Fish Scales: Morphology, Evolution, and Function

Fish scales: morphology, evolution, and function

A dissertation presented by

Dylan K. Wainwright

to

The Department of Organismic and Evolutionary Biology

in partial fulfillment of the requirements
for the degree of

Doctor of Philosophy

in the subject of

Biology

Harvard University
Cambridge, Massachusetts
April 2019

Dissertation Advisor: Dr. George V. Lauder Dylan K. Wainwright

Fish scales: morphology, evolution, and function

ABSTRACT

Fish scales are plates of dermal bone that are embedded in the dermis and epidermis of most fish species. Scales occur in many forms and past research has provided a framework to categorize scale types and a foundation for describing scale morphology. This thesis seeks to further our knowledge of scale morphology, evolution, and function using a combination of established, modern, and novel methods to quantify scale morphology in both intra- and inter-species contexts. In my first chapter, I describe how a method called gel-based stereo-profilometry can be used to image and quantify the three-dimensional topography of biological surfaces of interest, especially scales. In my second chapter, I use both gel-based profilometry and micro-computed tomography (μCT) to show that scale morphology of the bluegill (*Lepomis macrochirus*) is different qualitatively and quantitatively among regions of its body. In my third chapter, I use μCT and histology to study scale morphology in bigeye tuna (*Thunnus obesus*) and I show that regions on the anterior body of bigeye tuna have large scales made of cellular bone that are filled with adipocytes. In my fourth chapter, I quantify scale morphology across 59 damselfish (Pomacentridae) species that exhibit multiple transitions between pelagic and benthic feeding ecologies. With this comparative approach, I ask if scale morphology fits models of ecologically-driven evolution, thus seeking to link scale morphology to function. Finally, in my fifth chapter I briefly review our knowledge of elasmoid scale morphology and function, and I also demonstrate the quantitative effect mucus and epidermis have on scale morphology by *in vivo* imaging the surface topography of seven fish species.

Contents

Acknowledgments

First and foremost I would like to thank my advisor, George Lauder. His guidance, enthusiasm, and help were always appreciated and were crucial to this thesis. In a world that is filled with superlatives, George really is the best. I also acknowledge and thank Sam Ingersoll, Liz Karan, and Prof. Dave Collar for their generous assistance and collaboration in completing some of the work presented here. I wholeheartedly thank Karsten Hartel, Andy Williston, Meaghan Sorce, and Anne for their continuing support – without them, much of this thesis would have been impossible. I am deeply grateful to Dr. James Weaver for his enthusiasm and advice about my work and for helping to purchase an imaging system that was well-used and irreplaceable for the work herein. I further acknowledge the National Science Foundation's Graduate Research Fellowship program for allowing me to pursue the research and questions included in this thesis. Finally, I would not have been able to complete this work without the assistance of many people, and for that I thank Prof. Stephanie Pierce, Prof. Andy Biewener, Prof. Diego Bernal, Morgan Furze, Dr. Willy Goldsmith, Toby Arakawa (Tropic Fish Hawaii), Griffin Andres, Alex Shulman, Madeleine Ankhelyi, Meagan Popp, Dexter Summers, Chloe-Rose Colombero, the Office of Naval Research, Bob Brizzolara, Prof. Frank Fish, Prof. Lex Smits, Prof. Hilary Bart-Smith, Prof. Haibo Dong, Greenfins Tuna, Dr. Jeanette Lim, Dr. Valentina Di Santo, Dr. Callin Switzer, Maggie Starvish, Zane Wolf, Dave Matthews, Connor White, Prof. Dan Quinn, Peter Wainwright, Yoshi Wainwright, Naomi Wainwright, Carolyn Teragawa, Dr. Robin Thandiackaal, Dr. Dan Madigan, Dr. Terry Dial, Dr. Elsa Goerig, and Sarah Friedman.

For my grandfathers: Bill Teragawa and Steve Wainwright

Introduction

Surfaces are a crucial and fundamental feature of life – they allow for homeostasis and are the physical shell organisms use to interact with the world around them. Despite the important roles that surfaces play in biology, the various functions and complex three-dimensional (3D) nature of surfaces make them difficult to study and create challenges in linking surface form to function. However, modern imaging techniques hold promise for better understanding how diverse surface features impact organismal function and have allowed for the detailed study of biological surfaces, yielding bio-inspired advancements in adhesion (King *et al.*, 2014), drag reduction (Domel *et al.*, 2018), and hydrophobic surfaces (Feng *et al.*, 2002). In this thesis I focus my studies on the surfaces and scales of fishes to: 1) quantify fish surface morphology, 2) expand our knowledge of fish surface diversity, 3) seek evolutionary links between fish surfaces and fish ecology, and 4) gather evidence to link structure and function in fish surfaces.

Most fish surfaces are made of embedded bony scales and a superficial epidermis that secretes mucus (Sire and Akimenko, 2004). Scales come in a variety of different forms, which can broadly be grouped into smooth-edged (ganoid, cosmoid, cycloid) and spiny-edged scales (ctenoid, spinoid, crenate), with three categories (cycloid, ctenoid, spinoid) generating the bulk of scale diversity (Roberts, 1993; Wainwright and Lauder, 2016). Differences in scale type and morphology often exist among clades (Roberts, 1993), within clades (Ibañez and Jawad, 2018), and even within regions of a single individual (Dapar *et al.*, 2012; Wainwright, Ingersoll and Lauder, 2018). Although we have knowledge of qualitative scale diversity (Roberts, 1993; Meunier and Brito, 2004), we largely lack a quantitative understanding of scale diversity and 3D morphology, even though this information is crucial for making informed hypotheses about scale function. This thesis demonstrates the ability to

measure 3D morphology of scales and shows that scales are diverse in size, texture, and spacing (Wainwright and Lauder, 2016, 2018; Wainwright, Lauder and Weaver, 2017).

In chapter one, I demonstrate that an existing and new profilometry method called gel-based stereo profilometry is well-suited for imaging and quantifying the 3D topography of biological surfaces, especially fish scales (Wainwright, Lauder and Weaver, 2017). This method combines the speed of optical profilometry with the robustness of contact profilometry by using deformable gel pads with a painted bottom side that contact surfaces, thus creating an impression of the surface when the gel is held against it. The paint on the gel effectively removes any undesirable optical properties of the surface (clear, reflective) and six photographs with different lighting angles combine to reconstruct 3D topography of the surface. Gel-based profilometry is an exciting advancement in imaging and quantifying biological surfaces as it can rapidly reconstruct surfaces from about 22 mm by 16 mm to about 4.5 mm by 3 mm at resolutions that enable the easy identification of features that are tens to hundreds of microns in size. Gel-based profilometry is also non-destructive and I establish that it can be used *in vivo* to image surfaces of fish with delicate mucus and epidermis present (this work is extended in chapter five). Other common profilometry methods often struggle while imaging clear or wet material, only image very small areas (1 mm by 1mm), and thus also require destructive specimen preparation (comparisons between surface imaging methods are compared in chapter five). Gel-based profilometry also offers the ability to measure surface morphology in 3D and I show that fish surfaces are diverse in quantitative measurements of 3D morphology, such as surface roughness. Understanding the topographic nature of surfaces is crucial for explaining both surface diversity and potential functions, as surface topography likely plays an important role in many surface functions.

In chapter two, I use both gel-based profilometry and micro computed tomography (μCT) to study scale morphology of bluegill sunfish (*Lepomis macrochirus*) at different regions around the body (Wainwright and Lauder, 2016). I demonstrate qualitatively that scales on the gill cover of the bluegill

have spineless posterior edges and are therefore cycloid scales, while scales elsewhere on the body have small interlocking spines called ctenii at their posterior edges and are therefore ctenoid scales. Through the use of profilometry data, I show that measurements of surface topography and scale morphology are different among body regions. Similarly, μCT data demonstrate that measurements of whole-scale morphology differ among body regions. In this chapter I also provide data demonstrating the accuracy of gel-based profilometry when measuring a surface standard of known geometry. In addition, I provide a brief review of hypotheses linking scale form to function in the discussion of this chapter.

In chapter three, I use μCT and histology to investigate scale morphology of bigeye tuna (*Thunnus obesus*) at different body regions (Wainwright, Ingersoll and Lauder, 2018). In this study I discover that bigeye tuna scales are diverse in size and shape, and some scales are filled with adipocytes and have trabecular struts. These heavily modified trabecular scales are present in a portion of scales at the base of the tail and covering the cheek, but they mostly occur on a region called the corselet, which originates posterior to the gill opening and wraps around the body and the pectoral fin in bigeye tuna. I also confirm that bigeye tuna scales are made of cellular bone and I reveal that the modified scales also have arterioles and venules amongst the adipocytes. The fat-filled scales are much thicker than other scales and we hypothesize that these scales may help insulate bigeye tuna – a potentially useful feature because bigeye tuna maintain elevated body temperatures (regional endothermy).

In chapter four, I seek to understand how scales evolve in response to changes in ecology. For this study, I use damselfishes (Pomacentridae), which are a common group of coral reef fishes with close to 400 species that exhibit multiple transitions between benthic and zooplanktivorous feeding ecologies. I use previously published damselfish phylogenies and ecological categories (benthic, pelagic, and intermediate feeding groups) combined with gel-based profilometry, stochastic character mapping, and evolutionary model fitting to test the hypothesis that scale morphology follows specific

a priori models of ecologically driven evolution. Using a dataset of nearly 60 species of damselfishes, I find strong support that surface roughness on damselfishes shows coherent evolutionary patterns. In particular, pelagic-feeding damselfishes (planktivores) are evolving towards smoother surfaces, benthic-feeding species are evolving towards rougher surfaces, and intermediate-feeding species (feeding in both benthic and pelagic habitats) are intermediate. I make the argument that this pattern of surface roughness reflects our expectation that pelagic-feeding species are feeding in open water, usually in unidirectional currents and less turbulent flow, and that smooth surfaces could reduce body drag forces. Alternatively, benthic-feeding species spend time maneuvering around obstacles in more turbulent flow, and thus rougher surfaces could reduce drag under these fluid dynamic conditions. This study is the first modern comparative investigation of fish scale evolution and the results suggest that scale morphology is an important axis of functional diversity in fishes, indicating that future functional and comparative studies on fish scales may be important for understanding the diversity of scales and linking scale form to function.

In chapter five, I combine a brief review of fish scale morphology with a review of methods to study scales, and I add new data of *in vivo* surface topography of seven species of fishes (Wainwright and Lauder, 2018). I discuss our current knowledge of fish scale morphology as well as what is known and hypothesized about the function of fish scales. I also consider the advantages and disadvantages of different methods of studying scales including scanning electron microscopy, μCT, histology, and profilometry. Using paired topographic images from the same individual fishes *in vivo* and after standard museum preservation, I show that the presence of mucus and living epidermis tends to make fish surfaces smoother. In addition, mucus and epidermis can obscure many of the small features on fish scales (e.g. spines and ridges) that have been implicated in hypotheses of scale function; however, the degree to which features are obscured depends on the species. Therefore, the presence of mucus and epidermis likely plays an important role in modifying the surface of fishes, suggesting that more

study on fish surfaces with mucus present is needed to help unravel how mucus may change potential functions of fish scales (e.g. hydrodynamics, armor, anti-parasite).

In summary, this thesis applies modern methods to study the form and evolution of scale morphology in bony fishes and uses structural and comparative evidence to inform hypotheses of scale function. I believe this thesis represents a solid foundation upon which to complete future work to better unite knowledge of scale form with scale functions, as this remains a significant gap in our understanding of fish functional morphology.

References

Dapar, M. L. G., Torres, M. A. J., Fabricante, P. K. and Demayo, C. G. (2012) Scale Morphology of the Indian goatfish, *Parupeneus indicus* (Shaw 1803) (Perciformes: Mullidae), *Advances in Environmental Biology*, 6(4), pp. 1426–1432.

Domel, A. G., Domel, G., Weaver, J. C., Saadat, M., Bertoldi, K. and Lauder, G. V (2018) Hydrodynamic properties of biomimetic shark skin: effect of denticle size and swimming speed, *Bioinspiration & Biomimetics*. IOP Publishing, 13(5), p. 056014.

Feng, L., Li, S., Li, Y., Li, H., Zhang, L., Zhai, J., Song, Y., Liu, B. and Jiang, L. (2002) Super-Hydrophobic Surfaces : From Natural to Artificial, *Advanced Materials*, 14(24), pp. 1857–1860.

Ibañez, A. L. and Jawad, L. A. (2018) Morphometric variation of fish scales among some species of rattail fish from New Zealand waters, *Journal of the Marine Biological Association of the United Kingdom*, pp. 1–8.

King, D. R., Bartlett, M. D., Gilman, C. A., Irschick, D. J. and Crosby, A. J. (2014) Creating Gecko-Like Adhesives for 'Real World' Surfaces, *Advanced Materials*, 26, pp. 4345–4351.

Meunier, F. J. and Brito, P. M. (2004) Histology and morphology of the scales in some extinct and extant teleosts, *Cybium*, 28(1), pp. 225–235.

Roberts, C. D. (1993) Comparative morphology of spined scales and their phylogenetic significance in the Teleostei, *Bulletin of Marine Science*, 52(1), pp. 60–113.

Sire, J.Y. and Akimenko, M.-A. (2004) Scale development in fish: a review, with description of sonic hedgehog (shh) expression in the zebrafish (*Danio rerio*)., *The International Journal of Developmental Biology*, 48(2–3), pp. 233–247.

Wainwright, D. K., Ingersoll, S. and Lauder, G. V (2018) Scale diversity in bigeye tuna (*Thunnus obesus*): Fat-filled trabecular scales made of cellular bone, *Journal of Morphology*, pp. 1–13.

Wainwright, D. K. and Lauder, G. V. (2016) Three-dimensional analysis of scale morphology in bluegill sunfish, *Lepomis macrochirus*, *Zoology*. Elsevier GmbH., 119(3), pp. 182–195.

Wainwright, D. K. and Lauder, G. V. (2018) Mucus matters: the slippery and complex surfaces of fish, in Gorb, S. N. and Gorb, E. (eds.) *Functional Surfaces in Biology - From the Micro- to*

Nanoscale. 1st ed. Springer Berlin Heidelberg, pp. 223–246.

Wainwright, D. K., Lauder, G. V. and Weaver, J. C. (2017) Imaging biological surface topography *in situ* and *in vivo*, *Methods in Ecology and Evolution*, 8(11), pp. 1626–1638.

1

Imaging biological surface topography *in situ* and *in vivo*

Reprinted from:

Wainwright, D.K., Lauder, G.V. & Weaver, J.C. (2017) Imaging biological surface topography *in situ* and *in vivo*. *Methods in Ecology and Evolution*, 8, 1626-1638.

Article and supplement available at https://doi.org/10.1111/2041-210X.12778

Methods in Ecology and Evolution

Methods in Ecology and Evolution 2017, **8,** 1626–1638 doi: 10.1111/2041-210X.12778

Imaging biological surface topography *in situ* and *in vivo*

Dylan K. Wainwright*,[1], George V. Lauder[1] and James C. Weaver*,[2]

[1]*Museum of Comparative Zoology, and Department of Organismic and Evolutionary Biology, Harvard University, Cambridge, MA 02138, USA; and* [2]*Wyss Institute for Biologically Inspired Engineering, Harvard University, Cambridge, MA 02138, USA*

Summary

1. The creation of accurate three-dimensional reconstructions of biological surfaces is often challenging due to several inherent limitations of current imaging technologies. These include the inability to image living material, requirements for extensive specimen preparation and/or long image acquisition times, and the inability to image at length scales that are relevant for the study of interfacial phenomena that occur between the organism and its environment.

2. In this paper, we demonstrate the use of a new imaging approach that combines the benefits of optical and contact profilometry to image organismal surfaces quickly and without the need for any kind of specimen preparation, thus permitting three-dimensional visualization *in situ*.

3. As a proof of concept, we demonstrate the utility of this approach by imaging the surfaces of a wide range of live and preserved fish and other species, imaging wet, mucus-covered surfaces, and presenting quantitative metrics of surface roughness in a variety of natural and engineered materials.

4. Given the numerous wet, sticky, and slimy surfaces that abound in nature and the importance of the interface between species and their environments for the study of numerous biophysical phenomena, we believe this approach holds considerable promise for providing new insights into surface structural complexity in biological systems.

Key-words: 3D imaging, biology, mucus, profilometry, skin

Introduction

An organism's skin creates a boundary to the external world, and a detailed analysis of this three-dimensional surface structure is important for understanding numerous biophysical phenomena such as gas or moisture transfer, and the generation of drag forces that result from the movement of air and water across these surfaces (Lauder *et al.* 2016). Imaging and quantifying biological surface structural complexity can be accomplished by various methods, including contact and optical profilometry (Salvi *et al.* 2010), atomic force microscopy (AFM; Giessibl 2003), computed tomography (CT; Ritman 2004), confocal microscopy (Stephens 2003), and scanning electron microscopy (SEM; Kessel & Shih 1976). Despite the utility and prevalence of these methods, we currently lack a technique that is useful for the large area and high-throughput generation of three-dimensional surface datasets and is suitable for use with the wet, sticky, or mucus-covered surfaces of living organisms. To meet these needs, the applied method must be rapid, capable of imaging areas in the square millimetre to square centimetre size range, resolve surfaces with high x, y, and z resolution, not require sample preparation, be insensitive to surface optical properties, and be able to image living material. Although confocal microscopy, CT scanning, and AFM can be performed on living tissue, they either have poor surface resolution (CT scanning), sample only small regions (AFM), or are adversely affected by surface properties such as reflectivity (confocal microscopy). In this paper, we demonstrate the use of a gel-based photometric stereo profilometry technique (GelSight (Johnson & Adelson 2009; Johnson *et al.* 2011; Li & Adelson 2013; Li *et al.* 2014; Vetterli, Schmid & Wegener 2014; Lilien 2015; Yuan *et al.* 2015; Vorburger, Song & Petraco 2016)) that fills the aforementioned gap in surface-imaging technologies, and we apply it to a variety of biological surfaces from both living and preserved material.

Gel-based photometric stereo profilometry works by pressing a deformable clear gel pad with one opaque surface (Fig. 1a) onto an object, acquiring a series of photographs (Fig. 1c) from different illumination angles, and combining these images to create a three-dimensional topographical map (Figs 1b and 2). Acquiring the surface images occurs in less than 30 s, and performing a topographical reconstruction of the surface can be accomplished in c. 60 s offline. Additionally, no sample preparation is required and the approach can be routinely performed on live specimens. Wet, slimy, optically clear, or reflective surfaces can be successfully imaged with this approach because the opaquely-coated surface of the clear gel conforms to the specimen, resulting in a uniformly reflective profile that simplifies surface reconstruction.

Gel-based profilometry has been previously used to image surfaces for a variety of engineering applications, including

*Correspondence authors. E-mail: dylanwainwright@fas.harvard.edu, james.weaver@wyss.harvard.edu

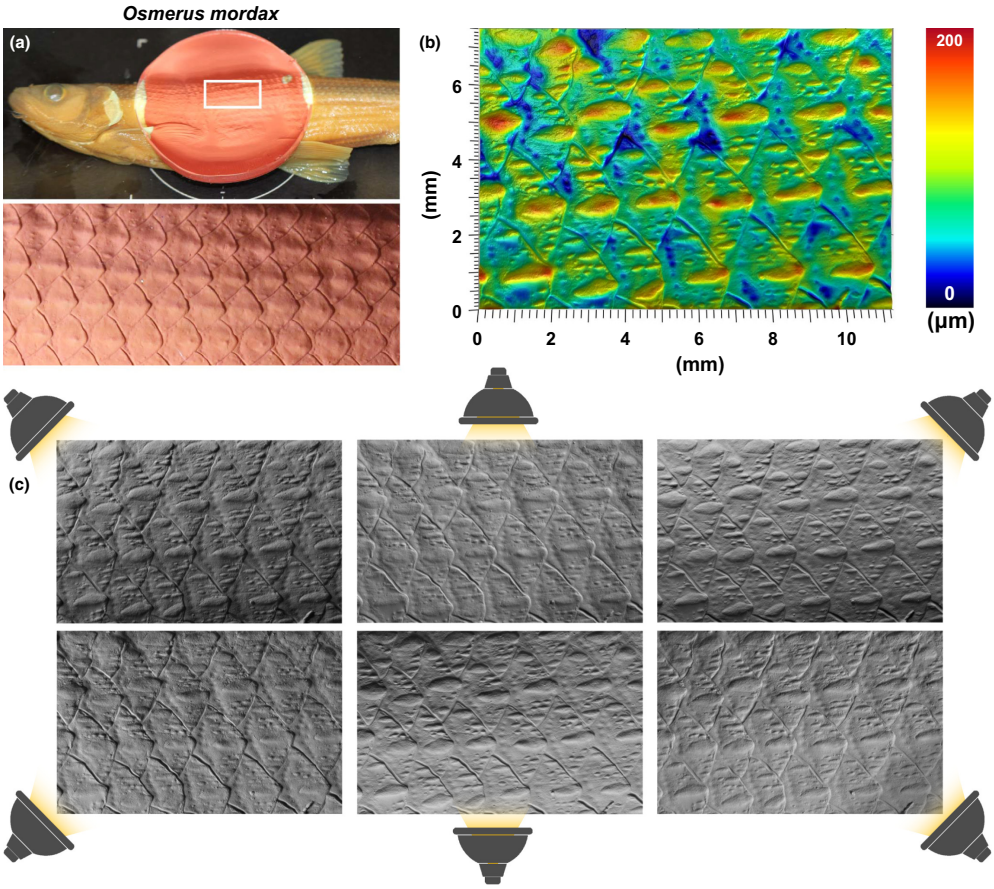

Fig. 1. Gel-based profilometry technique using the GelSight™ method. (a) A smelt (*Osmerus mordax*) is imaged by pressing a clear gel sensor with one coated opaque surface onto an area of interest and then illuminating the impression from six directions. (b) The surface is captured and reconstructed as a height map with known dimensions. Note the bumps which are keratinous breeding tubercles. (c) Each reconstructed surface is generated from six separate images taken with different illumination angles.

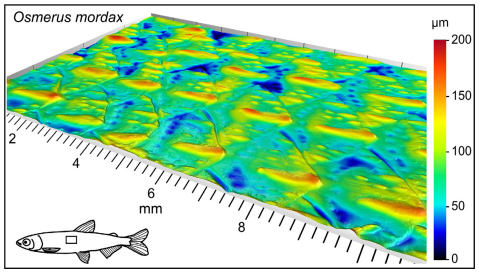

Fig. 2. Oblique view of rainbow smelt (*Osmerus mordax*) surface to highlight the 3D topography of the captured surface data. Scale bar indicates height above the lowest point on this surface.

surface characterization, firearm identification from bullet casings, and robotic sensing of surface texture (Johnson & Adelson 2009; Johnson *et al*. 2011; Li & Adelson 2013; Li *et al*. 2014; Vetterli, Schmid & Wegener 2014; Lilien 2015; Yuan *et al*. 2015), allowing researchers to quantify surface metrology metrics such as roughness, skew, and kurtosis in a high-throughput and noninvasive manner. For biological applications, this method is ideal for answering functional questions regarding surface-environment interactions in aquatic, aerial and arboreal species. Examples include the attachment organs of crustaceans and annelids; aerodynamic and hydrodynamic drag reduction in birds, insects, and fish; and how the scales of agamid lizards and arboreal snakes facilitate climbing. Applying this approach in a biological context, we present 3D surface reconstructions (Fig. 3) with quantitative metrology data (Table 1) from multiple organisms, and demonstrate how this technique can be used on mucus-covered surfaces (Fig. 4). Finally, using fish as a representative sample group, we showcase this technique's ability to capture the *in situ* topography of structurally complex biological surfaces (Figs 1, 2, 4, 5–9).

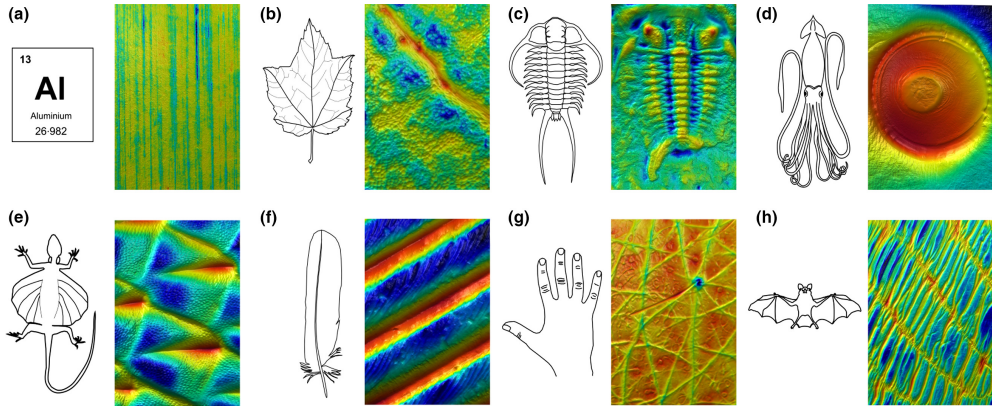

Fig. 3. 3D surface reconstructions using gel-based profilometry. Dimensions given below are image length and width, followed by the distance covered in the *z*-dimension (the elevation of the highest point on the surface). Warm colours correspond to higher, while cool colours correspond to lower elevations (highest: red, lowest: dark blue). (a) extruded aluminum sheet: 1·55 mm × 2·32 mm, *z*: 5 μm. (b) Red maple (*Acer rubrum*) leaf showing vein and cells: 0·73 mm × 1·1 mm, *z*: 31 μm. (c) Trilobite fossil: 14·8 mm × 22·2 mm, *z*: 915 μm. (d) Sucker with enclosed sucker ring from a giant squid (*Architeuthis dux*): 14·8 mm × 22·2 mm, *z*: 3·03 mm. (e) Flying lizard (*Draco timorensis*) belly scales: 0·90 mm × 1·31 mm, *z*: 117 μm. (f) Red-tailed hawk (*Buteo jamaicensis*) feather showing barbs and barbules: 0·75 mm × 1·09 mm, *z*: 152 μm. (g) Back of human hand showing a single hair and pore: 2·89 mm × 4·34 mm, *z*: 86·4 μm. (h) Greater mouse-eared bat (*Myotis myotis*) wing: 6·61 mm × 9·92 mm, *z*: 205 μm.

Table 1. Table of surface metrology parameters for different animals and materials. The table is organized in order of increasing roughness

Surface	Roughness Sq (μm)	Skew Ssk	Kurtosis Sku	Max height Sz (μm)
Aluminium	0·06	−0·20	3·5	6·7
Trout with mucus (*Salmo trutta*)	2·6	0·15	3·3	24·9
Trout preserved (*S. trutta*)	4·4	0·37	2·7	39·1
Hammerhead shark (*Sphyrna zygaena*)	5·2	−0·14	3·1	47·1
1000 grit sandpaper	6·3	0·22	3·1	66·3
Longnose butterflyfish (*Forcipiger flavissimus*)	7·6	0·11	4·1	74·3
Red maple leaf (*Acer rubrum*)	9·1	0·42	4·3	82·1
Back of hand (*Homo sapiens*)	14·3	−0·19	3·5	160·1
500 grit sandpaper	16·2	−0·33	4·5	215·8
Bonefish (*Albula vulpes*)	17·9	0·14	2·9	150·1
Bluegill preserved (*Lepomis macrochirus*)	19·9	−0·50	2·8	137·2
Bluegill with mucus (*L. macrochirus*)	21·7	0·20	2·8	138·7
Flying lizard (*Draco timorensis*)	24·7	0·56	3·2	173·1
Squirrelfish (*Sargocentron spiniferum*)	30·1	−0·11	3·0	235·1
150 grit sandpaper	36·0	0·10	2·8	280·8
80 grit sandpaper	53·6	0·14	2·9	389·7
Bichir (*Polypterus delhezi*)	55·8	−0·04	2·4	349·3
Triggerfish (*Xanthichthys ringens*)	59·8	0·42	3·5	449·2
Trunkfish (*Lactophrys triqueter*)	80·6	0·84	4·1	639·0
Armored catfish (*Hemiancistrus* sp.)	179·3	0·13	2·8	1125·2

Note the synthetic surfaces – aluminium and four grits of sandpaper – interspersed throughout the table as familiar standards.

Materials and methods

GEL-BASED PHOTOMETRIC STEREO PROFILOMETRY TECHNIQUE

Gel-based photometric stereo profilometry works by pressing a deformable clear gel elastomer pad (with one opaque, coated, surface) onto an object, acquiring a series of plan view photographs from different illumination angles, and combining these images to create a topographical map of the surface. For the examples described in this study, we used a system manufactured by GelSight Inc. (Waltham, MA, USA).

Using this approach, it is possible to create 3D reconstructions of a variety of topographically variable surfaces, from extruded aluminium with surface features of less than 5 μm in elevation, to a squid sucker disc with an elevation of 3 mm (Fig. 3a,d). This versatility is due to, but also limited by, the flexibility of the gel sensor that conforms to the surface and the ability of the camera and lens used to image it optically.

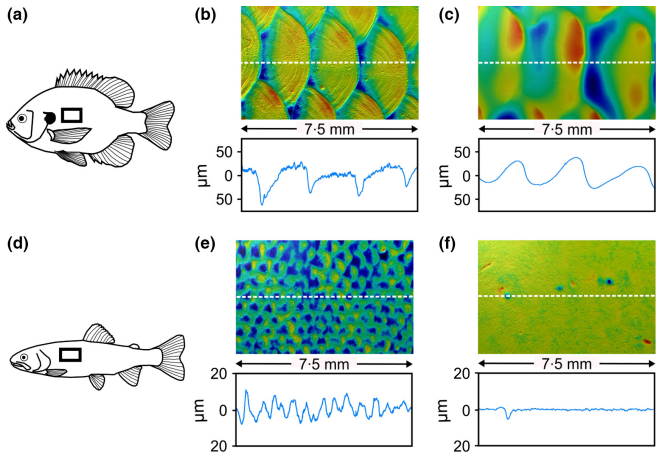

Fig. 4. 3D reconstructions of fish surfaces, with and without mucus. Images in b, c, e, and f are all 7·5 mm × 5 mm. Given below is the distance covered in the *z*-dimension (the elevation of the highest point on the surface). (a) The boxed region illustrates the location that was sampled on a bluegill sunfish (*Lepomis macrochirus*). (b) Image and elevation profile from the surface of a preserved (mucus-free) bluegill, *z*: 137 µm. (c) Image and elevation line-scan profile of an anesthetized (live) bluegill. The presence of mucus covers the microstructural features on the bluegill scales, but does not obscure the overall scale shape, *z*: 89 µm. (d) The boxed region illustrates the location that was sampled on a brown trout, (*Salmo trutta*). (e) Image and elevation line-scan profile from the surface of a preserved (mucus-free) trout, showing small scales, *z*: 39 µm. (f) Image and elevation line-scan profile of an anesthetized (live) trout. The mucus completely obscures the scales and only the lateral line pores are visible, *z*: 11·4 µm.

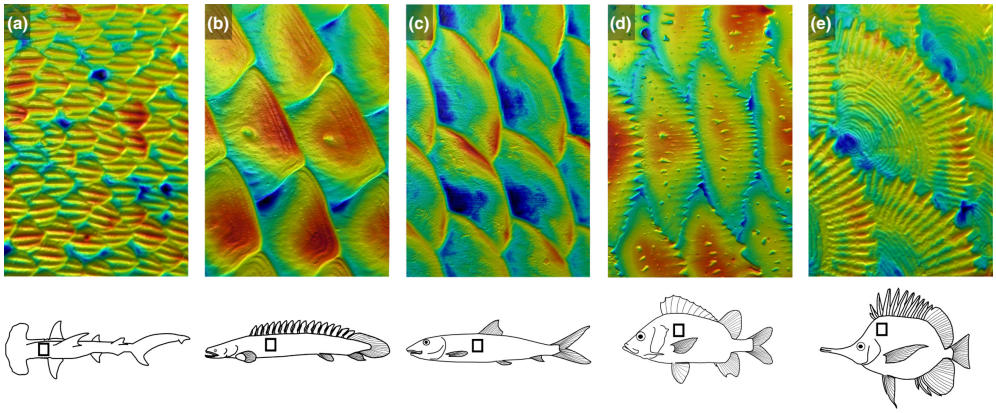

Fig. 5. Common fish scale types. Dimensions given below are image length and width, followed by the distance covered in the *z*-dimension (the elevation of the highest point on the surface). Warm colours correspond to higher, while cool colours correspond to lower elevations. (a) Placoid scales of a smooth hammerhead (*Sphyrna zygaena*): 0·749 mm × 1·09 mm, *z*: 24·5 µm. (b) Ganoid scales of a barred bichir (*Polypterus delhezi*): 7·47 mm × 10·9 mm, *z*: 331 µm. (c) Cycloid scales of a bonefish (*Albula vulpes*): 7·4 mm × 11·1 mm, *z*: 108 µm. (d) Spinoid scales of the sabre squirrelfish (*Sargocentron spiniferum*): 8·2 mm × 11·9 mm, *z*: 181 µm. (e) Ctenoid scales of the yellow longnose butterflyfish (*Forcipiger flavissimus*): 1·26 mm × 1·84 mm, *z*: 36·1 µm.

The standard GelSight system permits the successful imaging of surfaces ranging in dimensions from c. 15 mm × 22 mm to 3 mm × 4·2 mm using different optical zoom settings of the camera lens. Because an 18 megapixel camera is used, each surface is reconstructed with a point density of 18 million 3D (*x*,*y*,*z*) points, permitting the straightforward reconstruction of features down to 5 µm in size.

Gel sensors with different stiffness can be used depending on the specific application. For all of the surfaces imaged here, we used 'soft gels' (R40-XP565:30 SENSOR, Shore 00 30) with a thin opaque layer on one side. While 'soft gel' sensors are good at conforming to both complex and soft surfaces because they deform more easily, these properties also make them more prone to damage, which includes puncturing of the gel's opaque coating. Once a gel sensor becomes damaged, it creates small errors in the scan reconstruction. Although such errors can be corrected through post-processing, for the results reported here, a new gel

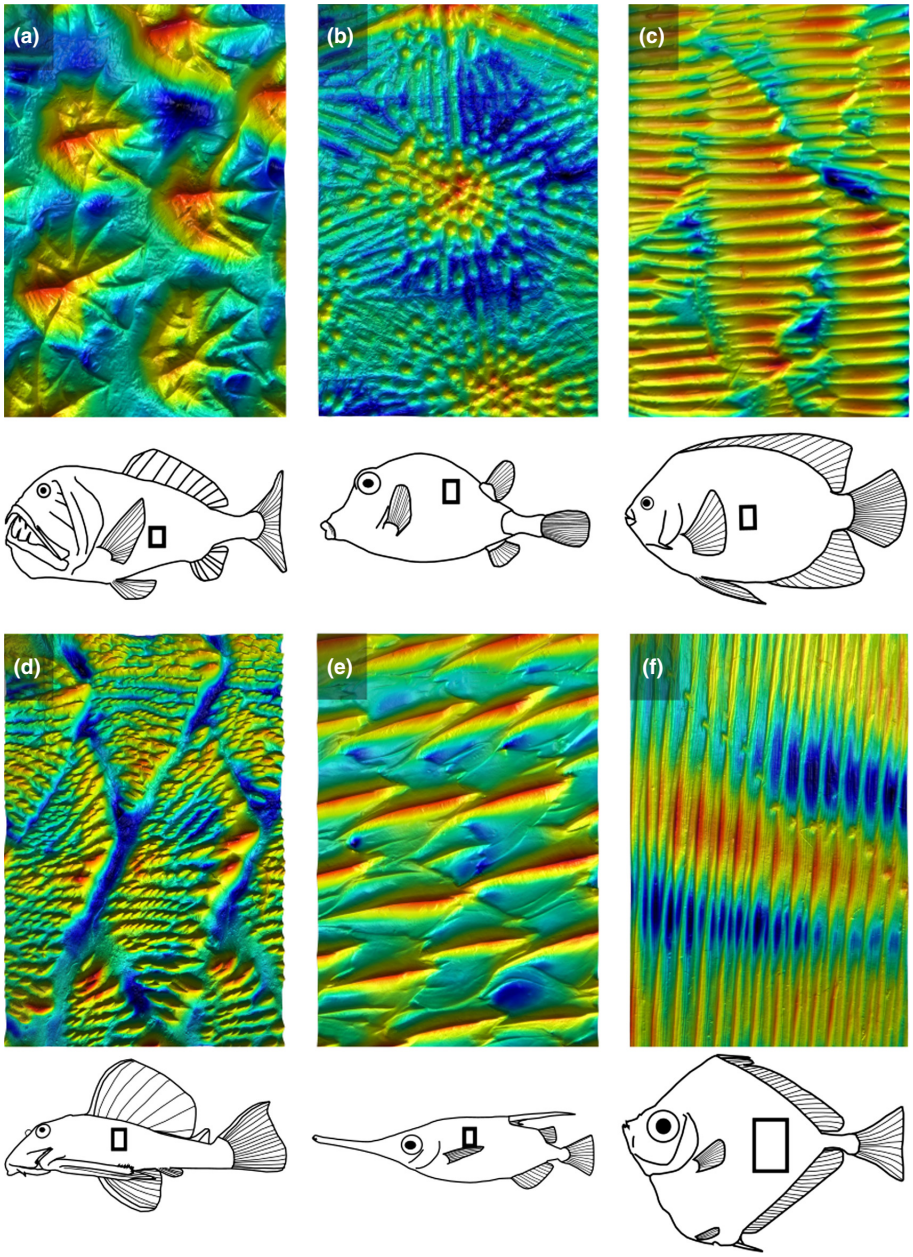

Fig. 6. Fish scale structural diversity. Dimensions given below are image length and width, followed by the distance covered in the *z*-dimension (the elevation of the highest point on the surface). Warm colours correspond to higher, while cool colours correspond to lower elevations. (a) Fangtooth (*Anoplogaster cornuta*): 1·89 mm × 2·83 mm, *z*: 392 μm. (b) Smooth trunkfish (*Lactophrys triqueter*): 14·8 mm × 22·2 mm, *z*: 337 μm. (c) King angelfish (*Holacanthus passer*): 3·72 mm × 5·43 mm, *z*: 184 μm. (d) Suckermouth armored catfish (*Hemiancistrus* sp.): 6·81 mm × 10 mm, *z*: 1·13 mm. (e) Longspine snipefish (*Macroramphosus scolopax*): 1·9 mm × 2·77 mm, *z*: 142 μm. (f) Spotted tinselfish (*Xenolepidichthys dalgleishi*): 9·22 mm × 13·6 mm, *z*: 388 μm.

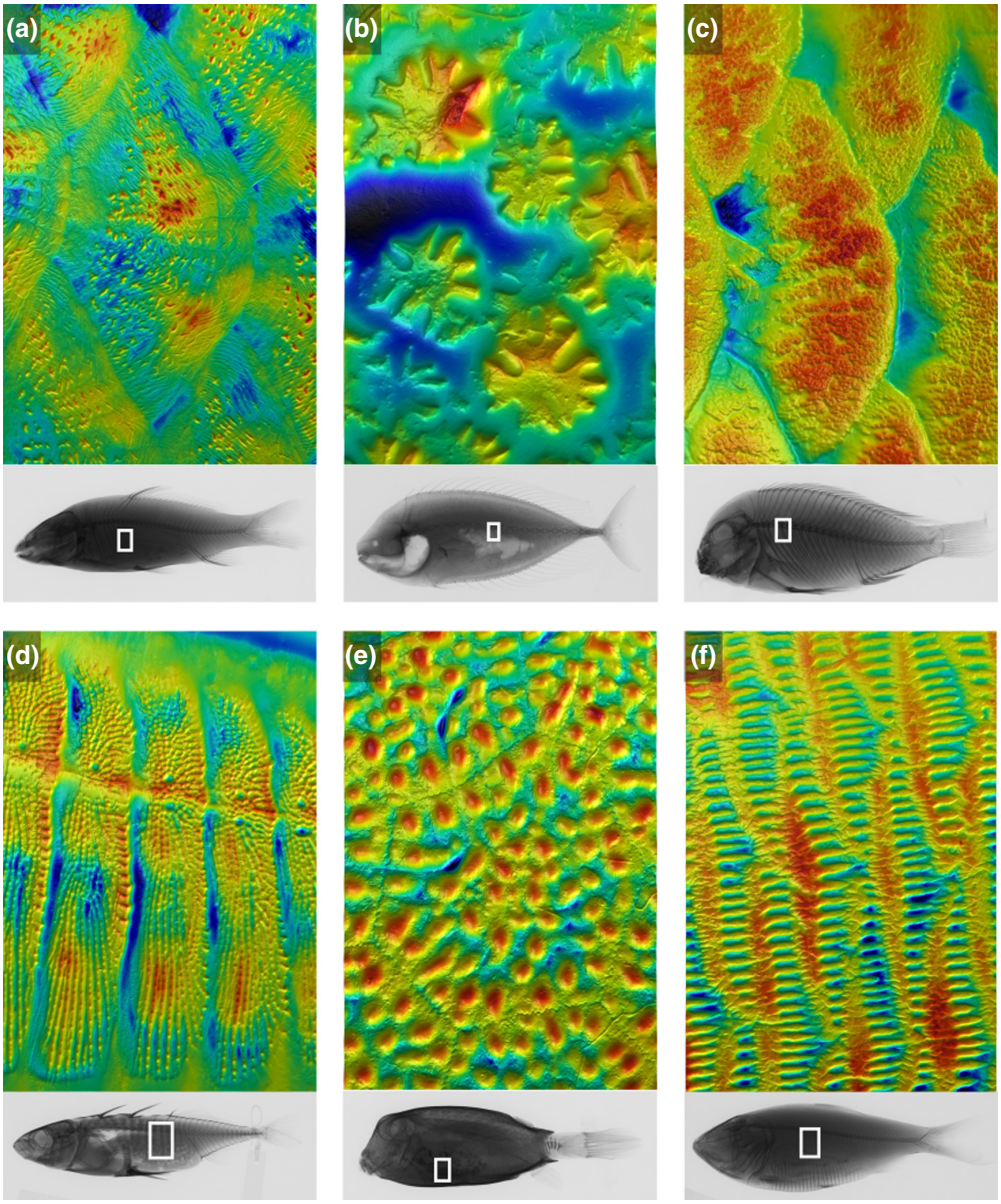

Fig. 7. Surface diversity of fish scales and scale-like tissues accompanied by whole specimen x-ray images with boxed regions of interest. Dimensions given below are image length and width, followed by the distance covered in the *z*-dimension (the elevation of the highest point on the surface). Warm colours correspond to higher, while cool colours correspond to lower elevations. (a) Carp (*Cyprinus carpio*): 8·96 mm × 11·5 mm, *z*: 121 μm. (b) Louvar (*Luvaris imperialis*): 1·9 mm × 2·77 mm, *z*: 130 μm. (**c**) *Tropheus moorei*: 4·94 mm × 7·2 mm, *z*: 258 μm. (d) Stickleback (*Gasterosteus aculeatus*): 8·94 mm × 11·5 mm, *z*: 180 μm. (e) Boxfish (*Ostracion meleagris*): 5·14 mm × 7·49 mm, *z*: 191 μm. (f) Menhaden (*Brevoortia patronus*): 7·4 mm × 10·8 mm, *z*: 133 μm.

was used after the first detected sign of surface damage. As a result, the number of uses per gel sensor is dependent on the surfaces being imaged as well as the gel type being used. For example, imaging flat surfaces with gentle curves can be performed hundreds of times without the need for gel sensor replacement.

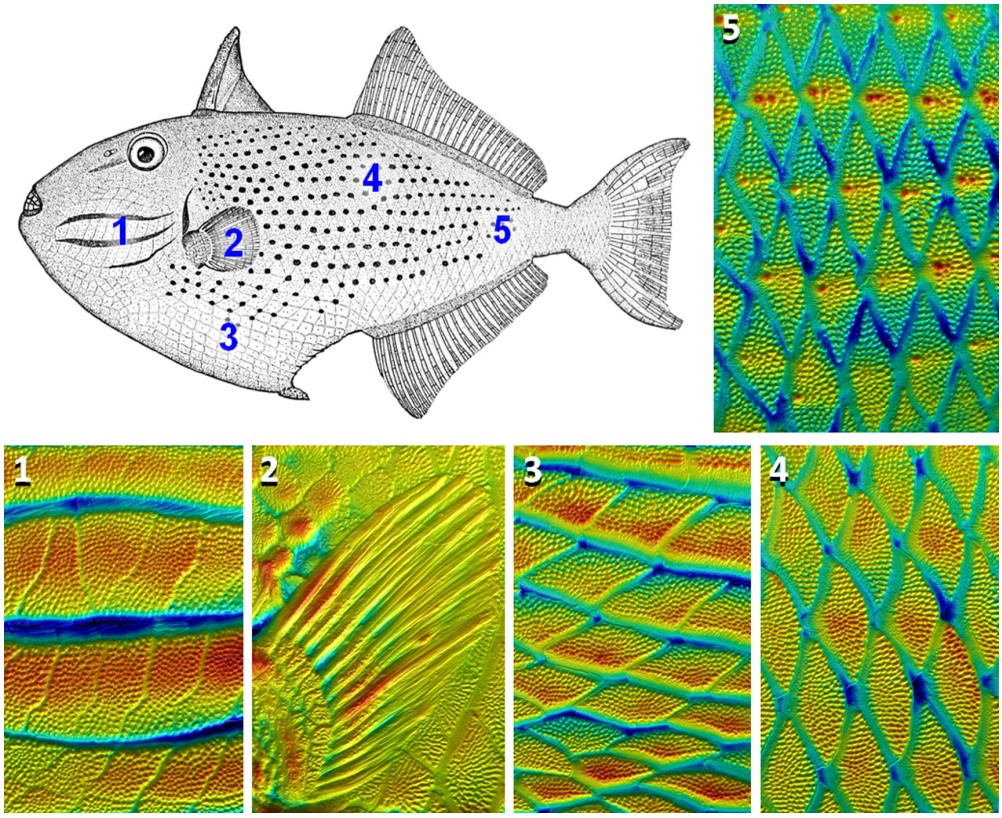

Fig. 8. Surface and scale diversity across the body of the sargassum triggerfish (*Xanthichthys ringens*). All images measure 14·8 mm × 22·2 mm and have the same orientation relative to the body. Warm colours correspond to higher, while cool colours correspond to lower elevations. Below we also give the distance covered in the *z*-dimension (the elevation of the highest point on the surface). 1: Ventral to the eye; *z*: 775 μm, 2: Pectoral fin, *z*: 925 μm, 3: Ventral to the pectoral fin, note the apparent 90° rotation of scales, *z*: 440 μm, 4: Ventral to the start of the second dorsal fin, *z*: 375 μm, 5: Between the end of the second dorsal and anal fin, *z*: 449 μm. Triggerfish image adapted from (Randall, Matsuura & Zama 1978).

A standard DSLR camera was used to acquire the source images from the different illumination angles, and for each combination of gel sensor type and camera setting, a unique calibration file is generated and used for surface reconstruction. For the samples described here, we used one gel type ('soft gel' R40-XP565:30 SENSOR, Shore 00 30) and standardized camera settings for each lens zoom level. The major trade-off we encountered was between the depth of field and shutter speed. Ideally, the depth of field should be as large as possible to image surfaces with large elevation changes, but this leads to longer exposure times, especially at higher zooms. To minimize movement of both the camera and the specimen during long image acquisitions, we used a shutter delay on the camera and limited foot traffic and other disturbances near our imaging system. After image acquisition, the 3D surface reconstructions were generated using the Gelsight Software (GSCapture Version 0.7).

IMAGING MUCUS

One unique application of gel-based profilometry is in the imaging of surfaces covered with viscous liquids such as mucus. Figure 4 shows examples of mucus imaging in two species of fish, the bluegill (*Lepomis macrochirus*) and the brown trout (*Salmo trutta*). These images were taken by anesthetizing an individual of each species using tricaine methanesulfonate (MS-222) under Harvard IACUC protocol 20-03 to GVL, and then immediately imaging the skin surface. For mucus imaging, we used 'soft gel' (R40-XP565:30 SENSOR, Shore 00 30) sensors and gently moved the gel into contact with the anesthetized fish. We found that even with moderate pressure between the gel sensor and the anesthetized fish, the integrity of the mucus layer was largely unaffected.

SPECIMENS IMAGED

Most of the preserved specimens imaged in this paper were selected from the Museum of Comparative Zoology (MCZ), Department of Ichthyology biodiversity collection. Each specimen was used with permission from the museum and their MCZ specimen numbers are given in Table S1, Supporting Information. No damage was done to the specimens imaged, as gel-based profilometry is a non-destructive technique for most applications. Because this technique applies light pressure to the surface of interest, we have found that wet specimens, such as fish preserved in ethanol, are often easier to image than dry animal

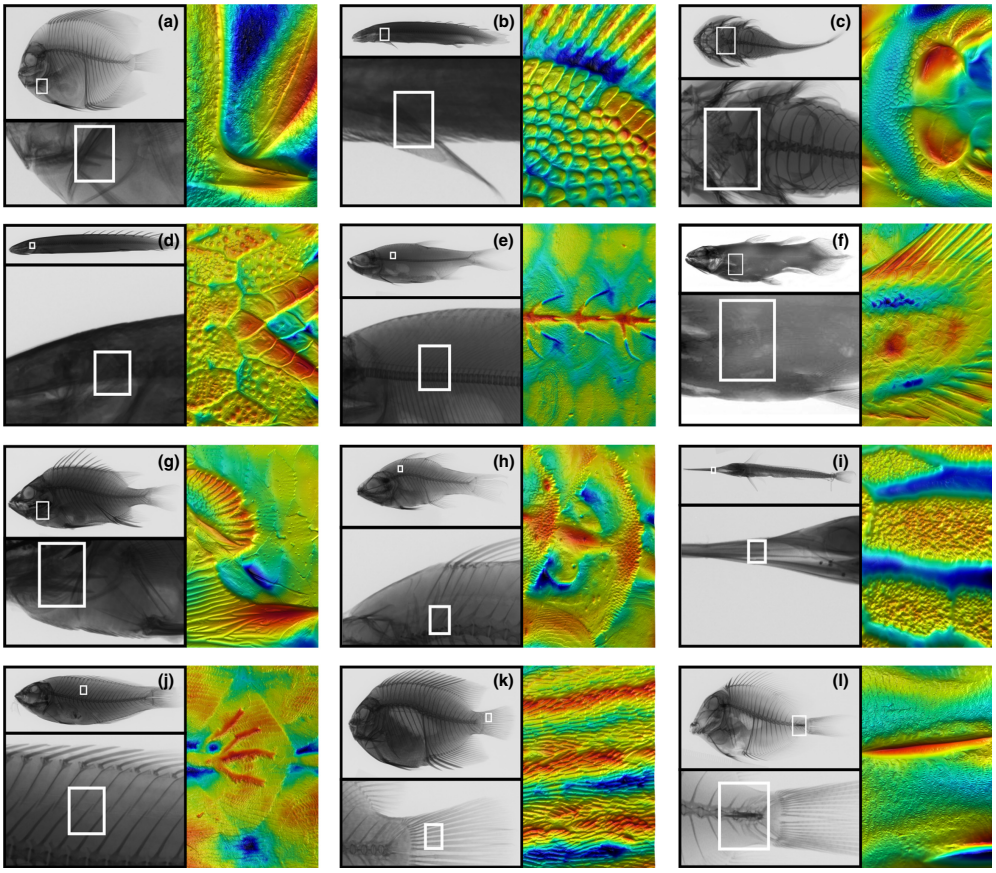

Fig. 9. Surface structural diversity in fishes accompanied by whole specimen x-ray images with boxed regions of interest. Dimensions given below are image length and width, followed by the distance covered in the *z*-dimension (the elevation of the highest point on the surface). Warm colours correspond to higher, while cool colours correspond to lower elevations (a) Gray angelfish (*Pomacanthus arcuatus*) preopercular spine: 7·45 mm × 10·9 mm, *z*: 1240 μm. (b) Barred bichir (*Polypterus delhezi*) pectoral fin: 5·14 mm × 7·12 mm, *z*: 285 μm. (c) Clingfish (*Gobiesox maeandricus*) adhesive disc derived from fused pelvic fins: 13 mm × 21·1 mm, *z*: 1340 μm. (d) Saddled bichir (*Polypterus endlicheri*) dorsal view of head: 14·8 mm × 22·2 mm, *z*: 976 μm. (e) Tarpon lateral line scales (*Megalops cyprinoides*): 7·5 mm × 9·96 mm, *z*: 152 μm. (f) Coelacanth (*Latimeria chalumnae*) pectoral fin: 13·8 mm × 20·4 mm, *z*: 496 μm. X-ray from Smithsonian National Museum of Natural History X-ray vision: Fish inside out series. (g) Sabre squirrelfish (*Sargocentron spiniferum*) preopercular spines: 13·7 mm × 18·2 mm, *z*: 1004 μm. (h) Cardinalfish lateral line (*Apogon imberbis*): 2·88 × 4·46 mm, *z*: 184 μm. (i) Striped marlin (*Kajikia audax*) teeth on the dentary: 5 mm × 7·5 mm, *z*: 532 μm. (j) Christmas wrasse (*Thalassoma trilobatum*) lateral line scales: 7·8 mm × 6 mm, *z*: 212 μm. (k) King angelfish (*Holacanthus passer*) tail scales: 3·72 mm × 5·4 mm, *z*: 214 μm. (l) Striated surgeonfish (*Ctenochaetus striatus*) scalpel on caudal peduncle: 5·6 mm × 7·8 mm, *z*: 931 μm.

material, which tends to be more brittle and less flexible, making it difficult to position specimens for imaging.

SURFACE ANALYSIS

Fish and other organisms often have curved surfaces, and when comparing surface textures among different regions or in species with different degrees of overall body curvature, it is necessary to remove this global curvature to reveal and compare local topographic features. We performed this background subtraction step in the Mountains Map software (Mountains Map 7.2.7344, Digital Surf, Besançon, France) using the 'remove form' function with varying polynomial complexities. Mountains Map software was also used to calculate the reported surface metrology parameters (Table 1), perform linear measurements in *x*, *y*, and *z* dimensions, and produce images of the surfaces.

Results

IMAGING SURFACE TOPOGRAPHY

Using gel-based profilometry, we have successfully imaged a diversity of surfaces, ranging from sandpaper and aluminium, to fossils, human skin, feathers, bat wings, and the mucus

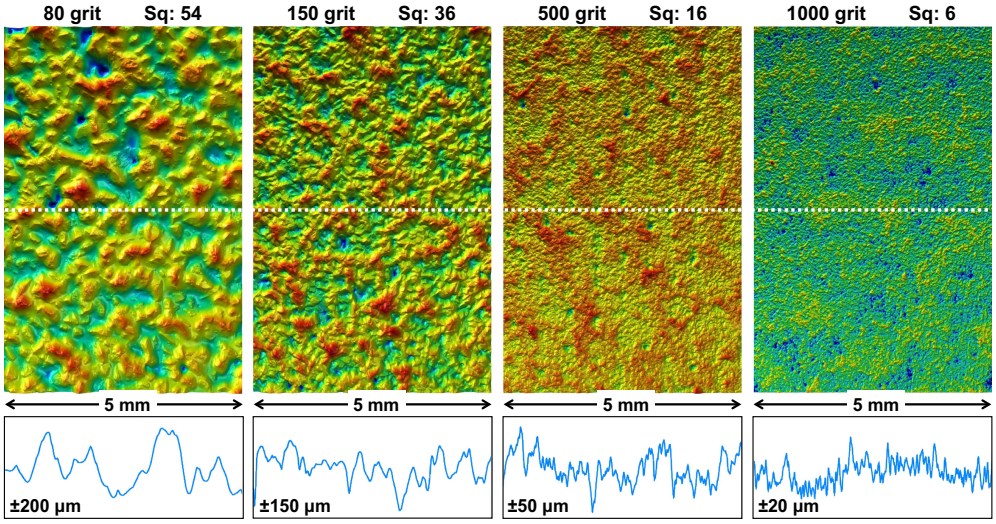

Fig. 10. Surface reconstructions of commercially available sandpapers (ranging from 80 grit to 1000 grit) to illustrate gel-based topographic imaging of known materials. All images are 5 mm × 7·5 mm with a corresponding elevation profile. Below we also give the distance covered in the *z*-dimension (the elevation of the highest point on the surface). Sq indicates root mean square surface roughness. (a) 80 grit sandpaper, *z*: 390 µm. (b) 150 grit sandpaper, *z*: 281 µm. (c) 500 grit sandpaper, *z*: 216 µm. (d) 1000 grit sandpaper, *z*: 66 µm.

coatings of living fish (Figs 3 and 4). All figures presented here illustrate elevation reconstructions performed using GelSight and MountainsMap software, where warmer colours correspond to higher elevations. Due to the wide range of surface roughness exhibited by the specimens used in this study, each image has a different elevation scale and the maximum elevation for each image is indicated in the figure captions.

Figure 3 illustrates a diversity of surfaces imaged with gel-based profilometry and demonstrates the versatility of this approach. While the aluminum sample is smooth to the touch, surface profilometry clearly reveals small (5 µm in elevation) parallel surface ridges resulting from extrusion manufacturing (Fig. 3a). Surface images of a red maple leaf show distinct individual cell boundaries, and leaf veins with elongated cells (Fig. 3b). An image of a hawk feather (Fig. 3f) reveals its characteristic barbs and barbules, with hooks (or hamuli) on the individual barbules. Figure 3g features human skin from one of the coauthors, clearly showing the voronoi-like organization of dead epidermal cells. For all of these examples, not only can small structural features be distinguished, but relative elevations can also be measured to address functional hypotheses (Table 1).

Panels c, d, e, and h in Fig. 3 illustrate applications of gel-based photometry for larger scan areas. The trilobite fossil (Fig. 3c) demonstrates non-destructive imaging of fossilized material. The giant squid sucker ring (Fig. 3d) clearly shows both the outer (infundibulum) and inner (acetabulum) (Kier & Smith 1990) sucker zones and the relatively low profile sucker ring teeth, and the flying lizard skin in Fig. 3e shows large keels present on each scale. Flying lizards are notoriously good climbers and these keels are directed posteriorly, perhaps serving as hooks or friction-increasing elements to reduce slipping. It is also possible that the keels and general scale morphology serve a complementary aerodynamic function during aerial gliding. Finally, the bat wing membrane (Fig. 3h) shows the structure of muscles and the associated connective tissue. The muscles are the smoother fibres oriented from the lower left to the upper right of the image and the connective tissue are the more kinked lines running in the opposite orientation (Skulborstad, Swartz & Goulbourne 2015). This organization of muscles and elastic fibres allows the bat wing to be both flexible and controllable (Skulborstad, Swartz & Goulbourne 2015).

IMAGING MUCUS-COVERED SURFACES

To demonstrate the advantages of this approach for investigating biologically relevant surface topography in living systems, we compared the 3D surface profiles from both fresh and preserved specimens of bluegill (*L. macrochirus*) and brown trout (*S. trutta*). The mucus-free specimens were formalin-fixed and preserved in ethanol at the Museum of Comparative Zoology (Harvard University) (Fig. 4b,e) and were compared to live, anesthetized individuals maintained in our laboratory (Fig. 4c,f).

Initial observations from the studies on preserved specimens reveal the dramatic size difference in scales between the two species, with the visible length of the bluegill scales being c. 3·5× those of the brown trout. The size difference in scales between the two species likely has a profound effect on how the scales interact with the surrounding water in the living fish. As predicted from the small size of trout scales (measuring

c. 15 μm in elevation), 3D reconstructions of the mucus-covered anesthetized fish revealed that the scales are completely obscured by the mucus layer, with the lateral line pores being the only surface features still visible (Fig. 4d–f) in the living specimens.

In contrast, bluegill have much larger scales that protrude c. 50 μm above the skin surface, and even in mucus-covered fish, the individual scales can still be distinguished. While the gross morphological features of the bluegill scales (size, shape and relative elevation) are clearly visible and similar in both live and preserved specimens (as revealed in corresponding line profiles), the structural details of the scales are completely obscured by the surface mucus in the living fish, raising intriguing questions as to functional significance of the scales' spines, ridges, and striations.

QUANTIFYING BIOLOGICAL SURFACES

Using 3D reconstructions obtained from both biological and engineered materials, we compared their surface roughness metrics in Table 1, organized by increasing roughness. Roughness (root-mean-square roughness, Sq), is given by the square-root of the sum across the surface of the squared distance of each point from the mean height. Skew (Ssk) and kurtosis (Sku) are parameters concerning the shape of the distribution of heights across a surface. A normal distribution of heights results in a skew of zero and a kurtosis of three. High positive skew corresponds to surfaces with many tall peaks, while low, negative skew describes surfaces with many deep valleys. A kurtosis above three indicates extremely high peaks or valleys, while a kurtosis below three indicates relatively gradual (and non-extreme) surface curvatures.

For this metrology parameter comparative study, we also included a wide range of commercially available sandpapers (ranging from 80 grit to 1000 grit) as familiar internal standards (see Fig. 10 for sandpaper surface images). From these measurements, the dramatic difference in fish surface roughness among the various taxa examined is readily apparent, which spans nearly two orders of magnitude.

The brown trout (Fig. 4b) was the smoothest fish measured, and unsurprisingly, the live specimen (with mucus) exhibited only half the roughness of its preserved counterpart (without mucus). The lone elasmobranch, the hammerhead shark (Fig. 5a), exhibited a similarly low surface roughness due to its very small placoid scales (compared to those found in most other ray-finned fish species). Both the trout and the hammerhead shark surfaces were both close in roughness to 1000 grit sandpaper, along with the scales of the longnose butterflyfish (Fig. 5e) and the surface of the red maple leaf (Fig. 3b). The next grouping of surface measurements, which were close to that of 500 grit sandpaper, included skin on the back of a human hand (Fig. 3g), bonefish scales (Fig. 5c), and the bluegill, both with and without mucus (Fig. 4a). While, for the different specimens examined, bluegill sunfish with mucus exhibited a higher roughness value than the bluegill without mucus, the difference was small (<2 μm, or about 10% of the roughness values), and could likely be due to the slight size differences between the two imaged specimens. The scales of the flying lizard (Fig. 3e) exhibited the next highest roughness values, followed by squirrelfish scales (Fig. 5d) and 150 grit sandpaper, 80 grit sandpaper, the ganoid scales of the bichir fish (Fig. 5b), and those of the sargassum triggerfish (Fig. 8). Trunkfish scales exhibited c. 20 μm greater roughness than the triggerfish, while the protective plates of armored catfish were over twice as rough as the trunkfish. Many of the fish with the roughest scales are traditionally categorized of as heavily armored fishes, with scales likely performing more of a protective rather than a hydrodynamic function.

None of the mapped surfaces exhibited particularly extreme values for skew, with most of these surfaces having an approximately normal distribution of heights. There were two surfaces with somewhat negative (about −0·5) skew values, the bluegill scales without mucus and the 500 grit sandpaper, due to the repeated occurrence of valley features on these surfaces. The red maple, and the scales of the flying lizard, triggerfish, and trunkfish, all had somewhat positive skew values (c. 0·5), indicating the presence of pronounced protruding features such as peaks, keeled scales, and leaf veins. Most surfaces also exhibited kurtosis values close to three, indicating a lack of extreme peaks or valleys. The few surfaces with high kurtosis values were the longnose butterflyfish scales, the red maple leaf, 500 grit sandpaper, and the trunkfish scales (kurtosis >4). These higher kurtosis values indicate more extreme surface features, such as the elevated leaf vein on an otherwise smooth leaf surface. In the results table, we also included values for the highest relative elevation (maximum height, Sz) on each surface, which largely followed the trends in measured roughness.

FISH SURFACE DIVERSITY: A CASE STUDY

As an example of a class of biological surfaces that illustrate the utility of *in situ* and *in vivo* gel-based surface profilometry measurements, we present data on a diverse assemblage of fish surfaces, which reveal remarkable variation both between species and on the body of single individuals. Quantifying the interface between fish and their fluid environment is critical for specific analyses of boundary layer structure (Anderson, McGillis & Grosenbaugh 2001; Dean & Bhushan 2010), and the general hydrodynamics of locomotion (Lauder & Tytell 2005). In order to obtain useful information regarding the structural complexity of fish scales, the surfaces must be imaged in a manner which allows analysis of areas on the order of 1 cm^2, because individual scales overlap and form complex patterns that generate intricate topography (Lauder *et al.* 2016; Wainwright & Lauder 2016). Smaller analysis regions miss the larger topographic arrangements that result from among-scale patterning.

Figures 4, and 5–9 illustrate the remarkable diversity of fish scale morphologies. Fish scales have been studied for more than a century and have been categorized and used for species identification and to inform the evolutionary relationships among different species (Agassiz 1833; Roberts 1993). Fish scales are also useful for aging purposes (Beardsley 1967; Park

& Lee 1988), for distinguishing different populations (Margraf & Riley 1993; Ibañez, Cowx & O'Higgins 2007), and for the identification of species from gut contents, middens, or the fossil record (Shackleton 1987; Daniels 1996). Historically, fish scales have been grouped into separate categories based on their external and internal morphological features (Agassiz 1833) and here, we present images of the five most common scale types among extant cartilaginous and ray-finned fishes (Fig. 5) using gel-based profilometry.

The placoid scales of sharks and rays are illustrated in Fig. 5a. These scales are typically very small (c. 100–200 μm long) and sit atop pedestals that grow from anchors in the skin (Motta *et al*. 2012). In many sharks, placoid scales form densely overlapping patterns (Fig. 5a), which have been shown to reduce drag and increase thrust under turbulent boundary layer conditions (Dean & Bhushan 2010; Oeffner & Lauder 2012). From our measurements, individual placoid scales are clearly visible, as well as the individual raised riblets on each scale, which have been hypothesized to play an important role in drag reduction.

While elasmobranch scales are all categorized as placoid, the scales of bony fishes have been further categorized, and here we provide examples of ganoid, cycloid, spinoid, and ctenoid scales (Fig. 5). Figure 5b shows the ganoid scales of a bichir, which are rhomboidal in shape and are characterized by a layer of hard ganoine covering their outer surface (Sire & Huysseune 2003). These scales interlock with pegs and sockets on each scale to create a flexible, but tough tile-like coating that has recently provided inspiration for the development of biomimetic armor (Duro-Royo *et al*. 2015). The two central scales in Fig. 5b are lateral line scales, with small pores that open to the lateral line canal where sensory hair cells measure water flow. Lateral line scales of different morphologies are also clearly visible in other imaged species (Fig. 9e,h,j).

Most bony fish have elasmoid scales, which have lost the hard ganoine layer and are instead composed of only two layers – an outer bony layer and an inner layer of connective tissue (Sire & Akimenko 2004). Elasmoid scales have been further categorized into cycloid, crenate, ctenoid, and spinoid forms based on the morphology of their posterior margins (Roberts 1993). Cycloid scales have smooth edges, and we show scales of a bonefish as an example (Fig. 5c). Figure 5d shows spinoid scales from a squirrelfish, with spines that are continuous with the body of each scale (and not separate ossifications). Finally, Fig. 5e shows the ctenoid scales of a butterflyfish, defined by the interlocking spines at the posterior margin, which are independent ossifications from the main body of each scale.

Figure 6 illustrates some extreme scale types ranging from the enlarged hexagonal plate-like scales of a boxfish, to the small, almost placoid-like scales of the fangtooth and snipefish, and the dorsoventrally elongated scales of the deepwater tinselfish. Figure 7 shows even more diversity of scale types in fishes, including cycloid and spinoid scales, as well as some highly modified morphologies that defy classification (Fig. 7b). In addition to scales, we also present surfaces of other interesting fish features, such as modified fins for surface attachment, protective head armour, lateral line pores, and spines (Fig. 9).

SCALE DIVERSITY WITHIN AN INDIVIDUAL

To investigate the diversity of scale surface topography across a single individual, we imaged the surface of the sargassum triggerfish, *Xanthichthys ringens* (Fig. 8), a planktivorous species from the tropical and sub-tropical Western Atlantic. Examining five different areas of the body: the cheek, belly, pectoral fin, and the regions below the dorsal fin and near the caudal peduncle, our results demonstrate dramatic region-specific variability in scale size, morphology, orientation, spacing, surface roughness, and aspect ratio across a single specimen.

Discussion

The ability to rapidly image the surface topography of biological specimens, both living and preserved, illustrates the unique capabilities of gel-based profilometry to generate data relevant to key questions regarding the surface roughness of biological tissues. Although other techniques exist for investigating biological surfaces (SEM, CT, AFM, etc.), gel-based profilometry has unique benefits which include the lack of specimen preparation, fast image acquisition time, and the ability to capture 3D surface details in the mm^2 to cm^2 size range of wet, reflective, or transparent materials.

Measuring the topography of mucus-covered surfaces (Fig. 4) is a unique and valuable capability of this imaging approach. Mucus has been proposed to perform an important immune function in fish (Shephard 1994; Roberts & Powell 2005; Subramanian, Ross & MacKinnon 2008), and some evidence suggests that fish mucus may also serve to reduce drag in some species (Bernadsky, Sar & Rosenberg 1993; Shephard 1994). As such, the ability to successfully image mucus coatings in living fish is important for assessing both health and swimming performance. In our live fish imaging studies (Fig. 4), we show that there appear to be complex interactions between scale size and associated mucus coats that creates a spectrum of different surfaces among species. As demonstrated, trout have small scales (10–15 μm elevation) that become undetectable when imaged *in vivo* with their mucus coating intact (Fig. 4d–f). In contrast, bluegill have much larger scales (30–60 μm elevation) that are still evident through the mucus coat, although lower amplitude surface elements become obscured (Fig. 4a–c).

Gel-based profilometry also permits the quantification of biological 3D surface metrics (Table 1). The ability to accurately measure surfaces in a size range relevant to many interfacial interactions allows for statistical analysis and comparative studies to be performed in a relevant way. By utilizing traditional metrology metrics such as roughness, skew, and kurtosis, we can compare biological surfaces to each other and to engineered surfaces (Table 1).

While the examples provided here represent applications for which this imaging approach is ideally suited, this

technique does have its limitations. In particular, gel-based profilometry is not well suited for generating realistic 3D reconstructions of protruding filamentous or large spiny structures, small diameter holes, or overhangs. It flattens filaments, cannot focus on the entire depth of long spines or conform to narrow holes, and cannot reconstruct undercuts or overhangs. Despite these limitations, as shown from the examples provided here, gel-based profilometry can be applied to address many research questions in the biological and physical sciences. For example, a long-standing hypothesis about the functional significance of different scale types seen across fish species surmises that spiny scales profoundly alter the boundary layer around fish to decrease drag (Bone 1972; Aleyev 1977; Burdak 1986; Helfman *et al*. 2009; Wainwright & Lauder 2016). Although it has been shown that the placoid scales of some sharks (Fig. 5a) can reduce drag and increase thrust under certain conditions (Oeffner & Lauder 2012), the same has not been shown for the scales of bony fish. As demonstrated here, fish scales show a tremendous amount of diversity both between taxa (Figs 5–7, 9) and on an individual (Fig. 8), yet no study has shown a connection between this structural diversity and hydrodynamic effects. Gel-based profilometry can supply us with accurate reconstructions of fish and other biological surfaces, which in turn, can be used in computational fluid dynamic models or as the basis for creating physical models via 3D printing for direct experimental studies. Indeed, any biological surfaces that come into contact with a substrate or a surrounding fluid can profoundly affect swimming, flying, running, jumping, or climbing, and understanding the three-dimensional topography of these surfaces is a critical step in assessing interfacial phenomena in biomechanics.

Authors' contributions

D.K.W., G.V.L., and J.C.W. conceived the ideas; D.K.W. collected and analysed the data and led the writing of the manuscript. All authors contributed critically to the drafts, and gave final approval for publication.

Acknowledgements

The authors are grateful to Kimo Johnson (GelSight, Inc.) for his imaging advice. This research on fishes was approved under Harvard IACUC 20-03. Our work was supported by ONR MURI Grant No. N000141410533 monitored by Bob Brizzolara to G.V.L., NSF GRF DGE-1144152 to D.K.W., and an HFSP Young Investigators Grant (RGY0067-2013) to J.C.W.

Data accessibility

All data used in this paper is included in the manuscript itself. Each image includes a height scale that is listed in the caption and the quantitative data we discuss is present in Table 1.

References

Agassiz, L. (1833) *Recherches sur les poissons fossiles: Tome 2*. Petitpierre, Neuchatel, Switzerland.

Aleyev, Y.G. (1977) *Nekton*. Dr. W. Junk b.v. Publishers, The Hague, the Netherlands.

Anderson, E.J., McGillis, W.R. & Grosenbaugh, M.A. (2001) The boundary layer of swimming fish. *The Journal of Experimental Biology*, **204**, 81–102.

Beardsley, G.L. (1967) Age, growth, and reproduction of the Dolphin, *Coryphaena hippurus*, in the Straits of Florida. *Copeia*, **1967**, 441.

Bernadsky, G., Sar, N. & Rosenberg, E. (1993) Drag reduction of fish skin mucus: relationship to mode of swimming and size. *Journal of Fish Biology*, **42**, 797–800.

Bone, Q. (1972) Buoyancy and hydrodynamic functions of integument in the Castor Oil Fish, *Ruvettus pretiosus* (Pisces: Gempylidae). *Copeia*, **1972**, 78–87.

Burdak, V.D. (1986) Morphologie fonctionnelle du tegument ecailleux des poissons. *Cybium*, **10**, 1–128.

Daniels, R.A. (1996) Guide to the identification of scales of inland fishes of northeastern North America. *New York State Museum Bulletin*, **488**, 1–93.

Dean, B. & Bhushan, B. (2010) Shark-skin surfaces for fluid-drag reduction in turbulent flow: a review. *Philosophical Transactions. Series A, Mathematical, Physical, and Engineering Sciences*, **368**, 4775–4806.

Duro-Royo, J., Zolotovsky, K., Mogas-Soldevila, L., Varshney, S., Oxman, N., Boyce, M.C. & Ortiz, C. (2015) MetaMesh: a hierarchical computational model for design and fabrication of biomimetic armored surfaces. *CAD Computer Aided Design*, **60**, 14–27.

Giessibl, F.J. (2003) Advances in atomic force microscopy. *Reviews of Modern Physics*, **75**, 949–983.

Helfman, G.S., Collette, B.B., Facey, D.E. & Bowen, B.W. (2009) *The Diversity of Fishes*, 2nd edn. John Wiley and Sons Inc., Hoboken, NJ, USA.

Ibañez, A.L., Cowx, I.G. & O'Higgins, P. (2007) Geometric morphometric analysis of fish scales for identifying genera, species, and local populations within the Mugilidae. *Canadian Journal of Fisheries and Aquatic Sciences*, **64**, 1091–1100.

Johnson, M.K. & Adelson, E.H. (2009) Retrographic sensing for the measurement of surface texture and shape. *IEEE Conference on Computer Vision and Pattern Recognition*, **2009**, 1070–1077.

Johnson, M.K., Cole, F., Raj, A. & Adelson, E.H. (2011). Microgeometry capture using an elastomeric sensor. *ACM SIGGRAPH 2011 Papers on – SIGGRAPH '11*, 1–8.

Kessel, R.G. & Shih, C.Y. (1976) *Scanning Electron Microscopy in Biology: A Students' Atlas on Biological Organization*, 1st edn. Springer-Verlag, Berlin, Heidelberg, Germany; New York, NY, USA.

Kier, W.M. & Smith, A.M. (1990) The morphology and mechanics of octopus suckers. *Biological Bulletin*, **178**, 126–136.

Lauder, G.V. & Tytell, E.D. (2005) Hydrodynamics of undulatory propulsion. *Fish Physiology*, **23**, 425–468.

Lauder, G.V., Wainwright, D.K., Domel, A.G., Weaver, J., Wen, L. & Bertoldi, K. (2016) Structure, biomimetics, and fluid dynamics of fish skin surfaces. *Physical Review Fluids*, **1**, 060502-1–060502-18.

Li, R. & Adelson, E.H. (2013) Sensing and recognizing surface textures using a GelSight sensor. *IEEE Conference on Computer Vision and Pattern Recognition*, **2013**, 1241–1247.

Li, R., Platt, R.J., Wenzhen, Y., Pas, A., Roscup, N., Srinivasan, M.A. & Adelson, E. (2014) Localization and manipulation of small parts using GelSight tactile sensing. *International Conference on Intelligent Robots and Systems*, **2014**, 3988–3993.

Lilien, R. (2015) *Applied Research and Development of a Three-Dimensional Topography System for Firearm Identification Using GelSight*. Acton, MA, USA.

Margraf, F.J. & Riley, L.M. (1993) Evaluation of scale shape for identifying spawning stocks of coastal Atlantic striped bass (*Morone saxatilis*). *Fisheries Research*, **18**, 163–172.

Motta, P., Habegger, M.L., Lang, A., Hueter, R. & Davis, J. (2012) Scale morphology and flexibility in the shortfin mako *Isurus oxyrinchus* and the blacktip shark *Carcharhinus limbatus*. *Journal of Morphology*, **273**, 1096–1110.

Oeffner, J. & Lauder, G.V. (2012) The hydrodynamic function of shark skin and two biomimetic applications. *The Journal of Experimental Biology*, **215**, 785–795.

Park, E.-H. & Lee, S.-H. (1988) Scale growth and squamation chronology for the laboratory-reared hermaphroditic fish *Rivulus marmoratus* (Cyprinodontidae). *Japanese Journal of Ichthyology*, **34**, 476–482.

Randall, J.E., Matsuura, K. & Zama, a. (1978) A revision of the triggerfish genus Xanthichthys, with description of a new species. *Bulletin of Marine Science*, **28**, 688–706.

Ritman, E.L. (2004) Micro-computed tomography – current status and developments. *Annual Review of Biomedical Engineering*, **6**, 185–208.

Roberts, C.D. (1993) Comparative morphology of spined scales and their phylogenetic significance in the Teleostei. *Bulletin of Marine Science*, **52**, 60–113.

Roberts, S.D. & Powell, M.D. (2005) The viscosity and glycoprotein biochemistry of salmonid mucus varies with species, salinity and the presence of amoebic gill

disease. *Journal of Comparative Physiology B: Biochemical, Systemic, and Environmental Physiology*, **175**, 1–11.
Salvi, J., Fernandez, S., Pribanic, T. & Llado, X. (2010) A state of the art in structured light patterns for surface profilometry. *Pattern Recognition*, **43**, 2666–2680.
Shackleton, L.Y. (1987) A comparative study of fossil fish scales from three upwelling regions. *South African Journal of Marine Science*, **5**, 79–84.
Shephard, K.L. (1994) Functions for fish mucus. *Reviews in Fish Biology and Fisheries*, **4**, 401–429.
Sire, J.-Y. & Akimenko, M.-A. (2004) Scale development in fish: a review, with description of sonic hedgehog (shh) expression in the zebrafish (*Danio rerio*). *The International Journal of Developmental Biology*, **48**, 233–247.
Sire, J.-Y. & Huysseune, A. (2003) Formation of dermal skeletal and dental tissues in fish: a comparative and evolutionary approach. *Biological Reviews of the Cambridge Philosophical Society*, **78**, 219–249.
Skulborstad, A.J., Swartz, S.M. & Goulbourne, N.C. (2015) Biaxial mechanical characterization of bat wing skin. *Bioinspiration & Biomimetics*, **10**, 36004.
Stephens, D.J. (2003) Light microscopy techniques for live cell imaging. *Science (New York, NY)*, **300**, 82–86.
Subramanian, S., Ross, N.W. & MacKinnon, S.L. (2008) Comparison of antimicrobial activity in the epidermal mucus extracts of fish. *Comparative Biochemistry and Physiology – B Biochemistry and Molecular Biology*, **150**, 85–92.
Vetterli, M., Schmid, M. & Wegener, K. (2014) Comprehensive investigation of surface characterization methods for laser sintered parts. *Proceedings of the Fraunhofer Direct Digital Manufacturing Conference*, **2014**, 1–6.
Vorburger, T.V., Song, J. & Petraco, N. (2016) Topography measurements and applications in ballistics and tool mark. *Surface Topography: Metrology and Properties*, **4**, 1–52.
Wainwright, D.K. & Lauder, G.V. (2016) Three-dimensional analysis of scale morphology in bluegill sunfish, *Lepomis macrochirus*. *Zoology*, **119**, 182–195.
Yuan, W., Li, R., Srinivasan, M.A. & Adelson, E.H. (2015). Measurement of shear and slip with a GelSight tactile sensor. *2015 IEEE International Conference on Robotics and Automation (ICRA)*, **2015**, pp. 304–311.

Received 11 November 2016; accepted 22 March 2017
Handling Editor: Erica Leder

Supporting Information

Details of electronic Supporting Information are provided below.

Table S1. Museum specimen identification numbers.

Supplemental Information for:

Imaging biological surface topography *in situ* and *in vivo*

Dylan K. Wainwright [1], George V. Lauder[1], and James C.Weaver[2]

[1]Museum of Comparative Zoology, and Department of Organismic and Evolutionary Biology, Harvard University, Cambridge, MA 02138, USA; and [2]Wyss Institute for Biologically Inspired Engineering, Harvard University, Cambridge, MA 02138, USA

Identification numbers for preserved specimens used in this study

Taxa	Museum number
Trilobite	MCZ 187961
Draco timorensis	MCZ 3178
Buteo jamaicensis	MCZ 364138
Myotis myotis	MCZ 45562
Sphyrna zygaena	MCZ 170998
Polypterus delhezi	MCZ 155306
Albula vulpes	MCZ 25734
Sargocentron spiniferum	MCZ 164931
Forcipiger flavissimus	MCZ 82668
Anoplogaster cornuta	MCZ 158736
Lactophrys triqueter	MCZ 12014
Holacanthus passer	MCZ 92077
Hemiancistrus sp.	MCZ 87873
Macroramphosus scolopax	MCZ 58397
Xenolepidichthys dalgleishi	MCZ 157769
Xanthichthys ringens	MCZ 11873
Lepomis macrochirus	MCZ 101480
Salmo trutta	MCZ 99406
Osmerus mordax	MCZ 52512
Cyprinus carpio	MCZ 18877
Luvaris imperialis	MCZ 55003
Tropheus moorei	MCZ 110027
Gasterosteus aculeatus	MCZ 101558
Ostracion meleagris	MCZ 24424
Brevoortia patronus	MCZ 23325
Pomacanthus arcuatus	MCZ 16190
Gobiesox maeandricus	MCZ 12929
Polypterus endlicheri	MCZ 29364
Megalops cyprinoides	MCZ 4419
Latimeria chalumnae	AMNH 32949h
Apogon imberbis	MCZ 125548
Thalassoma trilobatum	MCZ 14155
Ctenochaetus striatus	MCZ 29405

2

Three-dimensional analysis of scale morphology in bluegill sunfish, *Lepomis macrochirus*

Reprinted from:

Wainwright, D.K., Lauder, G.V. & Weaver, J.C. (2016) Three-dimensional analysis of scale morphology in bluegill sunfish, *Lepomis macrochirus*. *Zoology*, 119(3), 182-195.

Article and supplement available at https://doi.org/10.1016/j.zool.2016.02.006

Zoology 119 (2016) 182–195

Contents lists available at ScienceDirect

Zoology

journal homepage: www.elsevier.com/locate/zool

Three-dimensional analysis of scale morphology in bluegill sunfish, *Lepomis macrochirus*

Dylan K. Wainwright*, George V. Lauder

Museum of Comparative Zoology, Harvard University, 26 Oxford Street, Cambridge, MA 02138, USA

ARTICLE INFO

Article history:
Received 9 September 2015
Received in revised form 18 January 2016
Accepted 29 February 2016
Available online 5 March 2016

Keywords:
Fish locomotion
Locomotor performance
Scale morphology
Scale surface structure

ABSTRACT

Fish scales are morphologically diverse among species, within species, and on individuals. Scales of bony fishes are often categorized into three main types: cycloid scales have smooth edges; spinoid scales have spines protruding from the body of the scale; ctenoid scales have interdigitating spines protruding from the posterior margin of the scale. For this study, we used two- and three-dimensional (2D and 3D) visualization techniques to investigate scale morphology of bluegill sunfish (*Lepomis macrochirus*) on different regions of the body. Micro-CT scanning was used to visualize individual scales taken from different regions, and a new technique called GelSight was used to rapidly measure the 3D surface structure and elevation profiles of in situ scale patches from different regions. We used these data to compare the surface morphology of scales from different regions, using morphological measurements and surface metrology metrics to develop a set of shape variables. We performed a discriminant function analysis to show that bluegill scales differ across the body – scales are cycloid on the opercle but ctenoid on the rest of the body, and the proportion of ctenii coverage increases ventrally on the fish. Scales on the opercle and just below the anterior spinous dorsal fin were smaller in height, length, and thickness than scales elsewhere on the body. Surface roughness did not appear to differ over the body of the fish, although scales at the start of the caudal peduncle had higher skew values than other scales, indicating they have a surface that contains more peaks than valleys. Scale shape also differs along the body, with scales near the base of the tail having a more elongated shape. This study adds to our knowledge of scale structure and diversity in fishes, and the 3D measurement of scale surface structure provides the basis for future testing of functional hypotheses relating scale morphology to locomotor performance.

1. Introduction

Most bony fishes are covered in ossified plates called scales, which exhibit a broad range of morphological diversity. The scales typical of extant bowfins and teleosts consist of an acellular bone layer that covers a plate of haphazardly arrayed collagen fibers (Grande and Bemis, 1998; Sire and Akimenko, 2004). These scales are then arranged in imbricating patterns where a given scale overlaps with many others but remains uncovered posteriorly. This uncovered area is known as the posterior field, and its morphology has been used to categorize and describe fish scales for centuries (Agassiz, 1833). Elasmoid scales of teleosts are also organized into different types depending on their posterior field morphology: cycloid, ctenoid, crenate and spinoid (Roberts, 1993). Cycloid scales have a smooth posterior edge without any spines. Ctenoid scales have a posterior edge that is at least partly made of small, interlocking, tooth-like structures called ctenii (singular, ctenus) that form as separate ossifications and create a spiny posterior edge. Crenate scales are less common and have extra growths at the posterior margin that extend in flattened, finger-like projections. Finally, spinoid scales have spines on the posterior field that are not made of interlocking ctenii. Instead, their spines are part of the main body of the scale.

Although features of these basic scale types have been useful in studies of fish taxonomy (Cockerell, 1911; Lagler, 1947; Batts, 1964; Daniels, 1996; Grande and Bemis, 1998), there is relatively little work quantifying the pattern of scale variation within individuals (however, see Suzuki, 1971; Jawad, 2005; Esmaeili et al., 2007; Dapar et al., 2012). Further, the three-dimensional (3D) structure of scales is not well understood but is critical to the construction of hypotheses regarding the mechanical and hydrodynamic function

* Corresponding author.
E-mail addresses: dylanwainwright@fas.harvard.edu, dylan.wainwright@gmail.com (D.K. Wainwright).

http://dx.doi.org/10.1016/j.zool.2016.02.006
0944-2006/

of fish surface ornamentation. Some previous work has investigated scale-like armor and scale material properties of fishes (Vernerey and Barthelat, 2010; Yang et al., 2012; Zhu et al., 2012; Chintapalli et al., 2014), but there are few investigations on the hydrodynamic effects of scales. These previous hydrodynamic analyses have been conducted using rigid, non-moving models which do not reflect the pattern of oscillatory body bending that occurs during fish swimming (Burdak, 1986; Sagong et al., 2008). To investigate potential hydrodynamic effects of scale morphology on undulatory locomotion, we need to first understand scale surface morphology in three dimensions. To date, few studies have even quantified the morphology of teleost scales, and none have done so using the topography of in situ imbricating fish scales. We know of only two studies that examine the surface topography of teleost scales – and only one of these studies shows data on the elevation of scale surface features, and then only for a few individual scales (Sudo et al., 2002; Sagong et al., 2008). Understanding the 3D topography of scale surfaces is ultimately important to understanding the 3D hydrodynamic interactions happening along the body of fish, therefore scale morphology must be understood before hydrodynamic hypotheses for scale function can be developed.

The goals of the present study are to qualitatively and quantitatively describe the scale morphology of a focal species, the bluegill sunfish (*Lepomis macrochirus*), while also exploring a new surface imaging technique that allows measurement of the elevation of scale surface features. In this study, we were able to determine how the 3D structure of bluegill scales varies over different regions of the body, while also quantifying the 3D morphology of both scaled surfaces and single whole scales. Our initial hypothesis was simple: we expected scales to differ across the body of bluegill in both shape and surface structure, in part due to adaptation to differing amplitude of motion exhibited along the body during undulatory propulsion (Jayne et al., 1996; Drucker and Lauder, 2000; Standen and Lauder, 2005). Specifically, we used a novel system called GelSight (GelSight Inc., Waltham, MA, USA) to image the surface topography of scale patches from six regions of the body. This technique allowed us to measure scale shape and surface elevation, and to calculate surface metrics to describe the fish surface on regions of scales in situ. We also used computed tomography (CT) scanning to image individual whole scales from the same six patches to obtain more traditional measurements of size and shape of isolated scales.

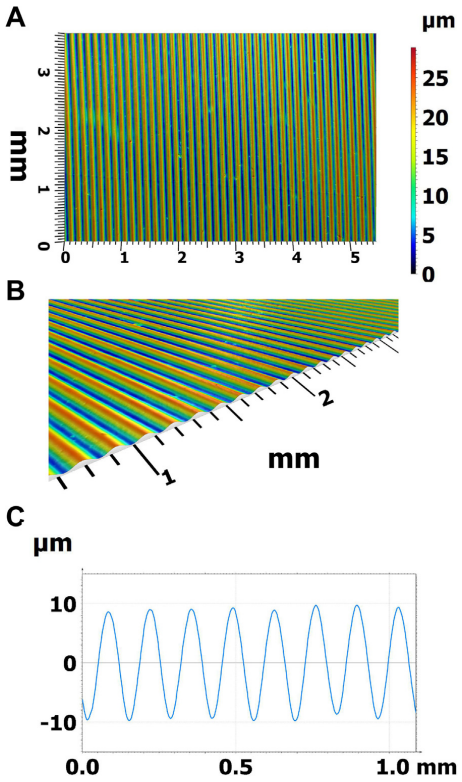

Fig. 1. GelSight was performed on a standard calibration surface with a sinusoidal pattern of known dimensions (see Section 2.2). (A) The sinusoid surface with peak-to-peak amplitude of 19 μm is displayed with a scale bar. (B) Also shown is an oblique view of the surface imaged with GelSight. (C) A profile of the surface is shown, where peak amplitude is within 2% of the expected 19 μm and the wavelength is not significantly different from the expected 135 μm.

2. Materials and methods

2.1. Study animals

Bluegill (*Lepomis macrochirus*) were used for the present study due to the considerable body of previous data on body shape, swimming mechanics, hydrodynamics, and energetics in this species (Kendall et al., 2007; Flammang and Lauder, 2008; Ellerby and Gerry, 2011; Flammang et al., 2011; Gerry et al., 2011). *L. macrochirus* is a freshwater fish found throughout North America in a wide range of habitats, but it does best in areas of slow flow. Specimens were taken from the Harvard Museum of Comparative Zoology's (MCZ) Ichthyology Collection. Three individuals of the same size class and in good condition were chosen for study from MCZ 101480 (Yawgoo Millpond, Slocum, RI, USA; April 8th, 1993; 10.84–11.83 cm standard length). Specimens were initially fixed in 3.7% formalin and then preserved in 70% ethanol after fixation. It is important that the fish be from the same population because intraspecific differences in scale morphology among populations have been documented in other species (Richards and Esteves, 1997). The three fish used had standard lengths of 11.31 cm, 10.84 cm, and 11.83 cm giving a mean standard length of 11.32 cm and a standard deviation of 0.49 cm.

2.2. GelSight imaging and analysis

GelSight is a new surface imaging technique that was used for the present study. It has been used in robotics to recognize surface textures and pressures (Li and Adelson, 2013; Li et al., 2014), but has never before been used for biological surface analysis. GelSight is a two-component system consisting of a camera and a piece of elastomer gel (Johnson and Adelson, 2009; Johnson et al., 2011). Proprietary gels (http://www.gelsight.com/) are made where one side is coated in reflective paint. The reflective side is pressed into the object of interest so the gel conforms to the surface of the object. An array of six LED lights allows illumination of the gel from different angles, and six photographs are taken using different angles of illumination (Fig. 1). Once the system is calibrated using a surface with known geometry, the GelSight software then processes these photographs into a 3D surface where each pixel is a 3D point. This system is non-damaging and can be performed on optically clear and wet material, allowing us to sample non-destructively without sample preparation, even on clear scales. This is in contrast to

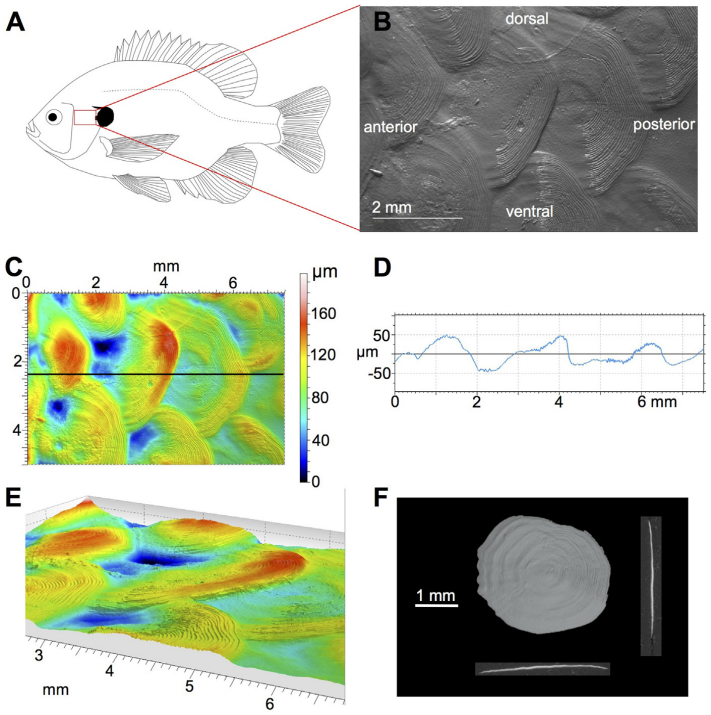

Fig. 2. Scales from the opercle region of *Lepomis macrochirus*. (A) Scales were imaged on the gill cover (opercle) of bluegill sunfish. (B) Grayscale image of the opercular scale surface – all panels show scales in this anatomical position. Note that scales are cycloid (without ctenii) and have small concentric circuli. (C) We show the surface in three-dimensions as a colored elevation map with a scale bar. (D) A profile line graph along the black reference line from C shows the topography of the surface – the plateaus and hills are the posterior fields, which are between 1.5–2.2 mm long with peak to valley heights of 50–100 μm. The small oscillations on the plateaus are caused by the circuli. (E) We also show an oblique view of the surface with elevation visually exaggerated by 10% to illustrate the 3D nature of these data. (F) Whole scales were imaged with μCT and an opercle scale is displayed with sagittal and transverse cross-sections. The scales of the opercle are oval in general shape and lack radii, although radii-like ridges are visible in the anterior region of the scales.

other surface imaging techniques that require sample preparation, especially on wet or clear material.

We used three bluegill specimens for GelSight, and on each specimen we investigated the same six body regions (with the name we have given each region in parentheses): (i) the operculum or gill-cover of the fish (opercle), (ii) between the spinous dorsal fin and the lateral line (dorsal), (iii) between the lateral line and the pectoral fin (central), (iv) between the pectoral fin and the underside of the body (ventral), (v) below the lateral line at the anterior caudal peduncle (peduncle), and (vi) below the lateral line on or near the hypural plate, but not on the caudal fin rays (tail). We always imaged the left side of the fish. Panel A in each of Figs. 2–7 shows the location of the sites sampled (opercle, dorsal, central, ventral, peduncle, and tail). We did not attempt to image the exact same scales on different fish, but limited our sampling to these small regions and used patches of scales that appeared undamaged. Scale surfaces were lightly brushed with a paintbrush to clean them of debris before imaging. We used a zoom lens to take images measuring 7.52 mm by 5.01 mm with a point density of 5202 by 3465, giving pixel resolution of 1.45 μm in the plane of the scan. One scan at each of the six regions was taken on each of the three fish.

To demonstrate the validity of this approach, we also used GelSight to image a sinusoidal surface standard with known dimensions (Fig. 1). This surface is made of symmetrical sinusoid riblets of amplitude 19 μm and wavelength 135 μm. This roughness standard is #525E (Rubert & Co. Ltd, Cheadle, UK), and represents a calibrated ISO industry-standard for surface metrology. GelSight imaging provided values that are very close to the specified dimensions; after measuring values at eight peaks, we found a mean peak-to-peak amplitude of 18.65 μm, reflecting a small but significant difference of 0.35 μm, or about 1.8% of 19 μm (t-test, $t = -2.579$, df = 7, $p = 0.0365$). We found no statistical difference in wavelength from the manufacturer's specified 135 μm (t-test, mean = 134.8 μm, $t = -0.378$, df = 7, $p = 0.72$). These values show that GelSight is a valid method for recovering surface geometry down to the micron scale.

GelSight scans were analyzed individually using TalyMap Platinum v5.1 (Digital Surf, Besançon, France), which is a surface analysis software package. Each surface was smoothed using TalyMap's "remove form" function. This corrects the surface to remove any large-scale curvature, while keeping the surface texture intact – an important correction to allow comparison of surface structure among samples. We then used TalyMap to generate values for 30 different surface metrology variables. We decreased and refined the number of metrology parameters during our statistical analysis, as explained in Section 3.2.

GelSight also creates 2D greyscale images of the regions that were scanned. We used these images to measure 2D morphological features of each scanned region in ImageJ v1.45s (Rasband, 1997–2015). We measured six variables on three posterior fields

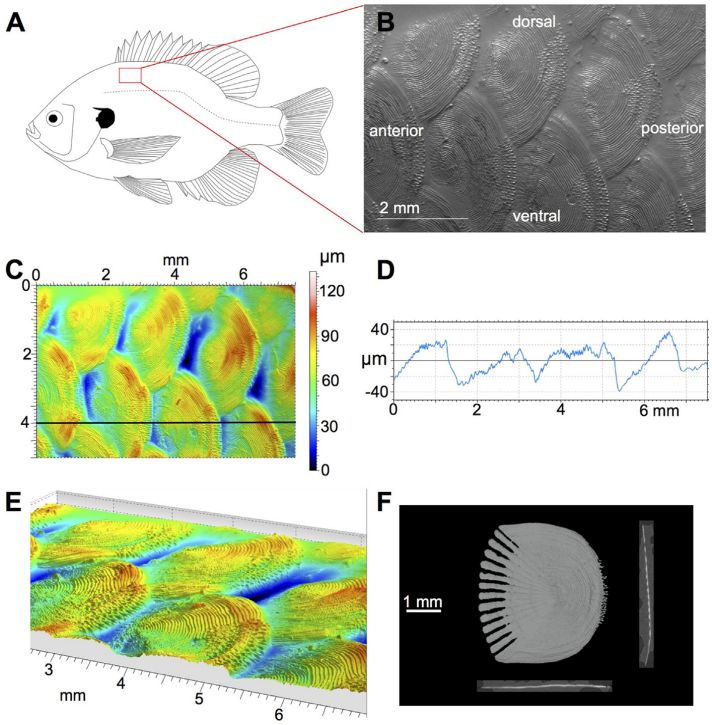

Fig. 3. Scales from the dorsal region of *Lepomis macrochirus*. (A) Scales were imaged on the dorsal region of fish, in the area between the first dorsal spines, and the lateral line. (B) Grayscale image of the opercular scale surface – all panels show scales in this anatomical position. (C) Scales in this region are ctenoid. We show the surface in three-dimensions as a colored height map with a scale bar. (D) The reference line in C is graphed as a profile line with zero as the average elevation of the surface. Hills correspond to posterior fields, which are around 2 mm long with peak to valley heights of 50–80 μm. (E) We also show an oblique view of the surface with elevation visually exaggerated by 10% to illustrate the 3D nature of these data. (F) We imaged individual scales with μCT, allowing us to display cross sections of scales as well as their three-dimensional representations. Radii are present and widely spaced along the anterior scale margin, which is covered by more anterior scales and not visible in images B-E.

for each scan: (i) posterior field height (dorsoventral axis), (ii) posterior field length (anteroposterior axis), (iii) posterior field area, (iv) area covered in ctenii, (v) length of the posterior margin, and (vi) length of the posterior margin made of ctenii. However, three full posterior fields were not always visible in each scan, so instead measurements were taken over half of the posterior field and multiplied by two. The three values for each variable were averaged for the scan, and that average was then used in statistical analyses. In addition, we used the six measured variables to calculate three metrics of posterior field shape and morphology: posterior field aspect ratio, percent of posterior field ctenii coverage, and percent of the posterior margin made of ctenii. We calculated posterior field aspect ratio by dividing the posterior field height by the posterior field length measurements, meaning lower values correspond to a posterior field more stretched in the anteroposterior axis. We calculated percent of posterior field ctenii coverage by dividing the area of the posterior field covered with ctenii by the total area of the posterior field. We calculated the percent of the posterior margin made of ctenii by similarly dividing the length of the posterior margin made of ctenii by the entire length of the posterior margin. These nine variables, three of which were calculated from the other six, were combined with the 30 surface metrology variables in an analysis to decrease and refine the number of variables as explained in Section 3.2.

2.3. μCT imaging and analysis

CT-scans have advantages over traditional microscopy techniques because they allow for a reconstruction of 3D morphology and they separate hard tissue, supplying data on the density of the region of interest. For the present study, we made use of CT scans instead of microscopy to accurately measure the thickness of scales and show that scales can be imaged accurately using μCT.

After GelSight scanning, we removed individual scales from only the specimen measuring 11.31 cm in standard length. Scales were taken from all six regions of interest described in Section 2.2 (opercle, dorsal, central, ventral, peduncle, and tail). We used a SkyScan 1173 micro-CT scanner (Bruker microCT, Kontich, Belgium) at a resolution of 6.75 μm voxel size to create our computed tomography (CT) data. For all scans, we used a voltage of 40 mV and a current of 200 μA. We removed four scales from each region sampled (opercle, dorsal, central, ventral, peduncle, and tail) and scanned each region's scales together, but only analyzed three scales from each region. The extra scale allowed us to discard scales that were damaged or bent in preparation but went unnoticed until the scan. These scans were reconstructed as image stacks using the program NRecon v1.6.9 (Bruker microCT). We used Mimics v16.0.0.235 (Materialise, Leuven, Belgium) to resolve our image stacks into 3D models.

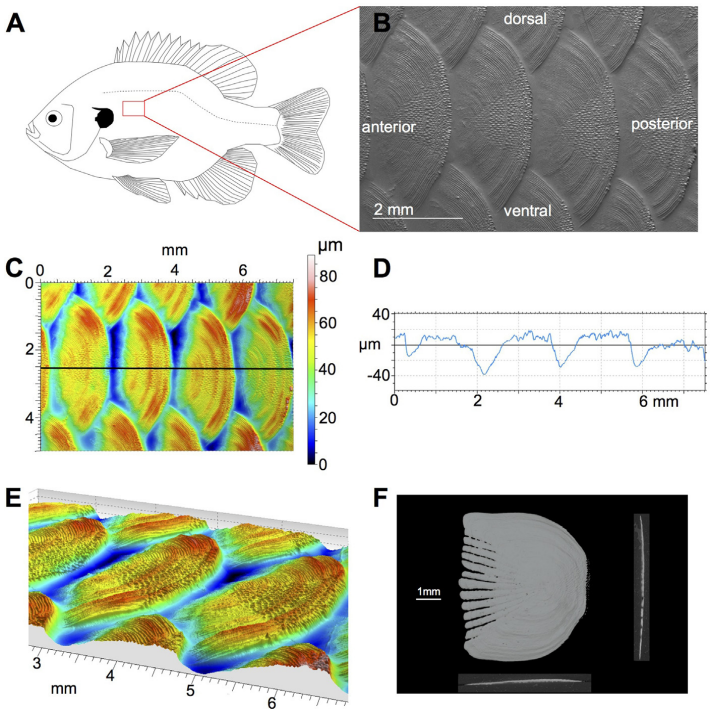

Fig. 4. Scales from the central region of *Lepomis macrochirus*. (A) Scales were imaged between the lateral line and pectoral fin in the area ventral to the spinous dorsal fin. (B) Grayscale image of the opercular scale surface – all panels show scales in this anatomical position. (C) Scales in this region are ctenoid. We show the surface in three-dimensions as a colored elevation map with a scale bar. (D) The black line in C is shown as a profile, where the mean height is zero. The posterior fields correspond to the plateaus in D and are approximately 1.9 mm long with deviations of 40–60 μm in elevation. Small deviations on the plateaus correspond to circuli and ctenii. (E) Three-dimensional data are shown at an oblique angle with a 10% height amplification – the scale bar from C still applies to E. (F) μCT scan of a single scale from this region with sagittal and transverse cross-sections that show small gaps between radii. Scale has a relatively blunt posterior margin.

Using the 3D models of the scales, we used Mimics to measure six variables for each of the three scales from each region: scale thickness, scale length, scale height, ctenii length, radii count, and scale aspect ratio. We measured scale thickness in the mediolateral axis at the approximate geometric center of the scale, scale length as the length in the anteroposterior axis at approximately 50% of its height, scale height in the dorsoventral axis at approximately 50% of its length, and ctenii length as the length of a single chosen ctenus. We also counted the number of radii present on each scale – radii are radially oriented thin regions or gaps (where ossification is reduced or lacking) in the bony scale matrix on the anterior portion of each scale (see panel F in Figs. 3–7). Scale aspect ratio was calculated by dividing scale height by scale length.

3. Results

3.1. Qualitative scale morphology

Figs. 2–7 present analyses of scales from the six different body surface regions we sampled in the following order: opercle, dorsal, central, ventral, peduncle, and tail. In all scales, growth rings (circuli) are visible on the posterior field. Radial gaps in the anterior field, called radii, are also evident in μCT images of single whole scales (panel F in Figs. 3–7).

Different regions of the body show clear differences in scale morphology, both in single whole scales and scaled surfaces. One of the most obvious differences is that scales on the opercle (Fig. 2) are cycloid with smooth posterior edges, while scales elsewhere on the body (Figs. 3–7) are ctenoid with small interlocking spines on the posterior field. Even on scales with ctenii, there are different proportions of ctenii coverage in different regions of the body – for example, dorsal scales (Fig. 3) have fewer ctenii than central scales (Fig. 4). Scales on the opercle (Fig. 2) also vary more in posterior field shape and whole scale shape than other regions.

There are also qualitative differences among the μCT-scanned whole scales (panel F in Figs. 2–7). Opercle scales are ellipsoid in shape, dorsal scales have more rounded corners, peduncle scales have flared anterior corners, and tail scales have a slightly pointed posterior edge. Also, radii in the anterior portion of bluegill scales differ among different regions. Notably, opercle scales have no radii (Fig. 2F), and dorsal scales have the widest radii, giving them the widest gaps in their anterior field (Fig. 3F).

Elevation profiles for each region are shown in panel D of Figs. 2–7. Note that each profile shows three to four posterior fields, each indicated by the larger plateaus in each graph. Posterior fields range in peak-to-valley heights from 35 μm to 125 μm: opercle posterior fields show peak-to-valley heights from 50 to 100 μm, dorsal from 40 to 80 μm, central from 35 to 80 μm, ventral from 40 to 70 μm, peduncle from 60 to 75 μm, and tail from 75 to 125 μm (panel D in Figs. 2–7). Color scale bars in panel C of Figs. 2–7 also show the elevation range across the entire surface.

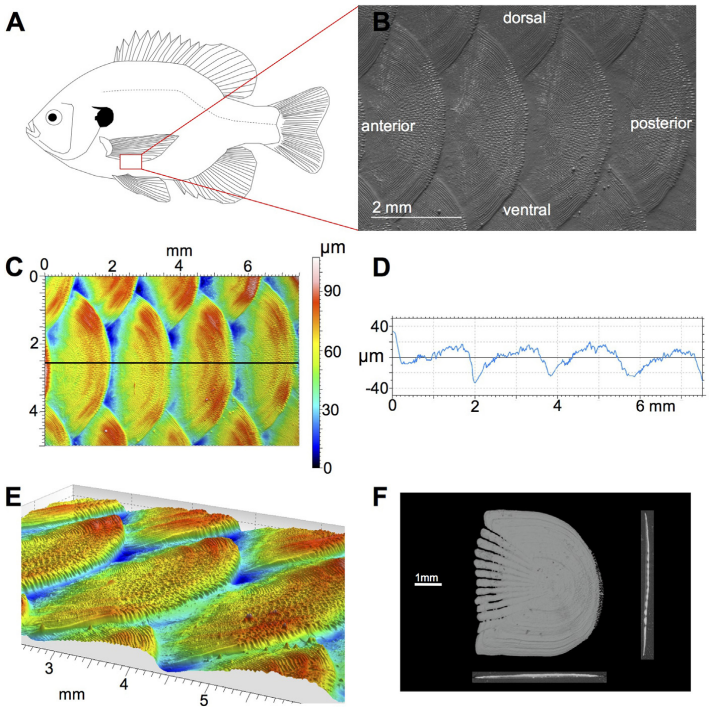

Fig. 5. Scales from the ventral region of *Lepomis macrochirus*. (A) Scales were imaged on the ventral surface of bluegill sunfish, between the pectoral fin and the pelvic fin. (B) Grayscale image of the scale surface – all panels show scales in this anatomical position. (C) Ventral scale surface in three-dimensions shown as a colored height map with a scale bar. (D) An elevation profile graph along the black line in C shows topography of the scaled surface – the hills are the posterior fields of scales, which are around 1.8 mm long with peak to valley heights of 30–50 μm. Oscillations in the height of the line in the plateau regions are caused by the circuli and ctenii. (E) An oblique view of the surface with elevation visually exaggerated by 10% to illustrate the 3D nature of these data. (F) Whole scales were imaged with μCT and a representative ventral scale is displayed, including sagittal and transverse cross-sections. Ventral scales have radii, ctenii, and a more rounded posterior edge. Radii are similar to those in central body scales.

3.2. GelSight results

Using GelSight we were able to measure 39 variables, which included 30 surface metrology variables and 9 parameters of size, shape, and ctenii coverage on posterior fields. Because of our large number of exploratory variables, we first reduced the number of variables for analyses, specifically to remove highly correlated variables. We used a correlation matrix to find variables that were the most positively or negatively correlated with one another. Because highly correlated variables show similar trends, we then removed variables until we had a set of only weakly correlated variables (correlation coefficients with an absolute value <0.82, although most are <0.6). This process left us with seven standard surface metrology variables: root-mean-square roughness, skew, kurtosis, texture direction, texture aspect ratio, mean hill area, and peak density, and two morphometric variables: posterior field aspect ratio, and percent of ctenii coverage. The variables that show significant trends are discussed below and incorporate aspects of 3D, 2D, and linear measurements. Although choosing one variable from a group of correlated ones can be arbitrary, we chose these variables for further analyses because they are both commonly used in surface metrology studies (Whitehouse, 1994) and more easily understood than other metrics.

With these nine variables, we used a MANOVA to test for differences among the six regions of the body. Differences among individuals are much smaller than the differences among scale regions (Fig. 8). The MANOVA showed a significant difference in scale surface structure among body regions: Wilks: $p = 0.0018$, Pillai: $p = 0.0027$. To display this result, we use a discriminant function analysis, which creates discriminant functions composed of the nine variables that best group the data by body region (Fig. 8A). Our first discriminant function explains over 75% of the variability between groups, while our second discriminant function explains nearly 14% (Fig. 8A). With MANOVA results indicating differences among scale patches from different regions of the body, we then ran post hoc ANOVAs on each variable to determine which were the ones contributing to differences among scale patches. Four variables showed significant trends: percent of ctenii coverage ($p = 0.0036$), aspect ratio ($p = 0.0057$), skew ($p = 0.035$), and texture direction ($p = 0.038$). A Tukey HSD test was then performed on each significant variable to see which specific regions of the fish differed with respect to each variable using a standard alpha level of 0.05. These results are presented graphically in Fig. 8B–E, with statistical groups shown by the grey and black lines at the top of each graph.

As seen in Fig. 8B, the percent of ctenii coverage shows two groups with much overlap; ctenii coverage on tail scales is greater than on opercle and dorsal scales, while ctenii coverage on ventral scales is greater than on opercle scales (Tukey HSD; tail–opercle: $p = 0.004$, tail–dorsal: $p = 0.026$, ventral–opercle: $p = 0.016$). In general, we observe more ctenii coverage as we move ventrally on the fish from dorsal to central and then ventral scales, and ctenii coverage is higher on scales from the posterior part of the fish on the

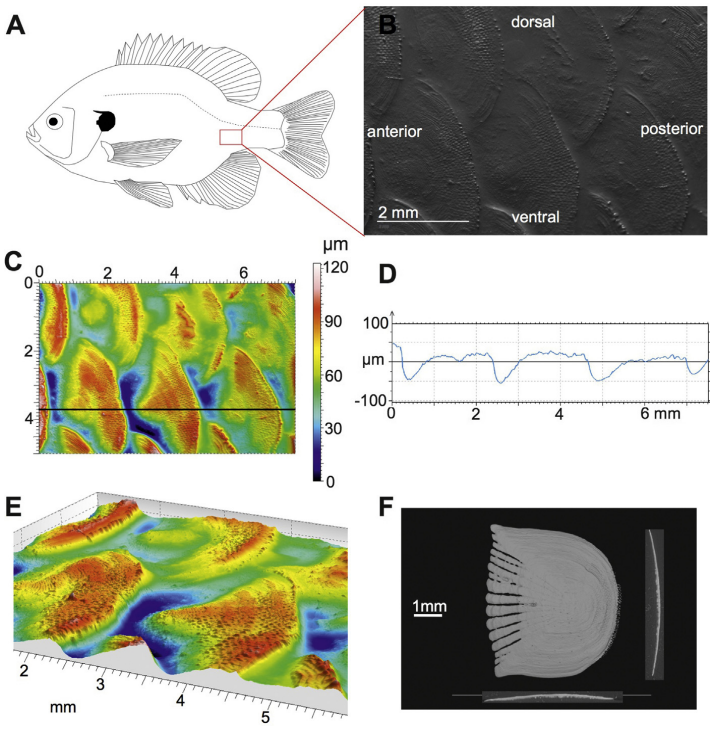

Fig. 6. Scales from the peduncle region of *Lepomis macrochirus*. (A) Scales were imaged between the lateral line and posterior base of the anal fin. (B) Grayscale image of the surface – all panels show scales in this anatomical position. (C) Ctenii are present and ctenii fields are triangular. Scale surface in three-dimensions as a colored elevation map with a scale bar. (D) An elevation profile graph along the black line in C shows topography. The plateaus are posterior fields – around 2.2 mm long and showing peak to valley heights of 60–80 μm. (E) Oblique view of this surface with elevation exaggerated by 10% to illustrate the 3D nature of these data. (F) μCT reconstruction of an anterior peduncle scale is displayed, including sagittal and transverse cross-sections. Peduncle scales show radii, ctenii, and have rounded posterior margins with flared dorsal and ventral edges. Radii nearest the lateral edges are not fully open.

peduncle and tail regions. Values fluctuate from around 10% ctenii coverage of the posterior field in the dorsal region to 35% in the tail region.

Fig. 8C shows the relationship between aspect ratio of the posterior field and region of the body. We find that posterior fields of opercle scales have a smaller aspect ratio than those on the central and ventral regions (Tukey HSD; opercle–central: $p = 0.0073$, opercle–ventral: $p = 0.0047$). Aspect ratio is lowest on the opercle region and increases from dorsal to central on the body of the fish.

Fig. 8D shows that skew is lower in the tail region than it is in the peduncle region (Tukey HSD, peduncle–tail: $p = 0.022$). Skew is a surface metrology metric where positive values indicate a predominance of peaks on the surface, whereas negative values indicate more valleys. The peduncle region is the only region with positive skews, although values for all regions of the bluegill are close to zero, indicating that surfaces contain equivalent peaks and valleys – evident from the profile lines given in panel D of Figs. 2–7.

Finally, in Fig. 8E we show the texture direction over different regions of the body. Texture direction is the direction of the primary pattern of a surface and is measured in degrees counterclockwise relative to the y-axis. A texture direction value of 90° means the prominent pattern of the surface would be arranged along the x-axis of the images (left to right in images presented). Although there are no differences between groups with a Tukey HSD test using a 0.05 alpha level, texture direction shows a significant overall effect, indicating that while texture differences among any pair of regions is small, significant variation still exists across all regions (considered together) in this metric.

3.3. μCT results

Measurements from μCT reconstructions include scale length, height, thickness, ctenii length, number of radii, and scale aspect ratio, and these data are shown in Fig. 9. Scale length is measured along the anteroposterior axis, scale height is measured along the dorsoventral axis, and scale thickness is measured in the mediolateral axis (for details see Section 2.3). MANOVA analysis shows a difference among scales from different body regions using these six variables (Wilks: $p < 0.001$, Pillai: $p < 0.001$).

Scales from different regions show differences in length (ANOVA, $p < 0.001$), although the pattern among regions is complex (Fig. 9A). Scales from the opercle are shorter in length than scales from the central, ventral, peduncle, and tail regions (Tukey HSD; opercle–central: $p < 0.001$, opercle–ventral: $p < 0.001$, opercle–peduncle: $p = 0.0073$, opercle–tail: $p = 0.0012$). Additionally, dorsal scales are shorter than scales from the central, ventral, and tail regions (Tukey HSD; dorsal–central: $p = 0.0067$, dorsal–ventral: $p = 0.017$, dorsal–tail: $p = 0.041$). Overall, scales are shorter on the opercle and dorsal regions (~4 mm) and longer on the rest of the body (~5 mm).

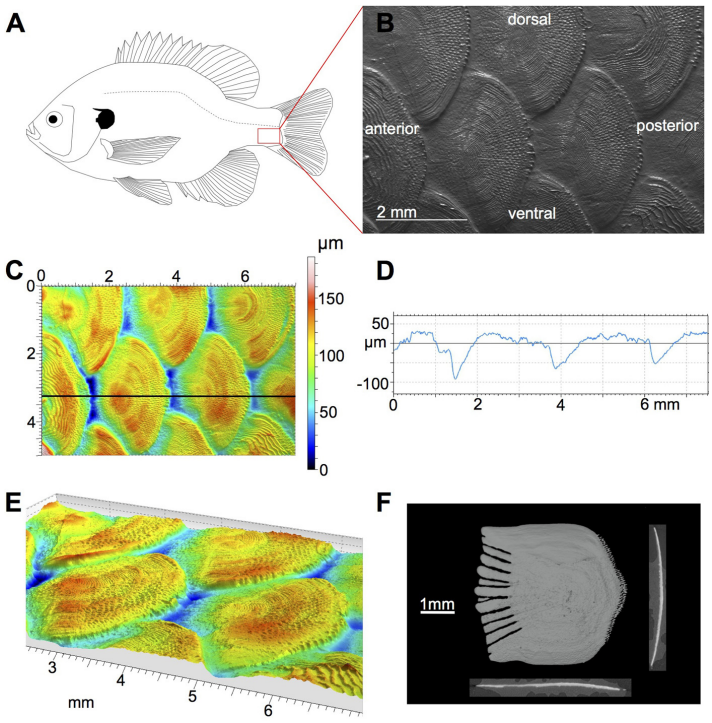

Fig. 7. Scales from the tail region of *Lepomis macrochirus*. (A) Scales were imaged above the hypural plate at the base of the tail, and below the lateral line. (B) Grayscale image of the surface – all panels show scales in this anatomical position. Ctenii present. Note the replacement scales with more distantly spaced circuli in the bottom right, top right, and left edges of the image. (C) The scale surface is shown in three-dimensions as a colored elevation map with a scale bar. (D) An elevation profile graph from the black line in C shows the topography of the scaled surface – the plateaus are the posterior fields, which are around 2.4 mm long and show vertical deviations of 80–120 μm. (E) Oblique view of the surface with elevation visually exaggerated by 10% to illustrate the 3D nature of these data. (F) Whole scales were imaged with μCT and a single tail scale is displayed, including sagittal and transverse cross-sections. Scales have dull-pointed posterior edges, straightened lateral edges, and slightly flared anterior margins. Radii nearest the lateral edges are not fully open.

Scales are also different in height (ANOVA, $p < 0.001$) as shown in Fig. 9B. Opercle scales are shorter in height compared to scales from the central, ventral, and peduncle regions (Tukey HSD; opercle–central: $p < 0.001$, opercle–ventral: $p = 0.0014$, opercle–peduncle: $p = 0.0026$). Similarly, dorsal scales are shorter than scales from the central, ventral, and peduncle regions (Tukey HSD; dorsal–central: $p = 0.0055$, dorsal–ventral: $p = 0.023$, dorsal-peduncle: $p = 0.045$). Tail scales are also shorter than central scales (Tukey HSD; tail–central: $p = 0.020$).

Fig. 9C shows that the thickness of scales is different on different regions of the fish (ANOVA, $p < 0.001$). Scales from the opercle region are thinner than scales from the central, ventral, and peduncle regions (Tukey HSD; opercle–central: $p = 0.0024$, opercle–ventral: $p = 0.025$, opercle–peduncle: $p = 0.013$). Moreover, scales from the dorsal region are thinner than scales of the central, ventral, peduncle, and tail regions (Tukey HSD; dorsal–central: $p < 0.001$, dorsal–ventral: $p = 0.0011$, dorsal–peduncle: $p < 0.001$, dorsal–tail: $p = 0.011$). Opercle and dorsal scales are thinnest, at about 65 μm, while central, ventral, and peduncle scales are much thicker, at around 110 μm.

Fig. 9D shows that length of ctenii is different among different regions on bluegill (ANOVA: $p < 0.001$). The only statistical difference here is that scales from the opercle region have no ctenii, in contrast to ctenii being present on all other scale regions (Tukey HSD: all pairwise comparisons between opercle and other regions $p < 0.001$). In the present study we have chosen to characterize the cycloid scales of the opercle as having ctenii of zero length, but an argument could be made for treating ctenii presence as a categorical variable. However, some research suggests that with growth of a fish, cycloid scales become ctenoid scales in some species, indicating that some cycloid and ctenoid scales are on the same ontogenetic spectrum of scale types (Burdak, 1986). It is possible that finer differences would be seen with a larger sample size. Dorsal, central, ventral, peduncle, and tail regions have ctenii about 110 μm long.

Fig. 9E shows that scale radius number differs among regions (ANOVA: $p < 0.001$). Opercle scales are different from other regions because they have either very few or no radii (Tukey HSD: all pairwise comparisons between opercle and other regions $p < 0.001$). The pairwise comparison between the counts of central versus peduncle radii is close to significance ($p = 0.081$) – indicating a larger sample size could reveal significant differences.

Fig. 9F shows that scale aspect ratio is different among regions on bluegill (ANOVA: $p = 0.033$). Tail scales have a lower aspect ratio than peduncle scales (Tukey HSD; tail–peduncle: $p = 0.045$). Lower aspect ratios indicate that scales are shorter in the dorsoventral axis or longer in the anteroposterior axis. Ventral and opercle scales have more variability in aspect ratio compared to other scales, as shown by the standard error bars in Fig. 9F.

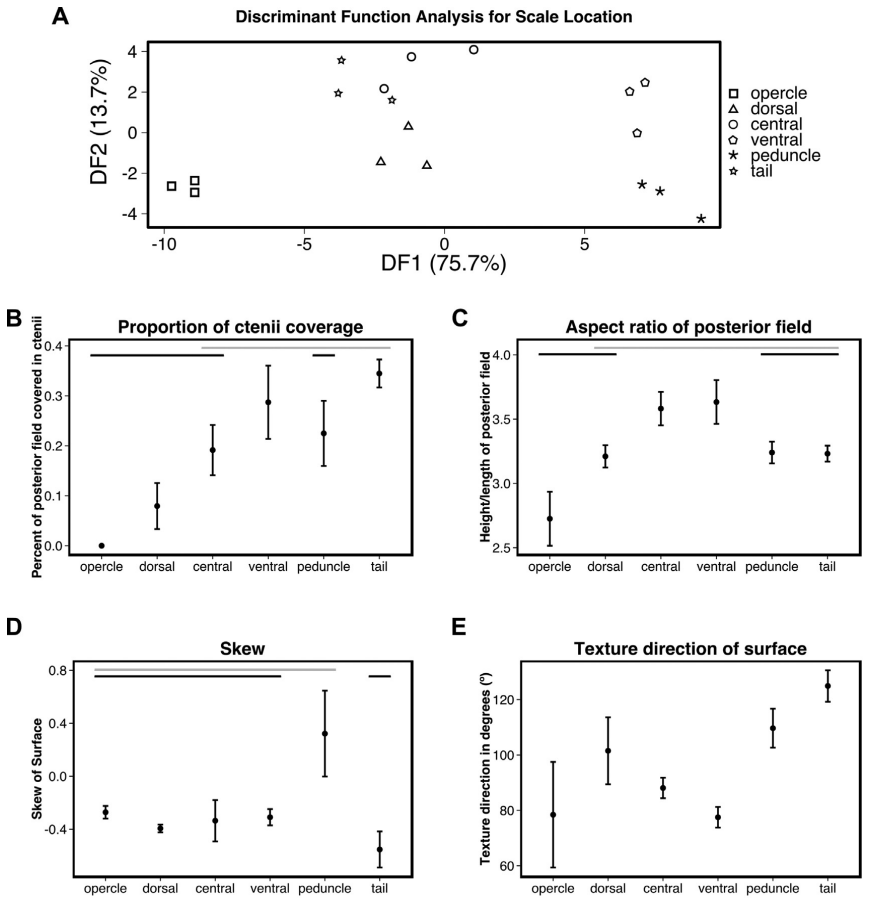

Fig. 8. Scale surface morphology data from GelSight, comparing measurements from different body regions. (A) Discriminant function analysis using 9 different variables categorized with scale location. Discriminant function 1 (DF1) accounts for 75.7% of the diversity among groups, while discriminant function 2 (DF2) accounts for 13.7%. Panels B–E show variables that demonstrate significant differences among scale locations. Black and grey bars at the top of graphs indicate the groups that are not statistically different using Tukey HSD test. Bars are ± 1 standard error and points are means. (B) Percent of the posterior scale field covered in ctenii. (C) Aspect ratio (height divided by length) of the posterior field within scales. (D) Skew and scale location. (E) Texture direction measured with respect to the y-axis, with clockwise turns in texture direction resulting in positive angle values. Although the ANOVA shows a significant effect with this variable, there are no differences among groups using Tukey HSD. Values are near 90 degrees, which is expected for horizontally arranged scales.

4. Discussion

In the present paper we present data on morphological differences among in situ patches and individual scales from six different regions of the body of bluegill sunfish. We collected our data using both a new surface analysis technique that allows 3D reconstruction of a fish's surface, and μCT to focus on the morphology of individual scales. We found numerous differences among regions of the body in both the shape and pattern of scales.

Fish scales have been the subject of research on topics ranging from species description (Jordan and Evermann, 1898; Miller, 1945) and analysis of age and growth (Everhart, 1950; Lane, 1954; Beardsley, 1967) to population discrimination (Barlow and Gregg, 1991; Margraf and Riley, 1993; Unwin and Lucas, 1993). Scales can be well preserved in the fossil record, and have been used to characterize species assemblages (Shackleton, 1987; McDowall and Lee, 2005), inform diet and food webs (Maisey, 1994), and describe extinct taxa (Goodrich, 1907; Zylberberg et al., 2010). Scale morphology has also been used to infer taxonomic relationships among fish taxa, starting notably with Louis Agassiz and his categorization of fish diversity based on scale morphology, but continuing to the present day (Agassiz, 1833; Goodrich, 1907; Kobayasi, 1955; Randall, 1955; Roberts, 1993; Kuusipalo, 1998; Lippitsch, 1998).

However, detailed descriptions of scale morphology and variation over the body have remained limited due to the lack of a method for imaging surface topography on patches of overlapping scales. Scanning electron micrographs and alizarin-stained scales provide clear images for 2D and linear morphometrics, but are not suitable for quantitative metrology and 3D analysis, or for examining the relationships among scales in situ on the body. Perhaps in part due to the general lack of quantitative imaging of fish scales, inferences about the hydrodynamic and locomotor function of scales have remained mostly indirect and speculative. Even basic questions such as "how rough is the surface of a fish?" and

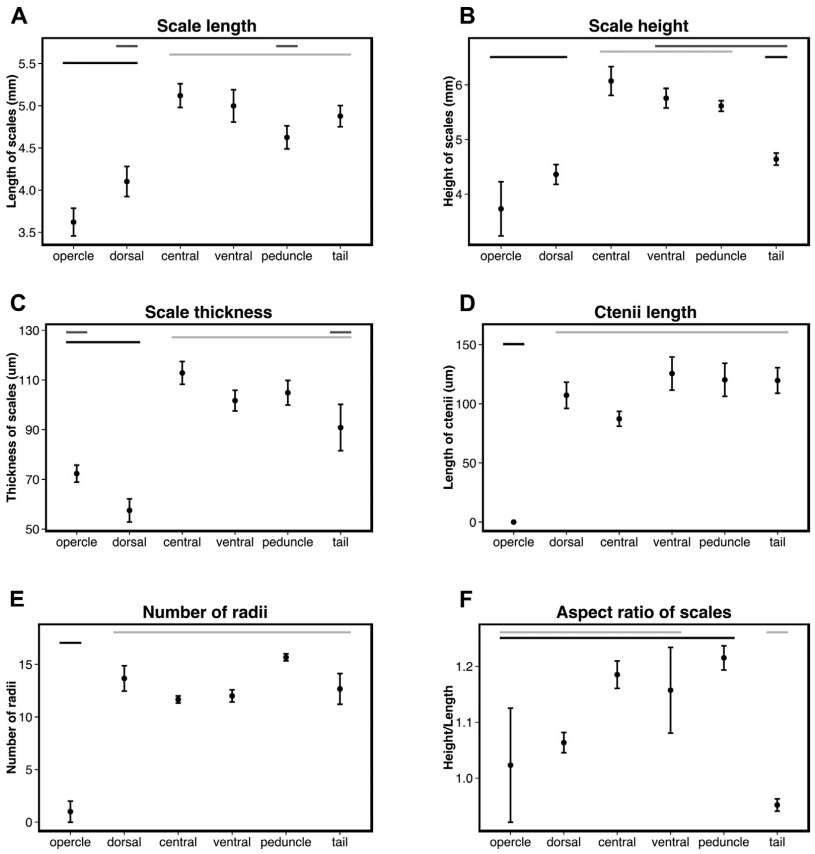

Fig. 9. Graphs of scale μCT data for scales all taken from the same individual to show differences in morphology among scales from different body regions. Lines at the top of graphs refer to groups determined with post-hoc Tukey HSD tests. Points are means and error bars are ± 1 standard error. (A) Scale length in the anterior-posterior direction. Scales from opercle and dorsal regions have the smallest lengths (3.5–4.3 mm) and bluegill scales show a range of lengths between 3.5–5.25 mm. (B) Scale height (dorsal–ventral direction). Scales from opercle, dorsal, and tail regions have the smallest heights, and variation of all scales is between 3 and 6.5 mm. (C) Scale thickness. Scales from dorsal and opercle regions are thinnest. Thickness ranges from 50 to 120 μm. (D) Ctenii length; all ctenii appear similar in length where present. Opercle scales have no ctenii. (E) Radii counts from different scale regions. Opercle scales have zero or few radii, while other scales have between 11 and 16. (F) Aspect ratio of whole scales. Scales are usually larger in height than length, except for scales on the tail and opercle regions.

"how does roughness vary across a fish's body surface?" have not been quantitatively addressed. Without this information, hypotheses about either how water flow is altered by scale morphology or regarding the effects of scales on boundary layer flows cannot be specified. To our knowledge, the present data on bluegill represent the first analysis of the 3D surface structure of scale patches and the use of μCT scans to investigate dimensional variation in individual scales around the body.

4.1. Bluegill scale morphology

Bluegill scales vary both qualitatively and quantitatively among different regions of the body. Figs. 2–7 illustrate scales from our six chosen regions. We particularly note the presence of ctenoid scales on all regions except the cycloid-scaled opercle, but differences do not end there.

Of our nine GelSight-measured variables for in situ scale patches, ctenii coverage, posterior field aspect ratio, skew, and texture direction show significant differences among different regions of the bluegill. In addition, μCT data on individual scales show differences in length, height, thickness, ctenii length, number of radii, and aspect ratio. Both the GelSight and μCT variables often show differences in the opercle, dorsal, peduncle, or tail regions compared to others, leading us to hypothesize that these regions may be good candidates for observing within-species scale diversity in other species. For example, to study differences in scale morphology within a species, scales from the opercle, dorsal, peduncle, and tail regions may be important to sample because these regions are most often different from other regions in the dataset we present here. Furthermore, because these regions appear to be most different, they may hold information on the functional significance of scale diversity – especially if similar patterns are seen in other species as some other studies suggest (Burdak, 1986; Grande and Bemis, 1998; Ibañez et al., 2009). Scales from the central and ventral regions are always very similar in our analyses and often have average values for metrics that we quantified; these may be good regions to use when investigating differences between species or describing the scales of a species.

Differences in the shape of the posterior fields are evident in our GelSight images of scale patches (panel B in Figs. 2–7). These differences are reflected in our analysis of posterior field aspect ratio (Fig. 8C) where we find the lowest aspect ratio on the opercle, followed by dorsal, peduncle, and tail regions, and then central and ventral regions. This aspect ratio pattern is mirrored in the analysis of whole scales (Fig. 9F) with a few differences. First, the aspect ratio of whole opercle scales has a much higher variability (Fig. 9F) than that of other regions, evidence that scale shape is more variable in the opercle than in other regions. Second, the aspect ratio of whole peduncle scales is high compared to that of other regions, but peduncle posterior fields have average aspect ratios. This last point is evidence that posterior field shape is not only the result of the shape of the whole scale; instead, scale shape interacts with the arrangement of neighboring scales to create different posterior field shapes. However, the general agreement between posterior field and whole scale aspect ratio patterns may indicate that whole scale shape often dictates posterior field shape, at least in bluegill.

In the order of largest to smallest, the largest scales in length, height, and thickness are the scales of the central, ventral, peduncle, and tail regions (Fig. 9A–C). Dorsal and opercle scales are overall smallest in those three simple size measurements. Ctenii length saw no pattern besides the lack of ctenii on opercle scales, although it is possible that slight differences exist, because central ctenii appear to be shorter than others (Fig. 9D). Radii show a pattern where opercle radii counts are different from those of other regions (Fig. 9F), yet radii counts appear to have small standard deviations in the central, ventral, and peduncle regions. Although we were unable to detect a significant difference between radii counts with our sample size, the pattern we describe here suggests a significant trend may emerge with further study and a larger sample size. Because radii are gaps in the ossification of scales, they naturally provide increased flexibility for scales. It is interesting to note that the highest radii counts come from regions of the body that are either naturally curved (dorsal) or experience higher lateral curvature during swimming (the caudal peduncle and tail). Because the opercular region does not bend during swimming, perhaps it is unsurprising that opercle scales have almost no radii, and hence, limited expected flexibility.

4.2. Functional significance of scale structures for solid mechanics

Research into the solid mechanics of fish scales has largely focused on biomimetic applications of fish-scale-like armor (Vernerey and Barthelat, 2010; Yang et al., 2012; Chintapalli et al., 2014). Much of this research has investigated thickened ganoid scales typical of Polypteridae and Lepisosteidae (Bruet et al., 2008; Song et al., 2011) but the mechanical properties of elasmoid scales as seen in bluegill and most bony fishes have also been investigated (Zhu et al., 2012; Browning et al., 2013). Here we present several hypotheses relevant to the solid mechanical function of fish scales based on the features that we have observed in bluegill scales.

First, the slight curvature of scales may function to stiffen scales in specific loading regimes. Scales appear to be curved so that their interior surfaces, facing medially, are concave (cross-sections in panel F of Figs. 2–7). This curvature would be expected to increase bending stiffness of the scale and allow it to resist bending in the anterior–posterior plane, which could be important in resisting injury or local deformation during swimming and escape events. Current mathematical and physical models of scales do not take scale curvature into account (Vernerey and Barthelat, 2010; Browning et al., 2013). Presumably scales contact and slide past one another during body and fin undulation (scales can be present on fins), but the degree and nature of scale-to-scale relative motion is unknown. It is also possible that scales could store elastic energy during either standard undulatory locomotion or high lateral bending maneuvers such as escape responses. Any elastic energy stored would be returned to the fish to accelerate lateral bending of the body in the opposite direction and scale curvature would affect the amount of energy stored. This hypothesis could be examined by first understanding the kinematics of fish scales during different modes of locomotion and then determining the extent of scale movement and bending in vivo.

Second, the circuli and other microroughness features on scale surfaces may function to limit tensile stresses to the valleys between circuli during bending of the scale (Yang et al., 2012). Limiting tensile stress in this way will minimize tensile stress during the bending of scales, which could affect the amount of stress necessary to produce a given amount of bending.

Third, circuli and other microroughness features of both scale medial and lateral surfaces could increase the second moment of area for scales. Increasing the second moment of area by placing material farther from the axis of bending would increase the stiffness of scales, with implications for swimming and protection as noted above.

Fourth, fields of interlocking ctenii at the posterior edge of scales may function as regions of flexibility. Because ctenii are made of many interlocking structures, it is reasonable to assume they are not as stiff as the body of the scale made of solid ossified tissue. The interlocking ctenii would create decreased resistance to flexibility, which could be important for lessening the force to bend arrays of scales when they are touching. This hypothesis is dependent upon the kinematics of scales during swimming and assumes that the posterior part of a scale will touch the scale posterior to it, creating a bending force.

A fifth hypothesis relevant to scale function is that radii may allow increased scale flexibility, thereby reducing body bending forces (Taylor, 1916) and the locomotor cost of transport. Radii are gaps in the ossified layer on scales, found on the anterior portion of scales on bluegill and other fishes (panel F in Figs. 3–7) (Daniels, 1996). Radii may decrease the bending stiffness of scales and these gaps could provide flexibility without sacrificing protective functions because radii are located under the surface of the neighboring scales in the anterior direction.

A final hypothesis on the solid mechanics of scales is that the microroughness of scales, including circuli and ctenii, could provide a substrate for the attachment of the epidermal and mucous layers atop fish scales. The epidermis and mucus could decrease friction among overlapping scales and make it easier for scales to slide past one another as the body bends, allowing for greater amounts of body curvature before scales begin to bend and resist body curvature. Interactions among biomimetic 3D-printed scales have been suggested to increase the cost of transport during locomotion, and scale mobility in sharks may act to decrease the energy required to bend the body (Wen et al., 2015).

4.3. Functional significance of scale structures for fluid mechanics

Scale morphology not only has relevance for solid mechanics and how fish body bending occurs, but for fluid mechanics as well. Several features of the pattern of scale variation across the body suggest functional hypotheses for future experimental testing. First, one hypothesis regarding scale function is that ctenoid scales increase turbulent energy in the boundary layer. This hypothesis originated in the Russian literature (Burdak, 1986), which states that spiny ctenoid scales create organized turbulence to either create or maintain a turbulent boundary layer, thereby delaying boundary layer separation and the associated increase in pressure drag. Although laminar boundary layers generate less friction drag than turbulent ones, turbulent boundary layers have a greater energy and are less prone to separation (Anderson et al., 2001; Anderson, 2005). If a fish were to 'trip' the boundary layer

from laminar to turbulent, it could therefore decrease drag by being less likely to incur separation – the spines on scales could be used as a turbulator (turbulence generator) in this manner. Our limited knowledge of swimming fish boundary layers shows that fish generate mainly laminar boundary layers (Anderson et al., 2001) at slow to moderate swimming speeds. However, turbulent boundary layers can occur posteriorly on the body and the tail, and during higher-amplitude motions such as escape responses. Also, larger fish may incur turbulent boundary layers proportionally further anteriorly on their bodies simply due to their large length – a factor in determining the Reynolds number and organization of boundary layer flows. For example, if the laminar-to-turbulent transition happens at 10 cm down the length of both a 15 cm salmon and a 60 cm salmon, the transition occurs proportionally further anteriorly on the 60 cm fish and we may expect the surface structure of the fish to reflect this. The hypothesis that ctenii increase turbulent energy in the boundary layer is often presented as if it was well supported (Bone and Moore, 2008; Helfman et al., 2009), but in fact we are not aware of any experimental studies that have investigated this idea explicitly.

Second, the increased ctenii coverage we observe towards the tail could indicate the use of more turbulators, such as ctenii, to delay separation of the boundary layer as the fluid's pressure gradient changes further back on the fish. We observed an increase in the coverage of ctenii as we move ventrally and posteriorly on the body (Fig. 8B), and as above, ctenii may be acting as turbulators to create a turbulent boundary layer and delay separation. In addition, it has been shown that both streamwise (parallel to the flow) riblets and the riblet-like features of shark's placoid scales reduce drag in turbulent boundary layers (Dean and Bhushan, 2010; Oeffner and Lauder, 2012; Wen et al., 2014) and the patterns of spines on fish scales could function similarly to reduce drag where there is turbulence. Furthermore, the increased ctenii coverage ventrally on the bluegill body might be explained by the increased turbulence created by pectoral fin oscillation during swimming at speeds of less than one body length per second (Gibb et al., 1994; Drucker and Lauder, 1999). In short, more ctenii are found where there appears to be increased turbulent flow, indicating that increasing the number the number of ctenii may be useful for controlling turbulence intensity near the body.

A related hypothesis for scale function is that the transition from cycloid scales on the anterior part of the body to ctenoid scales on the posterior part of the body could indicate the transition from a laminar to a turbulent boundary layer (Aleyev, 1977). Here, anterior cycloid scales would reduce drag in a laminar boundary layer by virtue of their smooth surface (Aleyev, 1977; Burdak, 1986). If the boundary layer becomes turbulent after the gill opening where fluid is injected into the boundary layer (Tytell and Alexander, 2007), then spiny-edged ctenoid scales could organize turbulence to prevent separation, as above. To test this hypothesis, experimental measurements of boundary layer flows could be made to determine if there is a match between where scales transition from cycloid to ctenoid and where the boundary layer transitions from laminar to turbulent flow.

Third, one of the surface metrology parameters measured from GelSight, skew, shows a pattern where the only positive values are seen on the peduncle region. Skew is a measurement of the dominance of peaks versus valleys on the surface, with positive values indicating more peaks. For reference, most sandpapers have skew values from 0.7 to 1.0 (a flat surface with grains that create peaks) and our data shows skew values of about 0.4 for the peduncle, indicating dominance of peaks. The peduncle of fish experiences larger amounts of bending than other regions, and the flow speed of the fluid near the peduncle is increased due to higher body oscillation amplitudes. In addition, the peduncle is a region of complex three-dimensional flow (Nauen and Lauder, 2001). Perhaps the positive skew values in the peduncle region have some relationship to the complex and possibly separated flows in this region (Anderson et al., 2001).

Although there has been discussion about the role of ctenii in hydrodynamics (see above), it is possible that the circuli may also function as turbulators. Circuli are concentric growth rings on the body of scales that protrude a small amount (~5 μm in bluegill) from the scale surface. On the dorsal and ventral areas of each scale, these circuli have streamwise grooves, while the posterior parts of scales have circuli perpendicular to flow. Circuli could generate turbulence to create or maintain a turbulent boundary layer. Circuli could also concentrate fluid shear stress on their ridges while experiencing a drop in shear stress over valleys, with the effect of decreasing friction drag overall.

Finally, the epidermis and mucus that cover the body and scales of many fish may have a profound effect on scale function. It is possible that the mucus layer and epidermis of live fish covers or partially obscures some of the morphological features described above. Values for thickness of the epidermis for trout and salmon vary from about 30 μm to 90 μm (Fast et al., 2002), which if similar in bluegill, may obscure microroughness created by circuli. Ctenii appear to project through the epidermis and mucus coating, as they are visible in experimental GelSight imaging of the surface of live bluegill swimming (D.K.W., unpublished observations). However, the epidermis may also conform to the scale surface, allowing many of the larger features to affect the fluid moving past the body.

Our study used preserved specimens but the epidermis is still sometimes present as a smooth area with small 10 μm bumps (perhaps goblet cells) in the anterior part of posterior fields of the images shown (Figs. 2B and 7B). However, the epidermis is likely distorted and damaged by the preservation process and live fish may look quite different. Mucus is almost certainly not present in our images, as the fixation and preservation process often causes mucus to slough off. If the epidermis and mucus of fish normally cover features such as circuli and ctenii, then these structures are not likely to have a direct effect on the boundary layer of a swimming fish, thereby limiting the fluid dynamic effect of several scale features. In fact, circuli and fields of ctenii may have a role in retaining the mucus coat on the scale surface.

Despite this range of hypotheses concerning scale function, the nature of fluid flow at the level of fish scales remains unknown, and so the effect of scale microstructure on flow dynamics over the body of swimming fishes is an area very much in need of future study.

4.4. The future of 3D fish scale imaging

With the use of both established μCT techniques and the new 3D surface imaging provided by GelSight, we have shown that it is possible to collect quantitative data on fish scale morphology. Describing scale morphology in 3D is crucial to understanding any potential hydrodynamic interactions scales may be having with the external fluid, and such data may also shed light onto other functional roles for scales. The scales of more species could be studied with these techniques to measure patterns of scale morphology in a phylogenetic context, which may lead to further hypotheses about the functional roles of scale 3D structure. Furthermore, it would be interesting to see if the general patterns across the body that we observed in bluegill hold in other species. GelSight is a powerful imaging tool that can be used to study scales from fossil fish to the surfaces of live fish. Additionally, 3D shape data allows us to create physical models of fish surfaces using 3D printing techniques and then test their performance during both swimming and static tests (Wen et al., 2014, 2015). In this way we can link form to function by testing the mechanical and hydrodynamic performance of different

scale structures using physical models and imaging the surface of live fish during locomotion.

Acknowledgements

This work was supported by ONR MURI Grant N000141410533 monitored by Dr. Bob Brizzolara and NSF GRF 2014162421 awarded to D.K.W. The authors thank Bill Yost and Kimo Johnson of GelSight for their assistance with the GelSight imaging technique, and Karsten Hartel and Andy Williston of the Harvard MCZ Fish Department for their assistance and suggestions. Special thanks to James Weaver for his assistance with this project and for introducing us to GelSight. Many thanks also to Stacy Farina and Kelsey Lucas for their helpful comments on the manuscript.

References

Agassiz, L., 1833. Recherches sur les Poissons Fossiles, vol. 2. Imp. Petitpierre, Neuchatel.
Aleyev, Y.G., 1977. In: Junk, W. (Ed.), Nekton. The Hague.
Anderson, E.J., McGillis, W.R., Grosenbaugh, M.A., 2001. The boundary layer of swimming fish. J. Exp. Biol. 204, 81–102.
Anderson, J.D., 2005. Ludwig Prandtl's boundary layer. Phys. Today 58, 42–48.
Barlow, C.G., Gregg, B.A., 1991. Use of circuli spacing on scales to discriminate hatchery and wild barramundi: *Lates calcarifer* (Bloch). Aquac. Fish. Manag. 22, 491–498.
Batts, B.S., 1964. Lepidology of the adult pleuronectiform fishes of Puget Sound Washington. Copeia 1964, 666–673.
Beardsley, G.L., 1967. Age, growth, and reproduction of the dolphin, *Coryphaena hippurus*, in the Straits of Florida. Copeia 1967, 441–451.
Bone, Q., Moore, R.H., 2008. Biology of Fishes, 3rd ed. Taylor and Francis, New York.
Browning, A., Ortiz, C., Boyce, M.C., 2013. Mechanics of composite elasmoid fish scale assemblies and their bioinspired analogues. J. Mech. Behav. Biomed. Mater. 19, 75–86.
Bruet, B.J.F., Song, J., Boyce, M.C., Ortiz, C., 2008. Materials design principles of ancient fish armour. Nat. Mater. 7, 748–756.
Burdak, V.D., 1986. Morphologie fonctionnelle du tegument ecailleux des poissons. Cybium 10, 1–128.
Chintapalli, R.K., Mirkhalaf, M., Dastjerdi, A.K., Barthelat, F., 2014. Fabrication, testing and modeling of a new flexible armor inspired from natural fish scales and osteoderms. Bioinspir. Biomim. 9, 036005.
Cockerell, T.D.A., 1911. The scales of freshwater fishes. Biol. Bull. 20, 367–387.
Daniels, R.A., 1996. Guide to the identification of scales of inland fishes of northeastern North America. New York State Mus. Bull. 488, 1–93.
Dapar, M.L.G., Torres, M.A.J., Fabricante, P.K., Demayo, C.G., 2012. Scale morphology of the Indian goatfish, *Parapeneus indicus* (Shaw, 1803) (Perciformes: Mullidae). Adv. Environ. Biol. 6, 1426–1432.
Dean, B., Bhushan, B., 2010. Shark-skin surfaces for fluid-drag reduction in turbulent flow: a review. Phil. Trans. R. Soc. A 368, 4775–4806.
Drucker, E.G., Lauder, G.V., 1999. Locomotor forces on a swimming fish: three-dimensional vortex wake dynamics quantified using digital particle image velocimetry. J. Exp. Biol. 202, 2393–2412.
Drucker, E.G., Lauder, G.V., 2000. A hydrodynamic analysis of fish swimming speed: wake structure and locomotor force in slow and fast labriform swimmers. J. Exp. Biol. 203, 2379–2393.
Ellerby, D.J., Gerry, S.P., 2011. Sympatric divergence and performance trade-offs of bluegill ecomorphs. Evol. Biol 38, 422–433.
Esmaeili, H.R., Ansari, T.H., Teimory, A., 2007. Scale structure of a cyprinid fish *Capoeta damascina* (Valenciennes in Cuvier and Valenciennes, 1842) using scanning electron microscope (SEM). Iran. J. Sci. Technol. Trans. A. 31, 255–262.
Everhart, W.H., 1950. A critical study of the relation between body length and several scale measurements in the smallmouth bass, *Micropterus dolomieu* Lacepede. J. Wildl. Managem. 14, 266–276.
Fast, M.D., Sims, D.E., Burka, J.F., Mustafa, A., Ross, N.W., 2002. Skin morphology and humoral non-specific defence parameters of mucus and plasma in rainbow trout, coho and Atlantic salmon. Comp. Biochem. Physiol. Part A Mol. Integr. Physiol. 132, 645–657.
Flammang, B.E., Lauder, G.V., 2008. Speed-dependent intrinsic caudal fin muscle recruitment during steady swimming in bluegill sunfish, *Lepomis macrochirus*. J. Exp. Biol. 211, 587–598.
Flammang, B.E., Lauder, G.V., Troolin, D.R., Strand, T.E., 2011. Volumetric imaging of fish locomotion. Biol. Lett. 7, 695–698.
Gerry, S.P., Wang, J., Ellerby, D.J., 2011. A new approach to quantifying morphological variation in bluegill *Lepomis macrochirus*. J. Fish Biol. 78, 1023–1034.
Gibb, A.C., Jayne, B.C., Lauder, G.V., 1994. Kinematics of pectoral fin locomotion in the bluegill sunfish *Lepomis macrochirus*. J. Exp. Biol. 189, 133–161.
Goodrich, E.S., 1907. On the scales of fish, living and extinct, and their importance in classification. Proc. Zool. Soc. 1907, 751–773.
Grande, L., Bemis, W.E., 1998. A comprehensive phylogenetic study of amiid fishes (Amiidae) based on comparative skeletal anatomy. An empirical search for interconnected patterns of natural history. J. Vertebr. Paleontol., Spec. Mem. 4 (Suppl. to Vol. 18).
Helfman, G.S., Collette, B.B., Facey, D.E., Bowen, B.W., 2009. The Diversity of Fishes, 2nd ed. John Wiley and Sons, Hoboken, NJ.
Ibañez, A.L., Cowx, I.G., OHiggins, P., 2009. Variation in elasmoid fish scale patterns is informative with regard to taxon and swimming mode. Zool. J. Linn. Soc. 155, 834–844.
Jawad, L.A., 2005. Comparative scale morphology and squamation patterns in triplefins (Pisces: Teleostei: Perciformes: Tripterygiidae). Tuhinga 16, 137–167.
Jayne, B.C., Lozada, A.F., Lauder, G.V., 1996. Function of the dorsal fin in bluegill sunfish: motor patterns during four distinct locomotor behaviors. J. Morphol. 228, 307–326.
Johnson, M.K., Adelson, E.H., 2009. Retrographic sensing for the measurement of surface texture and shape. Proceedings of the IEEE Conference on Computer Vision and Pattern Recognition, pp. 1070–1077, http://dx.doi.org/10.1109/CVPR.2009.5206534.
Johnson, M.K., Cole, F., Raj, A., Adelson, E.H., 2011. Microgeometry capture using an elastomeric sensor. Proceedings of ACM SIGGRAPH, http://dx.doi.org/10.1145/1964921.1964941 (article no. 46).
Jordan, D.S., Evermann, B.W., 1898. The fishes of North and Middle America: a descriptive catalogue of the species of fish-like vertebrates found in the waters of North America, north of the Isthmus of Panama. Part 2. Bull. U.S. Nat. Mus. 47, 1241–2183.
Kendall, J.L., Lucey, K.S., Jones, E.A., Wang, J., Ellerby, D.J., 2007. Mechanical and energetic factors underlying gait transitions in bluegill sunfish (*Lepomis macrochirus*). J. Exp. Biol. 210, 4265–4271.
Kobayasi, H., 1955. Comparative studies of the scales in Japanese freshwater fishes, with special reference to phylogeny and evolution. IV. Particular lepidology of freshwater fishes. I. Suborder Isospondyli (continued). Jap. J. Ichthyol. IV, 64–75.
Kuusipalo, L.V., 1998. Scale morphology in Malawian cichlids. J. Fish Biol. 52, 771–781.
Lagler, K.F., 1947. Lepidological studies, 1. Scale characters of the families of Great Lakes fishes. Trans. Am. Microsc. Soc. 66, 149–171.
Lane, C.E., 1954. Age and growth of the bluegill, *Lepomis macrochirus* (Rafinesque), in a new Missouri impoundment. J. Wildl. Manag. 18, 358–365.
Li, R., Adelson, E.H., 2013. Sensing and recognizing surface textures using a GelSight sensor. Proceedings of the IEEE Conference on Computer Vision and Pattern Recognition, pp. 1241–1247, http://dx.doi.org/10.1109/CVPR.2013.164.
Li, R., Platt, R.J., Wenzhen, Y., Pas, A., Roscup, N., Srinivasan, M.A., Adelson, E., 2014. Localization and manipulation of small parts using GelSight tactile sensing. Proceedings of the IEEE International Conference on intelligent Robots and Systems, pp. 3988–3993 http://dx.doi.org/10.1109/IROS.2014.6943123.
Lippitsch, E., 1998. Phylogenetic study of cichlid fishes in Lake Tanganyika: a lepidological approach. J. Fish Biol. 53, 752–766.
Maisey, J.G., 1994. Predator–prey relationships and trophic level reconstruction in a fossil fish community. Environ. Biol. Fishes 40, 1–22.
Margraf, F.J., Riley, L.M., 1993. Evaluation of scale shape for identifying spawning stocks of coastal Atlantic striped bass (*Morone saxatilis*). Fish. Res. 18, 163–172.
McDowall, R.M., Lee, D.E., 2005. Probable perciform fish scales from a Miocene freshwater lake deposit Central Otago New Zealand. J. R. Soc. New Zeal. 35, 339–344.
Miller, R.R., 1945. A new cyprinid fish from Southern Arizona, and Sonora, Mexico, with the description of a new subgenus of *Gila* and a review of related species. Copeia 1945, 104–110.
Nauen, J.C., Lauder, G.V., 2001. Locomotion in scombrid fishes: visualization of flow around the caudal peduncle and finlets of the chub mackerel *Scomber japonicus*. J. Exp. Biol. 204, 2251–2263.
Oeffner, J., Lauder, G.V., 2012. The hydrodynamic function of shark skin and two biomimetic applications. J. Exp. Biol. 215, 785–795.
Randall, J.E., 1955. An analysis of the genera of surgeon fishes (family Acanthuridae). Pacific Sci. 9, 359–367.
Rasband, W.S., 1997–2015. ImageJ. U. S. National Institutes of Health, Bethesda, MD, USA http://imagej.nih.gov/ij/.
Richards, R.A., Esteves, C., 1997. Use of scale morphology for discriminating wild stocks of Atlantic striped bass. Trans. Am. Fish. Soc. 126, 919–925.
Roberts, C.D., 1993. Comparative morphology of spined scales and their phylogenetic significance in the Teleostei. Bull. Mar. Sci. 52, 60–113.
Sagong, W., Kim, C., Choi, S., Jeon, W.-P., Choi, H., 2008. Does the sailfish skin reduce the skin friction like the shark skin? Phys. Fluids 20, 110150.
Shackleton, L.Y., 1987. A comparative study of fossil fish scales from three upwelling regions. South African J. Mar. Sci. 5, 79–84.
Sire, J.-Y., Akimenko, M.-A., 2004. Scale development in fish: a review, with description of sonic hedgehog (shh) expression in the zebrafish (*Danio rerio*). Int. J. Dev. Biol. 48, 233–247.
Song, J., Ortiz, C., Boyce, M.C., 2011. Threat-protection mechanics of an armored fish. J. Mech. Behav. Biomed. Mater. 4, 699–712.
Standen, E.M., Lauder, G.V., 2005. Dorsal and anal fin function in bluegill sunfish *Lepomis macrochirus*: three-dimensional kinematics during propulsion and maneuvering. J. Exp. Biol. 208, 2753–2763.
Sudo, S., Tsuyuki, K., Ito, Y., Ikohagi, T., 2002. A study on the surface shape of fish scales. Jap. Soc. Mech. Eng. 45, 1100–1105.
Suzuki, T., 1971. Some scale patterns of the scad *Decapterus maruadsi* (Temminck et Schlegel), and their variations with body parts. Bull. Jap. Sea Reg. Fish. Res. Lab. 23, 1–19.

Taylor, H.F., 1916. The structure and growth of the scales of the squeteague and the pigfish as indicative of life history. Bull. U.S. Bur. Fish. 34, 285–330.
Tytell, E.D., Alexander, J.K., 2007. Bluegill *Lepomis macrochirus* synchronize pectoral fin motion and opercular pumping. J. Fish Biol. 70, 1268–1279.
Unwin, M.J., Lucas, D.H., 1993. Scale characteristics of wild and hatchery chinook salmon (*Oncorhynchus tshawytscha*) in the Rakaia River. New Zealand, and their use in stock identification. Can. J. Fish. Aquat. Sci. 50, 2475–2484.
Vernerey, F.J., Barthelat, F., 2010. On the mechanics of fishscale structures. Int. J. Solids Struct. 47, 2268–2275.
Wen, L., Weaver, J.C., Lauder, G.V., 2014. Biomimetic shark skin: design, fabrication and hydrodynamic function. J. Exp. Biol. 217, 1656–1666.
Wen, L., Weaver, J.C., Thornycroft, P.J.M., Lauder, G.V., 2015. Hydrodynamic function of biomimetic shark skin: effect of denticle pattern and spacing. Bioinspir. Biomim. 10, 066010 http://dx.doi.org/10.1088/1748-3190/10/6/066010.
Whitehouse, D.J., 1994. Handbook of Surface Metrology. Institute of Physics Publishing, Philadelphia.
Yang, W., Chen, I.H., Mckittrick, J., Meyers, M.A., 2012. Flexible dermal armor in nature. JOM 64, 475–485.
Zhu, D., Ortega, C.F., Motamedi, R., Szewciw, L., Vernerey, F., Barthelat, F., 2012. Structure and mechanical performance of a modern fish scale. Adv. Eng. Mater. 14, 185–194.
Zylberberg, L., Meunier, F.J., Laurin, M., 2010. A microanatomical and histological study of the postcranial dermal skeleton in the Devonian sarcopterygian *Eusthenopteron foordi*. Acta Palaeontol. Pol. 55, 459–470.

3

Scale diversity in bigeye tuna (*Thunnus obesus*): Fat-filled trabecular scales made of cellular bone

Reprinted from:

Wainwright, D.K., Ingersoll, S. & Lauder, G.V. (2017) Scale diversity in bigeye tuna (*Thunnus obesus*): Fat-filled trabecular scales made of cellular bone. *Journal of Morphology*, 279(6), 828-840.

Article and supplement available at https://doi.org/10.1002/jmor.20814

Received: 2 June 2017 | Revised: 19 February 2018 | Accepted: 27 February 2018

DOI: 10.1002/jmor.20814

RESEARCH ARTICLE

WILEY JOURNAL OF morphology

Scale diversity in bigeye tuna (*Thunnus obesus*): Fat-filled trabecular scales made of cellular bone

Dylan K. Wainwright | Sam Ingersoll | George V. Lauder

Museum of Comparative Zoology, Harvard University, Cambridge, Massachusetts

Correspondence
Dylan K. Wainwright, 26 Oxford Street, Museum of Comparative Zoology, Harvard University, Cambridge, MA 02138.
Email: dylanwainwright@fas.harvard.edu

Funding information
ONR MURI, Grant Number: N000141410533; NSF, Grant Number: GRF 2014162421 (to DKW)

Abstract

Tunas of the genus *Thunnus* possess many morphological and physiological adaptations for their high-performance epipelagic ecology. Although *Thunnus* anatomy has been studied, there are no quantitative studies on the structure of their scales. We investigated the scales of bigeye tuna (*Thunnus obesus*) from ten regions of the body using micro computed tomography (μCT)-scanning and histology to quantitatively and qualitatively compare regional scale morphology. We found a diversity of scale sizes and shapes across the body of bigeye tuna and discriminant function analysis on variables derived from μCT-data showed that scales across the body differ quantitatively in shape and size. We also report the discovery of a novel scale type in corselet, tail, and cheek regions. These modified scales are ossified shells supported by internal trabeculae, filled with fat, and possessing an internal blood supply. Histological analysis showed that the outer lamellar layers of these thickened scales are composed of cellular bone, unexpected for a perciform fish in which bone is typically acellular. In the fairing region of the anterior body, these fat-filled scales are stacked in layers up to five scales deep, forming a thickened bony casing. Cheek scales also possess a fat-filled internal trabecular structure, while most posterior body scales are more plate-like and similar to typical teleost scales. While the function of these novel fat-filled scales is unknown, we explore several possible hypotheses for their function.

KEYWORDS
bone, fish, lipid, locomotion, skin

1 | INTRODUCTION

Species in the genus *Thunnus* are large, schooling, regionally endothermic fishes that inhabit the open ocean, where they regularly migrate long distances to utilize seasonal abundances of food in different areas (Block et al., 2011; Carey & Teal, 1966). *Thunnus* spp. also support some of the most economically important global fisheries (Havice & Campling, 2010). The seven species in the genus *Thunnus* have been the subject of study due to their migratory life history habits (Block et al., 2005; Itoh & Tsuji, 2003; Madigan et al., 2014), morphological adaptations to continuous swimming (Bernal, Dickson, Shadwick, & Graham, 2001; Graham, Koehrn, & Dickson, 1983; Kishinouye, 1923; Potthoff, 1975; Westneat, Hoese, Pell, & Wainwright, 1993), and endothermic physiology (Brill, Dewar, & Graham, 1994; Carey & Teal, 1966, 1969; Carey, Teal, Kanwisher, & Lawson, 1971; Graham & Dickson, 2004; Holland, Brill, Chang, Sibert, & Fournier, 1992). Despite this continued biological interest in *Thunnus* spp. and the important role that teleost fish surface structure may play in locomotion by interfacing with the fluid environment (Burdak, 1986; Lauder et al., 2016; Wainwright, Lauder, & Weaver, 2017), there is little detailed information on the structure of skin and scales in any *Thunnus* species.

In teleost fishes, most scales occur as single ossified plates that overlap to create an imbricating pattern on the surface of the body. These bony scales are covered with a layer of epidermis and mucus (Sire & Akimenko, 2004), both of which provide an important immune function for fishes (Shephard, 1994; Xu et al., 2013; Zaccone, Kapoor, Fasulo, & Ainis, 2001). Scales differ substantially among species (Roberts, 1993; Wainwright et al. 2017) and may show considerable variation among regions of the body within the same species (Dapar, Torres, Fabricante, & Demayo, 2012; Wainwright & Lauder, 2016). These differences can include scale shape, the presence of spines or other projections, the presence of ctenii (small interlocking spines that form as separate ossifications), and other traits such as radii (gaps in the ossification of scales) and

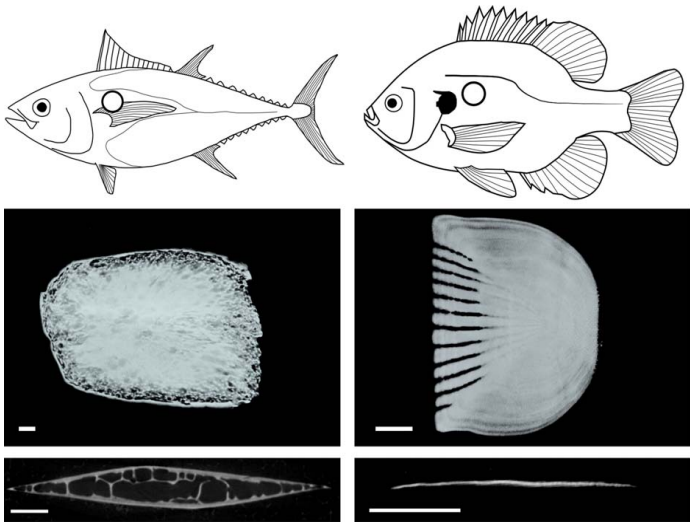

FIGURE 1 Micro-CT scan surface reconstructions and cross-sections for bigeye tuna (*Thunnus obesus*; left panels) and bluegill (*Lepomis macrochirus*; right panels). Images are from scales sampled from the anteriordorsal region of the body (location indicated by a circle on the fish images above). The tuna scale shows a modified morphology without many of the typical teleost scale features present in bluegill, such as radii (gaps in the anterior part of the scale) and circuli (concentric growth lines on the scale's surface). Bigeye tuna scales in this location have a thickened structure with top (lateral) and bottom (medial) ossified plates that join at the edges with trabeculae connecting these plates. The bluegill scale shows a typical teleost scale configuration of a single thin plate of bone without a central cavity (bottom right image). Scales are oriented anterior to the left, and cross-sections are results of cutting each scale dorso-ventrally. Scale bars: 1 mm

circuli (growth rings on the surface of scales). Scales in most teleost species are composed of acellular lamellar bone (lacking osteocytes), which includes plywood-like ossified layers of connective tissue (Sire & Huysseune, 2003; Zylberberg, Bereiter-Hahn, & Sire, 1988). Scales also grow outward from a central focus and thicken as an individual fish grows (Park & Lee, 1988; Schönbörner, Boivin, & Baud, 1979). After initial scale development in teleosts (which happens in post larval stages), scale size increases with fish growth, but scale number does not increase (Taylor, 1916). Scales are replaced if they are lost, and these replacement scales quickly grow to match the size of neighboring scales (Sire & Akimenko, 2004).

Teleost scales are biologically important in a number of ways. Although specific functions have not been conclusively proven, scales likely provide protection against predators and parasites (Browning, Ortiz, & Boyce, 2013; Vernerey & Barthelat, 2014), and serve as calcium stores (Parenti, 1986). Experimental studies on fish scale function have mostly focused on possible armor-like functions and the ability of scales to resist puncture while organized into a flexible protective surface (Bergman, Lajeunesse, & Motta, 2017; Browning et al., 2013; Duro-Royo et al., 2015; Ghosh, Ebrahimi, & Vaziri, 2014; Song, Ortiz, & Boyce, 2011; Vernerey & Barthelat, 2014). However, it has also been hypothesized that scales influence the hydrodynamics of swimming fish surfaces (boundary layer flow in particular) by either directly interacting with the water, or by maintaining an epidermis and mucus layer that interacts with flow next to the fish (Burdak, 1986; Daniel, 1981; Wainwright & Lauder, 2016).

The scales of scombrid fishes are not well studied, although it is well known that that many scombrid genera have a distinctive structure made of enlarged scales, called the corselet, on the anterior half of the body and posterior to the gill opening (see tuna diagram in Figures 1 and 2 [Collette & Nauen, 1983]). Corselet morphology and presence has been qualitatively described for different genera and species in the scombrid group (Collette, 1978; Collette & Nauen, 1983; Kishinouye, 1923) but only general descriptions of corselet scale morphology exist. Collette describes corselet scales as "enlarged" compared to scales posterior on the body and provides descriptions of scales and corselets for each of the different groups in his classification of tunas and mackerels (Collette, 1978). In Kishinouye's (1923) description of *Thunnus* morphology, scales are described as filled with "dentritic lumen," although this observation is not elaborated on. Corselet scales from *Thunuus* spp. are also embedded under a thick epidermis, and while all fishes have an epidermal layer on their scales, tuna epidermis covering the corselet appears to be thicker compared to most other teleost fishes (Kishinouye, 1923). In a paper including a list of teleost species with acellular and cellular bone (although without any figures or other evidence), Kölliker (1857) describes corselet scales from *Thunnus* species as being made of cellular bone—whereas most other perciform fishes have acellular bone. These previous comments on *Thunnus* spp. scales describe interesting features (dentritic lumen, cellular bone) in need of elaboration and further study. Given the multiple adaptations *Thunnus* spp.

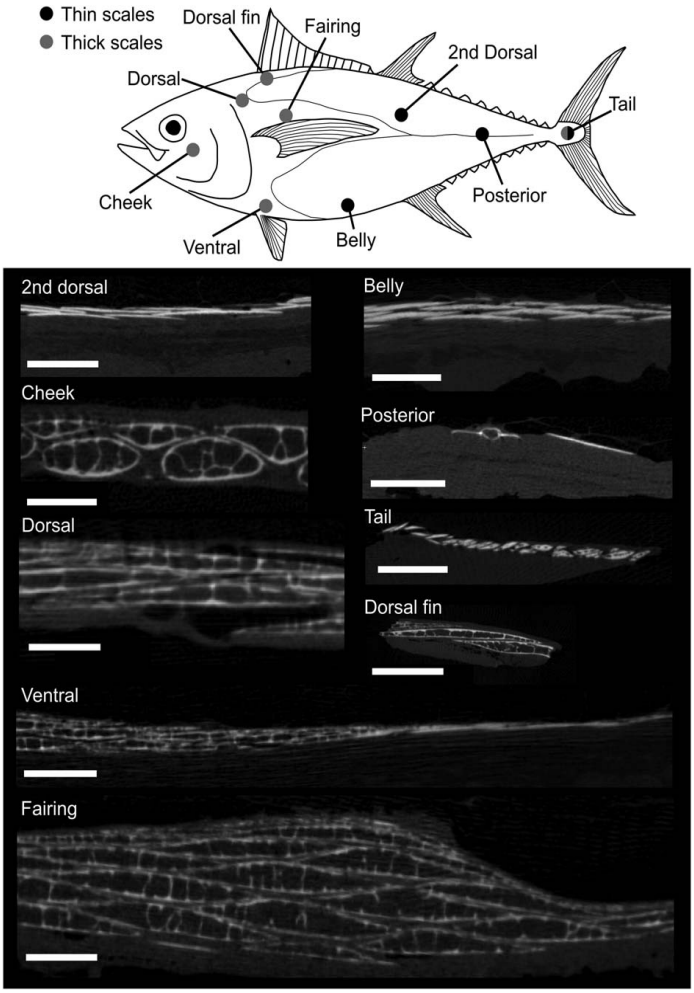

FIGURE 2 Drawing of bigeye tuna indicating the presence of thick or thin scales at different regions sampled (above) and micro-CT scan cross-sections of skin samples from each region (images below: cross-sections are perpendicular to long axis of the scales). The corselet is the region between the thin line that curves around the pectoral fin and the gill opening. Scale bars: 2 mm. The modified thickened scales are visible in the cheek, dorsal, ventral, fairing, dorsal fin, and tail regions, although there are large size differences among these scales. The second dorsal, belly, posterior, tail, and ventral regions show the more typical teleost condition of thin plate-like scales. The fairing region has multiple overlapped thickened scales. Note that the tail and ventral regions show both thick and thin scales

have to their pelagic lifestyle and endothermic physiology (Block & Stevens, 2001), it is reasonable to hypothesize that their scales may show specializations compared to the typical teleost scale pattern. By studying these modifications, we may gain insight into both how the skin of tuna functions and what features of teleost scales and skin are functionally important.

In this study, we investigate the morphology of scales in bigeye tuna (*Thunnus obesus*, Lowe, 1839) at ten regions of the body in five individuals of similar size. We use micro computed tomography (μCT) scanning and histological methods to image and quantify the morphology of scales in this species, and we present both qualitative and quantitative results on the diversity of scales that we find in bigeye tuna. Our results document the presence of considerable scale structure variation across the body and the occurrence of remarkable thickened scales composed of cellular bone with distinctive internal morphological features (trabeculae and lipid inclusions) not known from other teleost species (Figure 1). These results contribute new information about the skin and body surface to the suite of known specializations for pelagic life that characterize *Thunnus* species (Graham & Dickson, 2004).

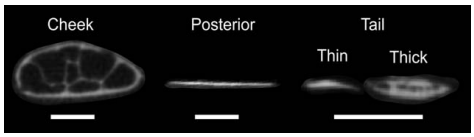

FIGURE 3 CT-scan cross-sections perpendicular to the long axis of the scale from cheek, posterior, and tail regions (regions from Figure 2). Anterior is coming out of the page, and the lateral body surface is towards the top. Scale bars: 500 μm. Cheek scales are thickened with ovoid dorsoventral cross-sections and trabeculae present. Posterior scales are thin and similar to typical teleost scales. Tail scales are small in cross-section (only 200–500 μm in width compared to 1.5–2 mm for cheek and posterior scales) and the tail region has both thick and thin scales. Tail region thickened scales have an open structure in their interiors, although they are thinner than other thickened scales (ex: 200 μm thick compared to 1.5 mm thick for thickened cheek scales). The thin and thick scales from the tail were treated as different regions in our analysis (see methods)

2 | MATERIALS AND METHODS

2.1 | Specimen acquisition and sampling

We obtained five bigeye tuna (*Thunnus obesus*, Lowe, 1839), mean fork length 78.7 cm (1.87 cm standard deviation), from Tropic Fish Hawaii, LLC (Honolulu, Hawaii). Based on their fork length, these fish are approaching maturity (Nootmorn, 2004). Bigeye tuna was chosen as the focus of this study due to the availability of multiple individuals of similar size. Each fish had the internal organs and gills removed at the time of measurement, and all fish were of the same age class (based on their small range of fork lengths). The skin of each fish was sampled at nine different regions of the body (Figure 2) by excising a 4×4 cm region of skin with scales intact from each sampling location. In two individuals, it was difficult to find intact scales on one side of the body due to damage during capture, so some samples were taken from different sides of the body. In total, 45 samples of skin and scales (9 samples from each of 5 individuals) were frozen at -20° C prior to μCT scanning. After sampling we discovered that there are two distinct scale types (termed "thick" and "thin") at the tail region (Figure 3), and we thus treated these different types as distinct regions in our measurements and analyses below, creating a total of ten regional locations instead of the original nine we sampled (see Figure 2 for regions). For brevity, we will refer to these regions throughout the manuscript using the names we give them in Figure 2: cheek, dorsal, fairing, ventral, belly, dorsal fin, 2nd dorsal, posterior, tail thin, and tail thick regions.

The fairing is a ridge on the lateral side of bigeye tuna (and other *Thunnus* species) that starts at the leading-edge origin of the pectoral fin and continues down the length of the corselet down the body. The fairing ridge allows the leading edge of the pectoral fin to sit against it when the pectoral fins are held against the body —this streamlines the body by creating a ridge and pocket that the pectoral fins fit into that smooths the external body surface (Kishinouye, 1923; Walters, 1962).

2.2 | μCT scanning

We used a Bruker Skyscan 1173 μCT-scanner to obtain CT-data for each sample. All samples were scanned using voltages between 45 and 50 kV, currents between 150 and 180 μA, exposures between 900 and 1,100 milliseconds, and with voxel sizes between 13 and 29 μm. Scans were reconstructed into image stacks with NRecon v1.6.9 (Bruker micro CT; Kontich, Belgium) and analyzed with Mimics v16.0.0.235 (Materialise, Leuven, Belgium) to create three-dimensional models and measure morphology. From each sample of tuna skin with multiple overlapping scales, a single scale was isolated digitally in Mimics by segmenting it from adjacent scales to create a surface model for measurements. Because two scale types were recognized in the tail region (thick and thin scales, described below), one scale from each of these types was segmented and analyzed for each tail sample.

For each segmented scale, we measured six variables: scale bone volume, surface area, height, length, thickness, and total scale layer thickness. Scale aspect ratio was also calculated and included as a seventh variable (explanation below). Creating a surface model of each scale allowed for bone volume and surface area to be calculated in Mimics, and it is important to note that these variables only measured the bony elements of scales, not the internal volume or internal surface area. Height was measured as the maximum dorso-ventral height of each scale on the surface model generated in Mimics. Length was quantified as the maximum anteroposterior length. Scale aspect ratio was calculated by dividing the height of each scale by the length of the same scale to give a general metric of scale shape. Scale thickness was measured in cross-sectional views (as seen in Figures 1 and 2) in Mimics software (version 16) and is the largest value of scale thickness along the medial-lateral axis. Finally, total scale layer thickness is the thickness of the entire scale layer, which spans multiple overlapping scales. All μCT data has been uploaded to both the Harvard Dataverse (https://doi.org/10.7910/DVN/LJASQK) and to Open Science Framework (https://osf.io/fuw7k/) and is available for download.

2.3 | Statistical analysis

We used the seven variables that we measured (length, height, thickness, bone volume, surface area, scale aspect ratio, and total scale layer thickness) to study morphological differences between the ten regions we sampled on the body of bigeye tuna. All statistics were performed in R version 3.3.1 (R Development Core Team, 2016). First, we used the package "psych" (Revelle, 2016) to create a correlation matrix using all seven of our variables, in order to determine which variables show similar patterns. We eliminated variables that were highly correlated with each other (details in the results below) to generate a smaller pool of variables, which included bone volume, scale aspect ratio, and total scale layer thickness. To test for morphological differences among body regions, we used a multivariate analysis of variance (MANOVA) using body regions as the independent variable and our three morphological variables as dependent variables. To visually display the results of our MANOVA, we implemented a discriminant function analysis using the "MASS" package in R (Venables & Ripley, 2002) with body

TABLE 1 Dimensions of scales from different body regions. SE refers to one standard error of the mean. Named regions correspond to those in Figure 2

Region	Mean length (mm)	SE length (mm)	Mean height (mm)	SE height (mm)	Mean thickness (mm)	SE thickness (mm)
Cheek	28.21	1.51	4.20	0.15	1.19	0.15
Dorsal	10.52	1.47	8.37	0.76	0.72	0.07
Fairing	14.63	0.63	6.68	0.35	0.93	0.06
Ventral	4.54	0.94	3.36	0.47	0.27	0.07
Dorsal fin	3.89	0.46	2.57	0.36	0.24	0.04
Belly	2.84	0.21	3.31	0.19	0.14	0.02
2nd dorsal	3.46	0.46	3.20	0.2	0.12	0.02
Posterior	2.98	0.13	2.00	0.07	0.15	0.01
Tail thin	4.83	0.65	0.95	0.09	0.09	0.01
Tail thick	3.95	0.53	0.38	0.05	0.14	0.01

region as the independent variable and our three morphological variables as dependent variables. We then performed one-way analysis of variance (ANOVA) tests on bone volume, scale aspect ratio, and total scale layer thickness independently using body region as the independent variable each time. Each ANOVA was followed by a Tukey HSD post-hoc test to test for pairwise differences among regions in a morphological variable (either bone volume, aspect ratio, or total scale layer thickness, depending on the test).

2.4 | Histology

Skin and scales from two bigeye tunas were used for histological analysis to investigate the internal structure of scales and determine scale composition. First, hematoxylin and eosin were used to stain 5-micron-thick sections of paraffin embedded, decalcified (using formic acid) tissue from two regions of bigeye tuna: a region dorsal to the fairing just dorsal to the insertion of the pectoral fin, and a posterior region ventral to the second dorsal fin and dorsal to the anal fin (locations shown in Figure 5). These two regions were chosen for histological analysis to clarify the structure of two distinct scale regions identified by μCT: the thickened scale area on the fairing in comparison to posterior body regions with thinner scales (scale morphology is described in detail below). For one individual, 60 sections (30 from each of the two regions), each 250 microns apart, were examined with hematoxylin and eosin staining. Three sections from a second individual, each 50 microns apart, were fixed and stained with osmium tetroxide (detailed below).

Hematoxylin and eosin stained sections showed what appeared to be fat inside the thickened scales from the anterior part of the body (Figure 5), and to confirm this we fixed and stained a second series of samples from the thickened scale region with osmium tetroxide (Figure 6). Osmium tetroxide fixation preserves lipids in biological tissues (which can otherwise be removed by solvents during standard embedding procedures [Wigglesworth, 1957]), and lipid inclusions then can be positively identified by their black color in subsequent paraffin sections (Figure 6). We first fixed all samples in 4% paraformaldehyde, washed samples with distilled water, decalcified samples (with Fisher Cal-ex CS510-1D), washed them again in water, then stained and fixed lipids in the samples by placing samples in a 0.5% osmium tetroxide bath.

3 | RESULTS

3.1 | μCT-observations

Bigeye tuna have large, thickened scales on parts of their bodies (Table 1, Figures 1 and 2, supporting information Video 1). These thickened scales (Figure 4) are markedly different from the typical flattened

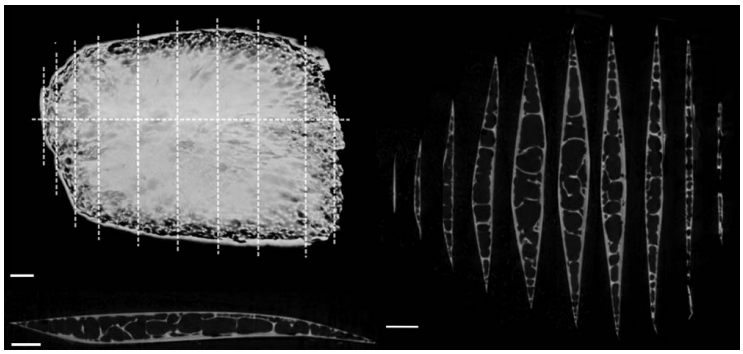

FIGURE 4 CT-scan surface rendering and cross-sections of a scan of an isolated scale from the dorsal region (Figure 2). Anterior is to the left and dorsal is at the top of both the top-left image and right-side cross-sections. Anterior to the left and dorsal is into the page for the bottom left cross-section. The surface rendering in the top left shows weaker ossification at the edges of the scale, especially at the posterior margin. To the right, 10 dorso-ventral cross-sections are shown of this single scale from the dorsal region of the bigeye tuna. The lines on the surface rendering show where cross-sections were taken. A single anteroposterior cross-section is shown in the bottom left—there is asymmetry with the anterior side being thicker than the posterior. The cross-sections show the trabeculae present in the internal part of the scale. Scale bars: 1 mm

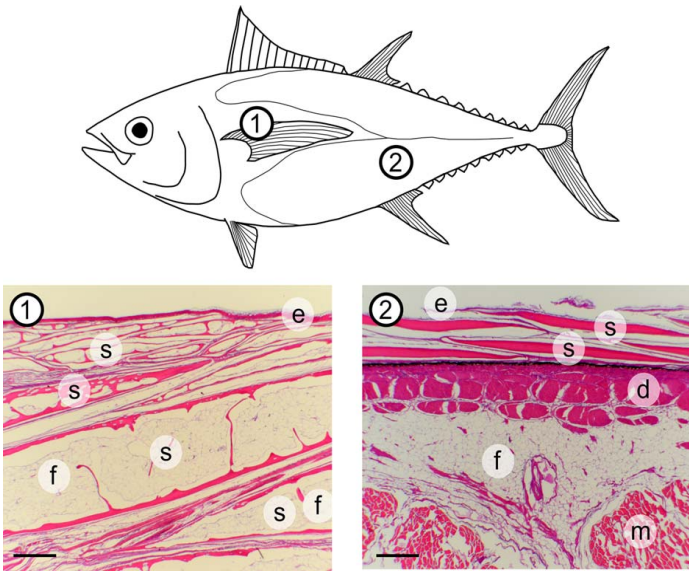

FIGURE 5 Histological sections from two regions of the body of a bigeye tuna, stained with hematoxylin and eosin. Region 1 is near the fairing region (Figure 2) and shows thickened, modified scales, while region 2 is ventral to the 2nd dorsal area (Figure 2) and shows more typical teleost scale morphology from further posterior on the body. There are many scales present in region 1, and we label four of them. Labels: e, epidermis; s, scale; d, dermis; m, muscle; f, fat. Scale bars: 500 μm

scales of most other teleosts (including bigeye tuna scales from other regions of the body) which are composed of bony laminae with a solid internal structure (Figure 1). The thickened scales of *T. obesus* are present mostly posterior to the gill opening around the pectoral fin, and make up the corselet (Figure 2) while other parts of the body have smaller, thinner scales of lamellar bone (Table 1, Figure 2; Collette & Nauen, 1983; Kishinouye, 1923). The thickened scales of bigeye tuna are 0.7–1.2 mm thick, which is thicker than both typical teleost scales (0.06–0.2 mm thick [Bergman et al. 2017; Wainwright & Lauder, 2016]) and scales on the posterior part of the body of bigeye tuna (0.09–0.27 mm thick, Table 1). Some parts on the head of bigeye tuna are scale-less (such as the dorsal side of the head) but the body of the tuna (posterior to the opercle) is covered in scales.

In bigeye tuna, thickened scales have an ossified exterior layer of lamellar bone that forms the exterior and interior sides of the scale and surrounds an internal cavity made of bony trabeculae surrounded by fat cells (Figures 1 and 4: described in more detail below). Furthermore, these scales do not have the typical growth lines (circuli) or gaps in the ossification of their anterior fields (radii) apparent in other teleost scales (visible in the bluegill scale shown in Figure 1). The thickened scales of the corselet have spindle-shape dorsoventral cross-sections, trabeculae crossing their interiors, an asymmetrical anteroposterior cross-section, and weak ossification at their edges, especially at the posterior edge (Figure 4). Thickened scales also occur on the cheek (exterior to the adductor mandibulae muscles) and tail (exterior to the hypural plate) regions of bigeye tuna (Figure 2). Scales at the cheek are elongate in anterior-posterior axis of the body and are thicker (mean thickness: 1.2 mm, Table 1) and larger (mean length: 28.2 mm, Table 1) than scales elsewhere on the body. At the tail region, however, scales of two types are present: thickened scales with an internal cavity, and thin, plate-like scales (Figure 3). Both of these scale types in this region are relatively small (mean length: 4.4 mm, Table 1), while also being elongated in a direction parallel to the anterior-posterior axis of the body. Overall, the morphology of thickened scales across the body is qualitatively diverse in both size and shape (Figure 2, Table 1). Transitions between thick and thin scales can be seen in images from the sampling regions labeled ventral and tail (Figure 3).

3.2 | μCT-measurements

A correlation matrix was calculated for the seven measured variables (bone volume, surface area, height, length, scale thickness, total scale layer thickness, aspect ratio) to determine the degree of inter-correlation among all pairs of variables. The size-related variables (bone volume, surface area, height, length, thickness) were all highly correlated with one another ($R = 0.69–0.95$; excluding height: $R = 0.91–0.95$). We elected to use scale bone volume to represent these five variables because we believe it best represents size of a scale and energy invested for growth. Total scale layer thickness and scale aspect ratio were not as highly correlated to bone volume as other variables ($r = .77$ for total scale layer thickness; $r = -.29$ for aspect ratio), so we elected to include these two variables along with bone volume in our multivariate analyses.

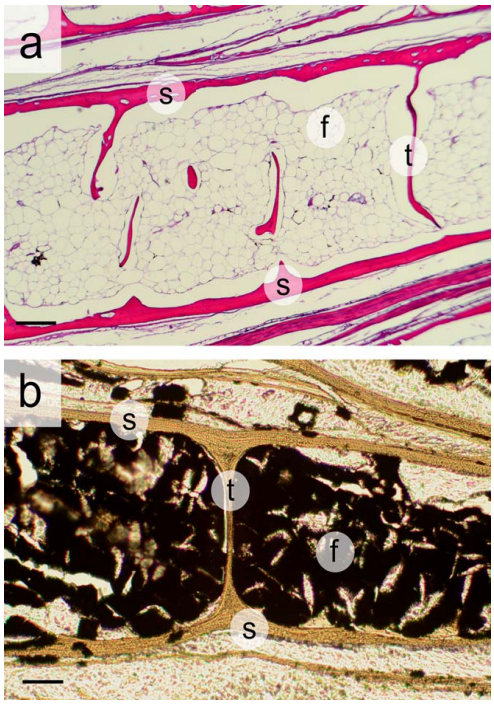

FIGURE 6 Histological sections of bigeye tuna scales. (a) Hematoxylin and eosin stained section showing details of fat deposition inside a thickened scale. Globular fat cells are visible inside the scale. The top (lateral surface) and bottom (medial surface) of the scale are both labeled "s," and portions of the internal bony trabeculae are visible "t." (b) Osmium tetroxide stained section of an individual scale to confirm the presence of fat (stained black) inside the scale. The top and bottom of the scale are labeled "s," and an entire bony trabeculae labeled "t." Labels: s, outer bone of scales; f, fat; t, trabeculae. Scale bars: 200 μm in (a) and 100 μm in (b)

We used a MANOVA with bone volume, total scale layer thickness, and scale aspect ratio as our dependent variables, and the region of the body as the independent variable to test for the effect of body position on scale morphology. Results from the MANOVA indicate that there are significant differences in scale morphology among different body regions (Wilks lambda, degrees of freedom = 9, Wilks approximation = 0.00309, $F = 25.7$, $p < .0001$) (MANOVA results are displayed with a discriminant function analysis, explained below; Figure 8). We then used multiple ANOVAs to test which of the three variables (bone volume, total scale layer thickness, and aspect ratio) differ among scales from different regions of the body (Figure 9). We found significant differences among body regions in bone volume (degrees of freedom = 9, F value = 25.3, $p < .0001$), total scale layer thickness (degrees of freedom = 9, F value = 30.4, $p < .0001$), and scale aspect ratio (degrees of freedom = 9, F value = 55.8, $p < .0001$).

In addition, we display the results of the MANOVA with a discriminant function analysis in Figure 8, which creates multivariate, orthogonal axes that best separate the given groups, in this case the ten sampled regions. Scale aspect ratio loads heavily on the first linear discriminant axis, which is responsible for 55.6% of the variation in the data set. Both bone volume and total scale layer thickness load heavily on the second linear discriminant axis, which is responsible for 38.0% of the variation in the data. Scales from the fairing, cheek, and dorsal regions have large bone volumes and occur in the thickest layers compared to other regions. Scales from the cheek, tail thin, and tail thick regions all have the highest aspect ratios (elongate in the anteroposterior axis), however tail thin and thick regions both have scales with small volumes that occur in thin layers in the skin. Scales from the belly and 2nd dorsal regions have the smallest aspect ratios (taller in the dorsoventral axis).

3.3 | Histological results

The hematoxylin and eosin stained sections show the presence of adipocytes inside the thickened scales as transparent globular structures (Figure 6a). The presence of fat inside the thickened scales was confirmed with an osmium tetroxide fixation and stain of lipids (Figure 6b). A layer of fat cells is also present beneath the dermis in body regions with thin scales (Figure 5). The presence of subdermal fat cannot be confirmed beneath the corselet because our sections are not deep enough.

Histological sections also reveal both arterioles and venules among the fat cells (Figure 7), which might serve to deposit or mobilize lipids in the scale interior. These arterioles and venules are consistent with the size and morphology of the same structures in other vertebrate taxa (Bloom & Fawcett, 1975; Patt & Patt, 1969). Also, lacunae (30–50 μm in diameter) are present in the external bone of the thickened scales (Figure 7e,f), and likely correspond to locations where the circulatory system penetrates the bony scale exterior. Within the lamellar bone covering each thickened scale (as well as the trabeculae: Supplementary Figure 1), smaller lacunae (about 10 μm in diameter) contain osteocytes and reflect the presence of bone (Figure 7e,f). These small lacunae and osteocytes are consistent with those seen in other vertebrate taxa (Atkins et al., 2014; Bloom & Fawcett, 1975; Patt & Patt, 1969). Thin scales occur on body regions other than the corselet (Figure 2) and are plate-like with a lamellar structure. These scales also have small lacunae containing osteocytes at scale margins, indicating the presence of cellular bone (Figure 7g,h).

4 | DISCUSSION

Analysis of scale morphology in bigeye tuna shows that this species has modified scales compared to typical flattened ctenoid and cycloid scales in many other teleosts (Figure 1, supporting information Video 1). These thickened scales are composed of bony outer shells filled with fat and braced by trabeculae. In addition, the bone of both thick and thin scales is made of cellular bone. Arterioles and venules are also visible among the fat cells inside the thick scales. These thickened, fat-filled scales occur on the cheek, at the base of the caudal fin, and as part of the corselet (posterior to the gill opening).

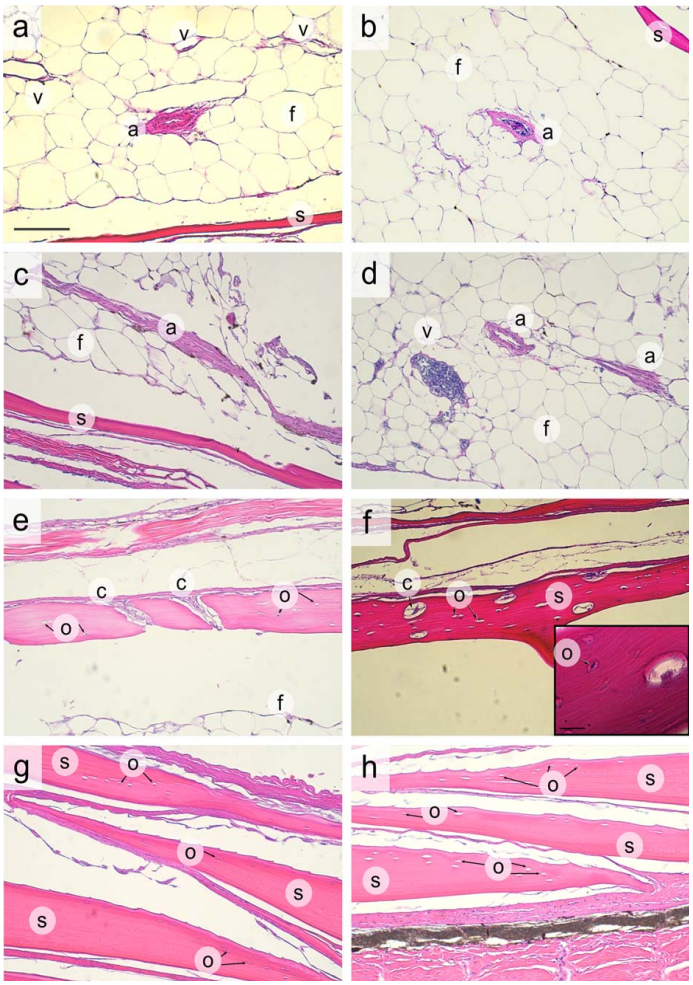

FIGURE 7 Histological sections stained with hematoxylin and eosin showing details of internal structure in the thickened (a–f) and thin (g, h) scales of bigeye tuna. (a) The fat-filled region of a single fairing scale, with an arteriole "a" and three venules "v" visible inside the scale. (b) An arteriole showing the lumen and blood cells. (c) A transverse section of the wall of an arteriole inside a scale. (d) Two cross-sections of arterioles and a venule showing blood in its interior. (e) The cellular bone wall of a thickened scale, with larger lacunae carrying circulatory elements labeled with "c" and smaller lacunae containing osteocytes labeled with "o." (f) Osteoctyes and larger lacunae in the lamellar bone of a thickened scale. (g) Thin scales with lacunae containing osteocytes (labeled "o"). (h) More thin scales showing cellular bone. Labels: s: scale wall; a: arteriole in adipose tissue; f: fat; v: venules; c: circulatory element in lacunae; o: osteocyte in lacunae. Scale bar: 100 μm (for all panels, in (a) only). Scale bar for (f) inset: 15 μm

On much of the posterior regions of the body, bigeye tuna have thin plate-like scales that are superficially similar to the scales of most perciform fishes (Parenti, 1986; Sire & Akimenko, 2004), and these scales are also composed of cellular bone at their margins. Bigeye tuna have remarkably diverse scales among the ten sampled regions of their body. Skin samples from different regions differ with respect to their scale volume, total scale layer thickness, and scale aspect ratio, indicating that they vary in size, shape, and the extent of overlap between scales (Figure 2). In general, larger scales are located in more anterior body regions, while smaller scales are found on the posterior half of bigeye tuna.

The thickened, fat-filled scales of the corselet and cheek are remarkable in their morphology, but no data on scale function in tuna are available. Hypotheses of the function of these modified thickened scales and of variation in scale morphology across the body are thus necessarily somewhat speculative. Despite this, if we restrict ourselves to first principles of the composition and structure of the modified scales, we can confidently state a few functional implications using hypothetical

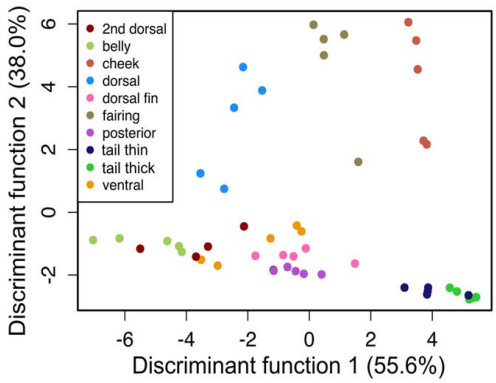

FIGURE 8 Discriminant function analysis using region of the body as the dependent variable and volume, skin thickness, and scale aspect ratio as independent variables. Scale aspect ratio loads most heavily on the first discriminant function, which is responsible for 55.6% of the variation in the data. Both volume and total scale layer thickness load heavily on the second discriminant function, which is responsible for 38.0% of the variation. Color denotes different body regions from which scales were sampled (Figure 2)

comparisons. First, thickened scales will protect the body surface from damage more so than smaller flattened scales or no scales. Second, fat-filled scales will increase buoyancy compared to scales of the same size but made entirely of bone. Third, fat-filled scales will provide better thermal insulation by decreasing conductance across the skin compared to similar-sized bone scales, or no scales. Subdermal fat (Figure 2) would provide additional thermal insulation—another endothermic fish, the opah, is described as having an exceptionally thick subdermal layer of fat around their body (Wegner, Snodgrass, Dewar, & Hyde, 2015). Although we can be confident in the action of these physical mechanisms, we do not know if these mechanisms have large enough effects on bigeye tuna to be functionally important. Further studies including experimental measurements of scale thermal and material properties, and studies comparing scale morphology across taxa in resolved scombrid trees (Miya et al., 2013; Santini, Carnevale, & Sorenson, 2013) would inform potential functions of thickened scales in protection, buoyancy, and thermal insulation. Although *Thunnus* spp. have the largest and most well-developed corselets (where we see the modified scales), non-endothermic scombrid genera such as *Sarda* are also described as having corselets (Collette & Nauen, 1983; Kishinouye, 1923), although there are no publications discussing details of their scale morphology.

Previous studies have suggested that corselets reduce drag in tuna swimming by tripping the boundary layer from laminar to turbulent to delay boundary layer separation (Blake, 2004; Fierstine & Walters, 1968; Walters, 1962; Webb, 1975). Although no study has experimentally examined flow over this region during swimming, we believe this is an unlikely function of the corselet because both the enlarged scales of the corselet and the smaller scales posterior to the corselet are coated in both epidermis and mucus. Covering scales with epidermis and mucus has an effect of smoothing the topography of the scales in fishes (Wainwright & Lauder, in press; Wainwright et al., 2017), which would make it difficult to trip the boundary layer from laminar to turbulent. Furthermore, the end of the corselet (Figure 2: fairing) does not create the type of roughness element (a sharp drop or bump) that is required to trip a boundary layer from laminar to turbulent. To support this, the cross-section of skin from the ventral region (Figure 2) illustrates the gradient of scale morphology at the edge of the corselet – this smooth transition is unlikely to trip the boundary layer.

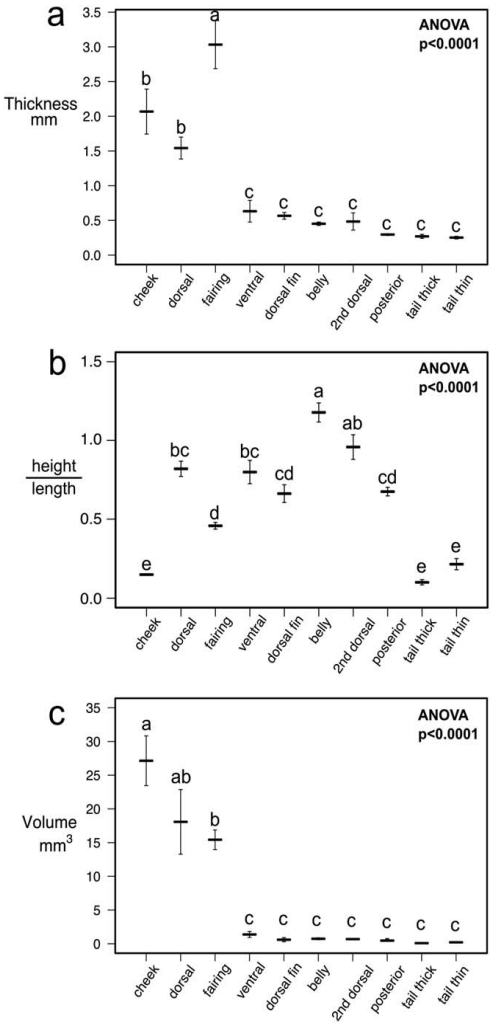

FIGURE 9 (a) Thickness of the scale layer, (b) scale aspect ratio, and (c) scale bony tissue volume compared across different body regions of bigeye tuna. Dark bars are means and error bars are +/− 1 standard error for one scale sampled per region for five bigeye tuna. ANOVA results are shown on each graph and lowercase letter labels indicate significant groupings using a Tukey HSD test. If a letter is shared between regions, there is no significant difference between them in the measured variable

The thickened scales of the corselet also give form to the fairing, which is a ridge that is dorsal to the pectoral fin and runs posteriorly down the body to the edge of the corselet—it allows the pectoral fin to be adducted against the body with its thickened leading edge against the ridge of the fairing, streamlining the contours of the body and pectoral fin (Kishinouye, 1923; Walters, 1962). This fairing is constructed using the thickened scales of the corselet (fairing region, Figure 2) where more scales are layered on top one another, and where scales are thinner in the depression for the pectoral fin, ventral to the fairing ridge. In this way, the corselet scales may contribute indirectly to drag reduction by providing streamlining for adducted pectoral fins. However, scales are not required for creating fairing-like structures, as similar structures are seen near the pectoral fins of beaked whales (Dalebout et al., 2003; Mead, Walker, & Houck, 1982). Therefore, it is difficult to assign a purely drag reductive role to the modified scales we have described, because as beaked whale morphology shows, construction of a fairing does not require scales.

Thunnus spp. have often been described as having a specialized undulatory swimming mode, called thunniform swimming (Breder, 1926; Webb, 1975) which is characterized by low amplitude bending in the head and body and higher amplitude bending in the peduncle and tail. Although thunniform swimming is often cited as a specialized case of swimming kinematics where lateral head amplitude (yaw) during swimming is exceptionally low, one study shows that the lateral head amplitude of thunniform swimmers is no different than carangiform swimmers (Donley & Dickson, 2000). Similarly, another study comparing midline kinematics of tunas to other species shows little difference in the ratio of head-to-tail amplitude in lateral bending between tunas and other fishes (Lauder & Tytell, 2006). Although one may propose that the thickened scale layer of the corselet creates higher stiffness in the anterior body reflective of thunniform swimming, kinematic data do not show any reduced lateral movement in the anterior body for swimming tuna, and thus do not support either the idea that thickened scales contribute to higher body stiffness at the head, or that thunniform swimming has smaller head oscillation amplitude than other swimming categories.

The function of the cellular bone and circulatory system elements (Figure 7) within thickened scales is unknown, but both anatomical features suggest a higher metabolic rate in these scales (compared to scales without either feature) and that calcium and lipids may be mobilized for metabolic needs. Although a circulatory system is known to be present on the surface of fish skin and on the surface of scales in teleost fishes (Farrell, Eliason, Clark, & Steinhausen, 2014; Rummer, Wang, Steffensen, & Randall, 2014), the circulatory elements identified inside bigeye tuna thick scales are, to our knowledge, unique among teleost fishes. Circulatory control of deposition and mobilization inside thickened scales would allow for control of lipid use with growth or during migratory periods with limited feeding where additional energy may be needed (as in salmonids [e.g., Penney & Moffitt, 2015]). Fat deposition in the scales and below the skin in tuna could also function as a reservoir for gamete production. Analyzing the fat content of thick scales in bigeye tunas under stress, starvation, or spawning conditions could determine if interior lipids are mobilized to meet metabolic needs, and determining what lipids are being stored would inform potential metabolic or buoyancy-related functions (Phleger, 1998).

The presence of cellular bone in both thickened and thin bigeye tuna scales warrants further investigation, as current comparative data suggest that "basal" teleosts and teleosts with ganoid scales have cellular bone in their scales, while most perciform fishes possess acellular bone (Meunier, 1981; Meunier & Brito, 2004; Parenti, 1986). Previous work indicates that tunas have cellular bone (our histological work confirms this for bigeye tuna), while the closely related mackerels (*Scomber* spp.) have acellular bone (Kölliker, 1857; Meunier, 2011). Most teleosts have acellular bone not only in their scales, but also in their body skeleton, yet we know little about the functional implications of having cellular versus acellular bone in fishes (Cohen et al., 2012; Moss, 1961; Shahar & Dean, 2013). It has long been thought that acellular bone is a derived condition in fishes, with euteleosts having a skeleton of acellular bone compared to cellular bone in more basal taxa (Meunier, 2011; Parenti, 1986). However it has also been shown that many euteleosts have cellular bone in parts of their skeleton (Hughes, Bassett, & Moffat, 1994) and that there are many transitions from acellular to cellular bone throughout teleosts (Kölliker, 1857; Kranenbarg, van Cleynenbreugel, Schipper, & van Leeuwen, 2005; Meunier & Huysseune, 1992; Moss, 1961, 1965; Sire, Huysseune, & Meunier, 1990).

In fishes, the function of acellular versus cellular bone has not been determined, although some hypotheses have been tested and found to have little support. For example, studies have found that acellular bone has similar material properties to cellular fish bone (Cohen et al., 2012; Dean & Shahar, 2012; Horton & Summers, 2009), acellular bone can remodel itself despite lacking enclosed cells (Atkins et al., 2014; Kranenbarg, et al., 2005), and cellular bone does not appear to be more prevalent in freshwater fish species, which may need to draw on calcium stores more often than saltwater fishes (Moss, 1965). Perhaps the presence of cellular bone in the large scales of bigeye tuna assists in rapid scale growth or remodeling, as well as rapid mobilization and deposition of calcium. Large, pelagic, fast-growing fishes may have higher needs for calcium and bone remodeling, especially during long migrations, necessitating cellular bony scales. One study has demonstrated bone resorption in fin spines of Atlantic bluefin tuna (*Thunnus thynnus*) (Santamaria et al., 2015) and more work on different bones of other scombrid species could determine if tunas have specializations for increased bone remodeling or resorption, compared to *Scomber* spp. (close relatives with acellular bone). Curiously, the osteocytes in the bone of the thin scales of *Thunnus* appear to be concentrated near scale margins, where remodeling and growth would also be concentrated (Figure 7g,h). However, there is no apparent pattern to osteocyte distribution in the thickened scales (Figures 6 and 7). Leatherback turtle (*Dermochelys coriacea*, Vandelli 1761) bones have a similarly modified growth pattern, perhaps due to high growth rates, large adult sizes, and endothermy (Rhodin, 1985) and the modified bone structure seen in bigeye tuna could be a reflection of some of these characteristics as well.

We have discovered considerable diversity in simple measures of size and shape among scales from different regions of the body of bigeye tuna and a remarkable trabecular structure in thickened anterior

scales. Generally, larger scales occur on the cheek and corselet of bigeye tuna, while smaller scales occur posteriorly on the body. The larger scales of the cheek and corselet, along with some smaller scales at the base of the tail, have a distinct bony shell made of cellular bone and an internal structure of fat cells, trabeculae, and circulatory elements. These scales represent an interesting departure from normal teleost scales which consist of flat sheets of acellular bone, and the function of these modified scales represents an intriguing area for future research.

ACKNOWLEDGMENTS

We would like to acknowledge William Goldsmith for his expertise on tunas, Cathy MacGillivray and the Harvard Department of Stem Cell and Regenerative Biology's Histology-Immunohistochemistry Core for aid with histology, Toby Arakawa for his assistance in obtaining specimens, Ryan Hulett for his microscopy expertise, Dan Madigan for proofreading, and the comments of two anonymous reviewers. This work was supported by ONR MURI Grant N000141410533 monitored by Dr. Bob Brizzolara and NSF GRF 2014162421 awarded to DKW.

AUTHOR CONTRIBUTIONS

DKW and GVL conceived the research. DKW and SI led data collection and DKW led the writing of the manuscript. All authors contributed to the manuscript and gave approval for publication.

ORCID

Dylan K. Wainwright http://orcid.org/0000-0003-4964-5048
George V. Lauder http://orcid.org/0000-0003-0731-286X

REFERENCES

Atkins, A., Dean, M. N., Habegger, M. L., Motta, P. J., Ofer, L., Repp, F., … Shahar, R. (2014). Remodeling in bone without osteocytes: Billfish challenge bone structure–function paradigms. *Proceedings of the National Academy of Sciences of the United States of America*, *111*, 16047–16052.

Bergman, J. N., Lajeunesse, M. J., & Motta, P. J. (2017). Teeth penetration force of the tiger shark *Galeocerdo cuvier* and sandbar shark *Carcharhinus plumbeus*. *Journal of Fish Biology*, *91*, 460–472.

Bernal, D., Dickson, K. A., Shadwick, R. E., & Graham, J. B. (2001). Review: Analysis of the evolutionary convergence for high performance swimming in lamnid sharks and tunas. *Comparative Biochemistry and Physiology - A Molecular and Integrative Physiology*, *129*, 695–726.

Blake, R. W. (2004). Fish functional design and swimming performance. *Journal of Fish Biology*, *65*(5), 1193–1222.

Block, B. A., Jonsen, I. D., Jorgensen, S. J., Winship, A. J., Shaffer, S. A., Bograd, S. J., … Costa, D. P. (2011). Tracking apex marine predator movements in a dynamic ocean. *Nature*, *475*, 86–90.

Block, B. A., & Stevens, G. (2001). *Fish physiology: Tuna: Physiology, ecology and evolution*. *Volume 19*. (W. Hoar, D. Randall, & A. Farrell, Eds.). (1st ed.). New York, NY: Academic Press.

Block, B. A., Teo, S. L. H., Walli, A., Boustany, A., Stokesbury, M. J. W., Farwell, C. J., … Williams, T. D. (2005). Electronic tagging and population structure of Atlantic bluefin tuna. *Nature*, *434*, 1121–1127.

Bloom, W., & Fawcett, D. W. (1975). *A textbook of histology* (10th ed.). Philadelphia, PA: W. B. Saunders Company.

Breder, C. M. (1926). The locomotion of fishes. *Zoologica*, *4*, 159–297.

Brill, R. W., Dewar, H., & Graham, J. B. (1994). Basic concepts relevant to heat transfer in fishes, and their use in measuring the physiological thermoregulatory abilities of tunas. *Environmental Biology of Fishes*, *40*, 109–124.

Browning, A., Ortiz, C., & Boyce, M. C. (2013). Mechanics of composite elasmoid fish scale assemblies and their bioinspired analogues. *Journal of the Mechanical Behavior of Biomedical Materials*, *19*, 75–86.

Burdak, V. D. (1986). Morphologie fonctionnelle du tegument ecailleux des poissons. *Cybium*, *10*, 1–128.

Carey, F. G., & Teal, J. M. (1966). Heat conservation in tuna fish muscle*. *Proceedings of the National Academy of Sciences of the United States of America*, *56*(5), 1464–1469.

Carey, F. G., & Teal, J. M. (1969). Regulation of body temperature by the bluefin tuna*. *Comparative Biochemistry and Physiology Part Physiology*, *28*(1), 205–213.

Carey, F. G., Teal, J. M., Kanwisher, J. W., & Lawson, K. D. (1971). Warm-bodied fish. *American Zoologist*, *11*, 137–145.

Cohen, L., Dean, M., Shipov, A., Atkins, A., Monsonego-Ornan, E., & Shahar, R. (2012). Comparison of structural, architectural and mechanical aspects of cellular and acellular bone in two teleost fish. *Journal of Experimental Biology*, *215*(11), 1983–1993.

Collette, B. B. (1978). II. Adaptations and Systematics of the mackerels and tunas. In G. D. Sharp & A. E. Dizon (Eds.), *The physiological ecology of tunas* (pp. 7–39). New York, NY: Academic Press.

Collette, B. B., & Nauen, C. E. (1983). FAO species catalogue. *Vol. 2. Scombrids of the world. An annotated and illustrated catalogue of tunas, mackerels, bonitos and related species known to date*. Rome.

Dalebout, M. L., Baker, C. S., Anderson, R. C., Best, P. B., Cockcroft, V. G., Hinsz, H. L., … Pitman, R. L. (2003). Appearance, distribution, and genetic distinctiveness of longman's beaked whale, *Indopacetus pacificus*. *Marine Mammal Science*, *19*(3), 421–461.

Daniel, T. L. (1981). Fish mucus: In situ measurements of polymer drag reduction. *Biological Bulletin*, *160*(3), 376–382.

Dapar, M. L. G., Torres, M. A. J., Fabricante, P. K., & Demayo, C. G. (2012). Scale morphology of the Indian goatfish, *Parapeneus indicus* (Shaw, 1803) (Perciformes: Mullidae). *Advances in Environmental Biology*, *6*, 1426–1432.

Dean, M. N., & Shahar, R. (2012). The structure-mechanics relationship and the response to load of the acellular bone of neoteleost fish: A review. *Journal of Applied Ichthyology*, *28*(3), 320–329.

Donley, J. M., & Dickson, K. A. (2000). Swimming kinematics of juvenile kawakawa tuna (*Euthynnus affinis*) and chub mackerel (*Scomber japonicus*). *The Journal of Experimental Biology*, *203*, 3103–3116.

Duro-Royo, J., Zolotovsky, K., Mogas-Soldevila, L., Varshney, S., Oxman, N., Boyce, M. C., & Ortiz, C. (2015). MetaMesh: A hierarchical computational model for design and fabrication of biomimetic armored surfaces. *Computer Aided Design*, *60*, 14–27.

Farrell, A. P., Eliason, E. J., Clark, T. D., & Steinhausen, M. F. (2014). Oxygen removal from water versus arterial oxygen delivery: Calibrating the Fick equation in Pacific salmon. *Journal of Comparative Physiology B: Biochemical, Systemic, and Environmental Physiology*, *184*, 855–864.

Fierstine, H., & Walters, V. (1968). Studies in locomotion and anatomy of scombroid fishes. *Memoirs of the Southern California Academy of Sciences*, *6*, 1–31.

zebrafish (*Danio rerio*). *The International Journal of Developmental Biology*, *48*, 233–247.

Sire, J.-Y., & Huysseune, A. (2003). Formation of dermal skeletal and dental tissues in fish: A comparative and evolutionary approach. *Biological Reviews of the Cambridge Philosophical Society*, *78*, 219–249.

Sire, J.-Y., Huysseune, A., & Meunier, F. J. (1990). Osteoclasts in teleost fish: Light-and electron-microscopical observations. *Cell and Tissue Research*, *260*, 85–94.

Song, J., Ortiz, C., & Boyce, M. C. (2011). Threat-protection mechanics of an armored fish. *Journal of the Mechanical Behavior of Biomedical Materials*, *4*, 699–712.

Taylor, H. F. (1916). The structure and growth of the scales of the squeteague and the pigfish as indicative of life history. *Bulletin of the Bureau of Fisheries*, *34*, 285–330.

Venables, W. N., & Ripley, B. D. (2002). *Modern applied statistics with S* (4th ed.). New York, NY: Springer.

Vernerey, F. J., & Barthelat, F. (2014). Skin and scales of teleost fish: Simple structure but high performance and multiple functions. *Journal of the Mechanics and Physics of Solids*, *68*, 66–76.

Wainwright, D. K., & Lauder, G. V. (2016). Three-dimensional analysis of scale morphology in bluegill sunfish, *Lepomis macrochirus*. *Zoology*, *119*, 182–195.

Wainwright, D. K., & Lauder, G. V. (2018). Mucus matters: The slippery and complex surfaces of fish. In S. N. Gorb & E. Gorb (Eds.), *Functional surfaces in biology - From the Micro- to Nanoscale*. Springer Berlin Heidelberg.

Wainwright, D. K., Lauder, G. V., & Weaver, J. C. (2017). Imaging biological surface topography in situ and in vivo. *Methods in Ecology and Evolution*, *8*, 1626–1638.

Walters, V. (1962). Body form and swimming performance in Scombroid fishes. *American Zoologist*, *2*(2), 143–149.

Webb, P. W. (1975). Hydrodynamics and energetics of fish propulsion. *Bulletin of the Fisheries Research Board of Canada*, *190*, 159.

Wegner, N. C., Snodgrass, O. E., Dewar, H., & Hyde, J. R. (2015). Whole-body endothermy in a mesopelagic fish, the opah, *Lampris guttatus*. *Science (New York, N.Y.)*, *348*(6236), 786–789.

Westneat, M. W., Hoese, W., Pell, C. A., & Wainwright, S. A. (1993). The horizontal septum: Mechanisms of force transfer in locomotion of Scombrid fishes (Scombridae, Perciformes). *Journal of Morphology*, *217*, 183–204.

Wigglesworth, V. B. (1957). The use of osmium in the fixation and staining of tissues. *Proceedings of the Royal Society of London. Series B, Biological Sciences*, *147*(927), 185–199.

Xu, Z., Parra, D., Gomez, D., Salinas, I., Zhang, Y.-A., von Gersdorff Jørgensen, L., . . . Sunyer, J. O. (2013). Teleost skin, an ancient mucosal surface that elicits gut-like immune responses. *Proceedings of the National Academy of Sciences of the United States of America*, *110*, 13097–13102.

Zaccone, G., Kapoor, B. G., Fasulo, S., & Ainis, L. (2001). Structural, histochemical and functional aspects of the epidermis of fishes. *Advances in Marine Biology*, *40*, 253–348.

Zylberberg, L., Bereiter-Hahn, J., & Sire, J. Y. (1988). Cytoskeletal organization and collagen orientation in the fish scales. *Cell and Tissue Research*, *253*, 597–607.

SUPPORTING INFORMATION

Additional Supporting Information may be found online in the supporting information tab for this article.

How to cite this article: Wainwright DK, Ingersoll S, Lauder GV. Scale diversity in bigeye tuna (*Thunnus obesus*): Fat-filled trabecular scales made of cellular bone. *Journal of Morphology*. 2018;00:1–13. https://doi.org/10.1002/jmor.20814

Ghosh, R., Ebrahimi, H., & Vaziri, A. (2014). Contact kinematics of biomimetic scales. *Applied Physics Letters*, *105*, 233701-1–233701–5.

Graham, J. B., & Dickson, K. A. (2004). Tuna comparative physiology. *The Journal of Experimental Biology*, *207*(Pt 23), 4015–4024.

Graham, J. B., Koehrn, F. J., & Dickson, K. A. (1983). Distribution and relative proportions of red muscle in scombrid fishes: Consequences of body size and relationships to locomotion and endothermy. *Canadian Journal of Zoology*, *61*, 2087–2096.

Havice, E., & Campling, L. (2010). Shifting tides in the Western and Central Pacific Ocean tuna fishery: The political economy of regulation and industry responses. *Global Environmental Politics*, *10*, 89–114.

Holland, K. N., Brill, R. W., Chang, K. C., Sibert, R., J. R., & Fournier, D. A. (1992). Physiological and behavioural thermoregulation in the bigeye tuna (*Thunnus obesus*). *Nature*, *358*, 410–412.

Horton, J. M., & Summers, A. P. (2009). The material properties of acellular bone in a teleost fish. *The Journal of Experimental Biology*, *212*(Pt 9), 1413–1420.

Hughes, D. R., Bassett, J. R., & Moffat, L. A. (1994). Histological identification of osteocytes in the allegedly acellular bone of the sea breams *Acanthopagrus australis*, *Pagrus auratus* and *Rhabdosargus sarba* (Sparidae, Perciformes, Teleostei). *Anatomy and Embryology*, *190*(2), 163–179.

Itoh, T., & Tsuji, S. (2003). Migration patterns of young Pacific bluefin tuna (*Thunnus orientalis*) determined with archival tags. *Fishery Bulletin*, *101*, 514–534.

Kishinouye, K. (1923). Contributions to the comparative study of the so-called Scombroid fishes. *Journal of the College of Agriculture, Tokyo Imperial University*, *8*, 295–473.

Kölliker, A. (1857). On the different types in the microscopic structure of the skeleton of osseous fishes. *Proceedings of the Royal Society of London*, *9*(0), 656–668.

Kranenbarg, S., van Cleynenbreugel, T., Schipper, H., & van Leeuwen, J. (2005). Adaptive bone formation in acellular vertebrae of sea bass (*Dicentrarchus labrax* L.). *The Journal of Experimental Biology*, *208*(Pt 18), 3493–3502.

Lauder, G. V., & Tytell, E. D. (2006). Hydrodynamics of undulatory propulsion. In R. E. Shadwick & G. V. Lauder (Eds.), *Fish biomechanics* (pp. 425–468). Amsterdam: Elsevier.

Lauder, G. V., Wainwright, D. K., Domel, A. G., Weaver, J., Wen, L., & Bertoldi, K. (2016). Structure, biomimetics, and fluid dynamics of fish skin surfaces. *Physical Review Fluids*, *1*, 060502.

Madigan, D. J., Baumann, Z., Carlisle, A. B., Hoen, D. K., Popp, B. N., Dewar, H., … Fisher, N. S. (2014). Reconstructing transoceanic migration patterns of Pacific bluefin tuna using a chemical tracer toolbox. *Ecology*, *95*(6), 1674–1683.

Mead, J. G., Walker, W. A., & Houck, W. J. (1982). Biological observations on Mesoplodon carlhubbsi (Cetacea: Ziphiidae). *Smithsonian Contributions to Zoology*, *344*, 1–25.

Meunier, F. J. (1981). Twisted plywood" structure and mineralization in the scales of a primitive living fish *Amia calva*. *Tissue & Cell*, *13*, 165–171.

Meunier, F. J. (2011). The Osteichtyes, from the Paleozoic to the extant time, through histology and palaeohistology of bony tissues. *Comptes Rendus - Palevol*, *10*(5–6), 347–355.

Meunier, F. J., & Brito, P. M. (2004). Histology and morphology of the scales in some extinct and extant teleosts. *Cybium: International Journal of Ichthyology*, *28*, 225–235.

Meunier, F. J., & Huysseune, A. (1992). The concept of bone tissue in osteichthyes. *Netherlands Journal of Zoology*, *42*, 445–458.

Miya, M., Friedman, M., Satoh, T. P., Takeshima, H., Sado, T., Iwasaki, W., … Nishida, M. (2013). Evolutionary origin of the Scombridae (Tunas and Mackerels): Members of a Paleogene adaptive radiation with 14 other pelagic fish families. *PLoS ONE*, *8*(9), e73535.

Moss, M. L. (1961). Studies of the acellular bone of teleost fish 1. Morphological and systematic variations. *Acta Anatomica*, *46*, 343–462.

Moss, M. L. (1965). Studies of the aceullular bone of teleost fish V. Histology and mineral homeostasis of fresh-water species. *Acta Anatomica*, *60*, 262–276.

Nootmorn, P. (2004). Reproductive biology of bigeye tuna in the eastern indian ocean. *IOTC Proceedings*, *7*, 1–5.

Parenti, L. R. (1986). The phylogenetic significance of bone types in euteleost fishes. *Zoological Journal of the Linnean Society*, *87*(1), 37–51.

Park, E.-H., & Lee, S.-H. (1988). Scale growth and squamation chronology for the laboratory-reared hermaphroditic fish Rivulus marmoratus (Cyprinodontidae). *Japanese Journal of Ichthyology*, *34*, 476–482.

Patt, D. I., & Patt, G. R. (1969). *Comparative vertebrate histology* (1st ed.). New York, NY: Harper and Row.

Penney, Z. L., & Moffitt, C. M. (2015). Fatty acid profiles of white muscle and liver in stream-maturing steelhead trout *Oncorhynchus mykiss* from early migration to kelt emigration. *Journal of Fish Biology*, *86*, 105–120.

Phleger, C. F. (1998). Buoyancy in marine fishes: Direct and indirect role of lipids. *American Zoologist*, *38*(2), 321–330.

Potthoff, T. (1975). Development and structure of the caudal complex, the vertebral column, and the pterygiophores in the blackfin tuna (*Thunnus atlanticus*, Pisces, Scombridae). *Bulletin of Marine Science*, *25*, 205–231.

R Development Core Team (2016). *R: A language and environment for statistical computing*. Vienna, Austria: R Foundation for Statistical Computing. Retrieved from https://www.r-project.org/

Revelle, W. (2016). psych: Procedures for personality and psychological research. Northwestern University, Evanston, IL: http://CRAN.R-project.org/package=psych Version = 1.6.6. Retrieved from http://cran.r-project.org/package=psych

Rhodin, A. G. J. (1985). Comparative chondro-osseous development and growth of marine turtles. *Copeia*, *1985*(3), 752–771.

Roberts, C. D. (1993). Comparative morphology of spined scales and their phylogenetic significance in the Teleostei. *Bulletin of Marine Science*, *52*, 60–113.

Rummer, J. L., Wang, S., Steffensen, J. F., & Randall, D. J. (2014). Function and control of the fish secondary vascular system, a contrast to mammalian lymphatic systems. *The Journal of Experimental Biology*, *217*, 751–757.

Santamaria, N., Bello, G., Pousis, C., Vassallo-Agius, R., de la Gándara, F., & Corriero, A. (2015). Fin spine bone resorption in Atlantic bluefin tuna, *Thunnus thynnus*, and comparison between wild and captive-reared specimens. *PLoS ONE*, *10*, 1–17.

Santini, F., Carnevale, G., & Sorenson, L. (2013). First molecular scombrid timetree (Percomorpha: Scombridae) shows recent radiation of tunas following invasion of pelagic habitat. *Italian Journal of Zoology*, *80*, 210–221.

Schönbörner, A. A., Boivin, G., & Baud, C. A. (1979). The mineralization processes in teleost fish scales. *Cell and Tissue Research*, *202*(2), 203–212.

Shahar, R., & Dean, M. N. (2013). The enigmas of bone without osteocytes. *BoneKEy Reports*, *2*, 1–9.

Shephard, K. L. (1994). Functions for fish mucus. *Reviews in Fish Biology and Fisheries*, *4*(4), 401–429.

Sire, J.-Y., & Akimenko, M.-A. (2004). Scale development in fish: A review, with description of sonic hedgehog (shh) expression in the

Supplementary Information for Chapter 3

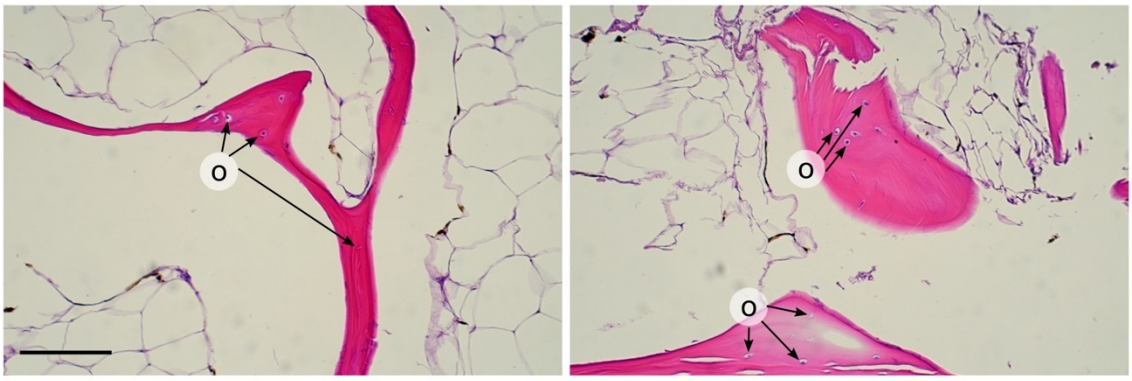

Supplementary Figure 1. Osteocytes in the trabeculae of bigeye tuna scales

4

Ecomorphological evolution of fish scales: habitat-imposed selection generates scale diversity in damselfishes

In revision as:

Wainwright, D.K., Karan, E.A., & Collar, D.C. Ecomorphological evolution of fish scales: habitat-imposed selection generates scale diversity in damselfishes. *Integrative Organismic Biology*.

Abstract

Fish scales are bony plates embedded in the skin that vary extensively in shape across taxa. Despite a plethora of hypotheses about form-function relationships in scales, we know little about the ecological selective factors that shape scale diversity. Here, we present evidence that scale morphology adapts readily to alternative ecologies in a major radiation of teleost fishes, Pomacentridae (damselfishes). We collected surface profilometry measurements from scales and analyzed data using phylogenetic comparative methods to show that ecological transitions between planktivory and benthic feeding are associated with divergent patterns of scale evolution. Scale roughness and spine length evolve toward distinct ecology-associated phenotypic optima, with planktivores evolving smoother scales with longer spines and benthic damselfishes evolving rougher scales with shorter spines. We suggest this pattern may reflect differences in flow experienced by planktivores and benthic-feeding fishes. Smoother surfaces may be beneficial for steady swimming planktivores because smooth surfaces reduce drag in laminar flow. Alternatively, rougher surfaces may increase performance in unsteady swimming benthic-feeding fishes because roughness can be beneficial in turbulent flows, such as in golf ball dimples. These results establish a connection between scale diversity and ecologically-driven adaptive evolution, and they suggest links between scale form and hydrodynamic function.

Introduction

Most bony fish possess scales, and scales exhibit a wide diversity of forms. Fish scales are defined as bony overlapping plates embedded in the dermis, and they can differ in size, shape, amount of exposed surface, as well as the presence, shape, and orientation of spiny projections or ridges (Roberts 1993). Suites of these attributes tend to vary together in major groups of fishes, creating broad categories of scales, such as rounded, smooth-edged cycloid scales or spiny-edged ctenoid

scales, though substantial variation exists within these categories. Indeed, scale morphology has been shown to vary considerably at multiple taxonomic levels—among closely related species (Agassiz 1833; Cockerell 1911; Kobayasi 1955; Roberts 1993; Daniels 1996; Lippitsch 1998), among populations within species (Richards and Esteves 1997; Poulet et al. 2005), between juveniles and adults (Pothoff and Kelley 1982; Frédérich et al. 2010), and even across different body regions on the same individual (Dapar et al. 2012; Wainwright and Lauder 2016; Wainwright et al. 2018). In fact, many species possess spiny ctenoid and smooth edged cycloid scales on different regions of their body (Lippitsch 1998; Ibañez et al. 2009; Wainwright and Lauder 2016). Despite widespread recognition of scale shape as a prominent aspect of fish morphological diversity, the selective factors that shape this diversity are unknown.

A first step in identifying the selective drivers of scale evolution is to link structural variation with functional consequences, and a variety of hypotheses have been proposed. Although scales are multifunctional with purported roles in protection from predators (Browning et al. 2013; Vernerey and Barthelat 2014) and calcium storage (Parenti 1986), many studies into scale functional morphology have proposed that scales influence water flow around swimming fishes (Aleyev 1977; Burdak 1986; Klein and Bleckmann 2015; Wainwright and Lauder 2016, 2018). Previous work has hypothesized that spines, ridges, or scales themselves project into the flow to either decrease drag or increase thrust in turbulent flows (Burdak 1986; Lauder et al. 2016; Wainwright and Lauder 2016; Wu et al. 2018). In addition, studies have proposed that the distribution and shape of scales and spines across the body of fishes may reflect adaptation to the local flows found there (Burdak 1986; Ibañez et al. 2009). Scale morphology therefore may have important consequences for flow around fish as they move through the environment.

In this study, we test whether scale morphology adapts to divergent ecologies by taking advantage of a well-documented axis of ecological diversity in coral reef fish: a continuum between

open-water planktivory and structure-associated grazing in the benthic zone (Findley and Findley 2001; Wainwright et al. 2002; Cooper and Westneat 2009; Price et al. 2012; Friedman et al. 2016). Open water planktivores tend to occur in areas of deeper water adjacent to reefs exposed to direct currents (Odum and Odum 1955; Hobson and Chess 1978; Lazzaro 1987; Hobson 1991; Aguilar-Medrano et al. 2016; Friedman et al. 2016), whereas benthic-associated fish live near shallow-water reef structure where large-scale turbulence and unsteady flows dominate (Fulton and Bellwood 2005; Fulton et al. 2005; Madin et al. 2006; Reidenbach et al. 2006; Koehl et al. 2007; Aguilar-Medrano et al. 2016). Consistent with these differences in flow regimes, planktivores and benthic feeding reef fishes tend to differ in locomotor characters: planktivores tend to have elongate bodies, longer caudal peduncles, higher aspect-ratio pectoral fins, and swim steadily at higher speeds, while benthic feeding fishes have deeper bodies, shorter caudal penduncles, lower aspect pectoral fins and swim unsteadily with more maneuvering (Wainwright et al. 2002; Collar et al. 2008; Aguilar-Medrano et al. 2011, 2016). We further expect that pelagic-feeding fishes would benefit by having smoother surfaces because smooth surfaces reduce drag in the unidirectional laminar flow that is likely experienced by these fishes (Smits 2000). Conversely, benthic-feeding fishes that experience more unsteady and turbulent flow could benefit from having rougher surfaces because some rough surface textures can decrease drag in these general flow conditions, as seen in shark denticles and golf ball dimples (Choi et al. 2006; Oeffner and Lauder 2012). The planktivory to benthic feeding gradient therefore offers a chance to examine whether ecological shifts in feeding, locomotion, and habitat are associated with adaptive evolution toward alternative scale morphologies.

We examine scale evolution in the teleost fish family, Pomacentridae (damselfishes), which is a diverse family of over 380 species (Froese and Pauly 2018) that mostly occur on coral reefs and exhibit repeated transitions between planktivory and benthic feeding (Frédérich et al. 2013). Damselfishes are well studied – we have a good understanding of their phylogeny from the use of

molecular data (Tang 2001; James Cooper et al. 2009; Frédérich et al. 2013), and a range of ecological, morphological, and functional diversity in damselfishes has been described (Emery 1973; Atkinson and Grigg 1995; Ormond et al. 1996; Gluckmann and Vandewalle 1998; Frédérich et al. 2008; Barneche et al. 2009; Cooper and Westneat 2009; Aguilar-Medrano et al. 2013, 2016). We present three-dimensional topographic data describing surface features of scales from a diverse sample of damselfish species that represents the major phylogenetic lineages within the group and multiple transitions between planktivory and benthic feeding. We analyze these data using modern phylogenetic comparative analyses that account for uncertainty in species trait values, phylogeny, and ancestral ecology estimates to reveal morphological adaptation in scales and the selective factors that shape them.

Materials and methods

Specimen sampling

We sampled three to five adult individuals from each of 59 species of damselfishes from the Museum of Comparative Zoology's (MCZ) Ichthyology collection at Harvard University (Supplemental Tables 1 & 2). All specimens were previously preserved in formalin and stored in 70% ethanol. We sampled species that are likely descended from multiple independent evolutionary transitions in feeding ecology, as inferred from the most recent and complete molecular phylogeny of the group (Frédérich et al. 2013). We adopt the feeding ecology categories described in that study: pelagic ecology is feeding mostly on zooplankton in the open water away from structure; benthic ecology is feeding on or near the substrate; and intermediate ecology is feeding in both open water and from substrates (Frédérich et al. 2013). We refer to these different ecologies as pelagic, benthic, and intermediate for brevity (although we consider implications for the definition of these categories

in the discussion below). Our sample of species includes all damselfish genera with over 10 species and spans the major subclades identified in the Frederich et al. (2013) phylogeny. We estimate that our data cover at least 19 independent transitions between pelagic, intermediate, and benthic states (see "Fitting alternative evolutionary models" below).

Imaging scales

Surface topography of scales is crucial to making informative hypotheses about their hydrodynamic function, yet our knowledge of fish skin topography is currently limited (Sudo et al. 2002; Sagong et al. 2008; Liyan et al. 2017; Wainwright et al. 2017). To capture surface topography, we used a gel-based profilometer manufactured by GelSight Inc. (Waltham, MA, USA). This technique can accurately reconstruct surface features of fish scales and other biological surfaces (Wainwright and Lauder 2016; Wainwright et al. 2017). Briefly, gel-based profilometry works by pressing a soft gel with a painted bottom surface into the surface of interest. Six images are taken under lighting from different angles (Johnson and Adelson 2009; Johnson et al. 2011), and GelSight software uses these six images to reconstruct surface topography (Fig. 1).

For each specimen, we imaged the body surface and scales embedded in it on the left side of the body at two locations: a midbody region above the dorsal margin of the pectoral fin and including a portion of the lateral line trunk canal, and a posterior region directly anterior of the narrowed caudal peduncle (Fig. 1a). We captured surface topography of these regions, allowing us to measure surface characteristics in one, two, and three dimensions. To remove topography due to curvature of the body of the fish, we fit a polynomial (6-12 degrees) to the surface using the 'remove form' function of the MountainsMap software (v.7.2.7344, Digital Surf, Besançon, France). This polynomial-fitted surface was removed from the measured surface to obtain only topography of surface features, such as scales, and not topography due to the curved surface of the fish. Then we use MountainsMap to take and

record linear measurements, as well as surface metrology measurements such as root-mean-square roughness (see below).

To prepare surfaces for gel-based profilometry, midbody and posterior regions were lightly brushed before imaging to clear surfaces of debris. Specimens were kept damp with 70% ethanol during imaging to prevent damage from drying, and all specimens were sampled in a non-destructive manner. We collected and reconstructed patches of surface topography at dimensions of either 22 mm by 14 mm or 11 mm by 7 mm, depending on specimen size and shape. Each topographic reconstruction has over 18 million three-dimensional points (5202 x 3565 pixel image reconstructed into 3D).

Measurement of scale morphology

We used images collected from gel-based profilometry to measure several morphological aspects of scales from the midbody and posterior regions (Figure 1). We measured four variables from both regions—roughness, scale aspect ratio, ctenii coverage, and ctenii length (ctenii are small spines that often occur in interlocking fields at the posterior margins of scales [Roberts 1993; Wainwright and Lauder 2016]). In this section, we describe measurement techniques and expected associations between these variables and function.

Roughness describes the variability in height across the examined portion of the body surface. We used topographic data to measure roughness as the root-mean-square of the difference between the height of each point on the surface and the mean height over the entire surface. High values of roughness indicate that the surface is highly variable in height, while low values describe uniform height across the surface. This measure of roughness is a common and fundamental parameter for describing surface characteristics (Whitehouse 1994), and roughness variation is expected to change the nature of flow around objects, with surface features (higher roughness) having the potential to

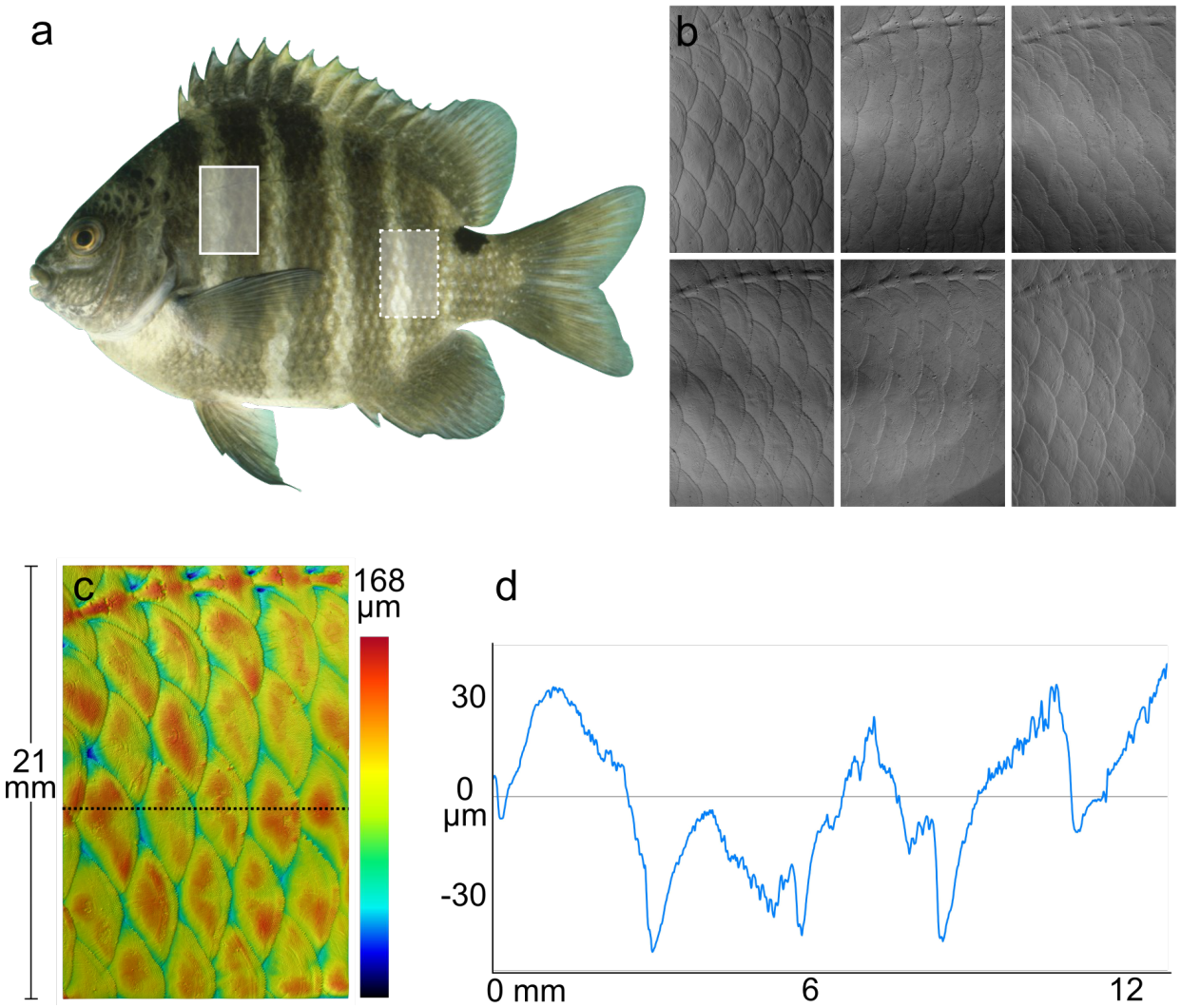

Figure 1. Sampling of damselfish surface topography. (a) Two sampling locations on the surface of damselfishes – one dorsal to the pectoral fin called midbody (shaded with solid line), and another anterior to the peduncle called posterior (shaded with dotted line). Posterior results are shown in supplemental material. (b) Examples of black and white photographs collected during gel-based profilometry where lighting angle is changed, but the specimen remains fixed in position. (c) Three-dimensional surface reconstruction of the six images from (b) where each pixel is assigned a coordinate in 3D space. Warm colors refer to higher heights – height scale at right of image (darkest blue is zero µm). (d) Example of a height profile line from the dotted line in (c). The zero µm height in this profile represents the mean height for the surface in (c).

either increase or decrease drag depending on surface feature geometry and flow conditions. In turbulent flow, for example, elements that increase roughness can decrease drag and sometimes increase thrust, as is seen in dimpled golf balls (Choi et al. 2006), or shark denticle patterns (Oeffner and Lauder 2012; Wen et al. 2015). However, the fluid mechanisms that create drag reduction in these

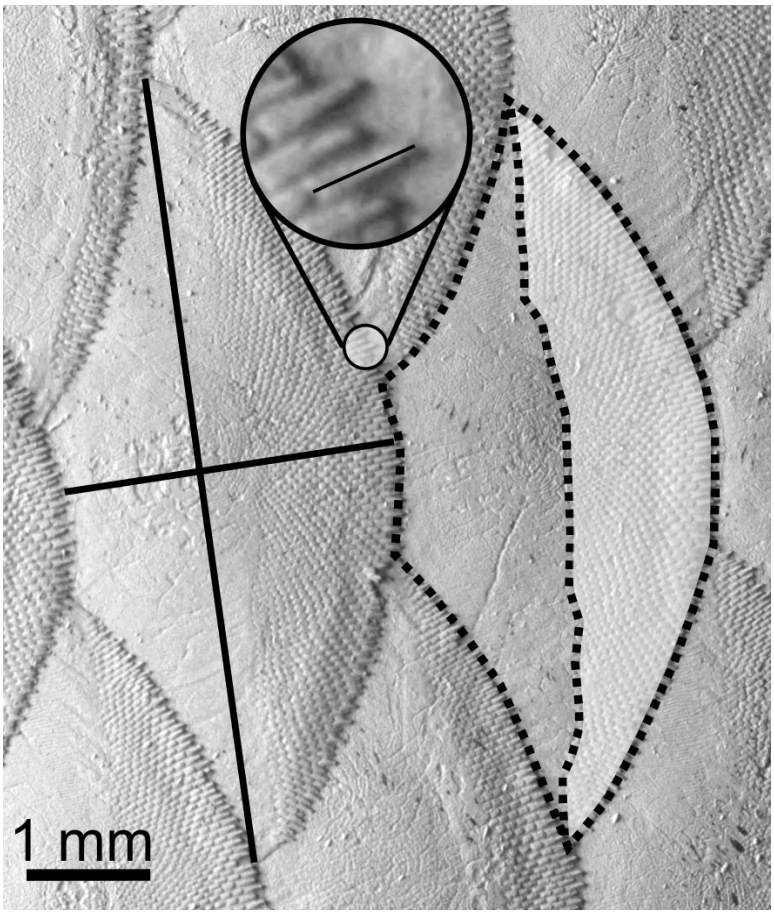

Figure 2. Linear and areal morphological measurements taken from imaging and surface profilometry of scales. Solid intersecting lines indicate scale height and length, which are divided to give aspect ratio. Dotted lines indicate scale area and the shaded area shows the area covered by ctenii. Ctenii coverage is the shaded area divided by the area enclosed by the dotted lines. Circular inset shows how ctenii length is measured.

cases are not always understood, and the complexity of fluid boundary layer make it difficult to predict effects on drag unless the surface happens to be one of the few that have been thoroughly studied. In laminar flow, however, smoother surfaces will decrease drag compared to rough surfaces (Smits 2000).

Scale aspect ratio describes the shape of the exposed surface of the scale. We measured aspect ratio as the visible dorso-ventral height of the scale divided by the visible antero-posterior length (Fig. 2), and we quantified aspect ratio for each region of the body as the mean aspect ratio measured for three scales from that region. Visible scale length is the distance from the midpoint of the anterior-most border of the scale to the midpoint of the posterior-most border of the scale. Visible scale height

is the distance between the dorsal-most and ventral-most points of the scale. Aspect ratio is a simple measure of scale shape and may change fluid flow near the surface.

We also measured ctenii coverage—the percent area of the visible portion of the scale covered in ctenii—and ctenii length—the mean length of individual ctenii on a scale. As described above, we estimated mean ctenii coverage and ctenii length for three scales from each body region (Fig. 2). Ctenii are separate ossification from the rest of thescale, which allows them to rotate at their base, so that their tips can point away from the body of the fish (some evidence for this in [Wainwright and Lauder 2016]). In some species, ctenii also protrude past the skin mucus of fish (Wainwright and Lauder 2018) and are therefore likely to affect flows, perhaps by generating turbulence, organizing it, or by helping to maintain the epidermis and mucus coat (Wainwright and Lauder 2016).

Transformation of variables and size correction

All variables were log transformed and, if needed, corrected for variation due to specimen size. Damselfishes exhibit a relatively limited adult size range, and although we measured only adult specimens, size variation is generally particular to our sample rather than fixed differences in adult size. Across our sample, larger fish tend to have larger scales, and we sought to account for differences in trait values that could be explained by size. To determine whether size-correction was necessary for a particular trait, we regressed log-transformed species mean trait values against log-transformed mean standard length (measured for each specimen prior to profilometry) using phylogenetic linear models fit in the phylolm package (Ho and Ane 2014) for R (R Development Core Team 2018) under a lambda model (Pagel 1999) and using phylogenetic relationships estimated in Frédérich et. al 2013 (Frédérich et al. 2013). We repeated regressions across a posterior sample of 100 trees (from Frédérich et al. 2013) and determined that a variable needed size correction when the mean p-value was below 0.05. According to this scheme, roughness and ctenii length needed size correction but aspect ratio

and percent ctenii coverage did not. We obtained size-corrected values for each specimen as the residual deviations from the estimated regression lines fitted in the manner described above, which resulted in a set of size-corrected trait values for each of the 100 phylogenetic trees. We used each tree-specific set of residuals and its corresponding phylogenetic tree as input for evolutionary model fitting (see below).

Fitting alternative evolutionary models

To test the hypothesis that scale morphology evolves in response to feeding habitat-imposed selection, we fit models of adaptive evolution to species values for scale variables and reconstructions of phylogeny and ancestral habitat use (Felsenstein 1985; Hansen 1997; Butler and King 2004; Beaulieu et al. 2012). If benthic and pelagic habitats have exerted divergent selective demands on damselfish scales, we expect the best-fit model(s) to include distinct adaptive peaks associated with these two habitats. In contrast, if scale evolution is unrelated to these factors, simpler models that exclude habitat-associated optima should receive more support. Therefore, by fitting alternative models to individual scale variables, we are able to identify ecomorphological associations during evolution.

For each scale variable, we fit a series of Ornstein-Uhlenbeck (OU) evolutionary models that specify multiple adaptive peaks associated with alternative feeding ecologies. In these multi-peak OU models, trait evolution in a lineage is determined by the optimum trait value associated with its inferred ecology, θ, the rate of adaptation towards that optimum, α, and a rate of stochastic evolution that causes dispersion around the optimum, $\sigma 2$ (Hansen 1997; Butler and King 2004). Lineages that differ in inferred habitat state evolve toward separate habitat-specific θs, but for simplicity, α and $\sigma 2$ are held constant across all damselfish lineages. We fit a three-peak model (OU3M) where each of the three categories (pelagic, intermediate, benthic) has a separate optimum. We also fit two two-peak models in which the intermediate category has been combined with either the pelagic ecology (OU2M-pelagic)

Table 1: Evolutionary models used to fit data and their interpretations.

Model	θ	σ^2	α	If this model fits best then…
BM1	Global	Global	none	Trait evolution is not affected by ecology and is unconstrained
OU1	Global	Global	Global	Trait evolution is unaffected by ecology but it is constrained by attraction to a single optimum
OU3M	State-specific	Global	Global	Trait evolves toward distinct optima for benthic, pelagic, and intermediate ecologies
OU2M pel	State-specific	Global	Global	Trait evolves toward a distinct optimum for pelagic ecology or a shared optimum for benthic and intermediate ecologies.
OU2M ben	State-specific	Global	Global	Trait evolves toward a distinct optimum for benthic ecology or a shared optimum for pelagic and intermediate ecologies

or the benthic ecology (OU2M-benthic). Support for the OU3M model indicates that each of the three ecologies experiences a different selective regime (Table 1). Support for the OU2M-pelagic model suggests that the benthic ecology experiences a different selective regime (and therefore has a separate optima) compared to the combined pelagic and intermediate regimes. Similarly, support for the OU2M-benthic model indicates that the pelagic ecology has a separate optimum and therefore a different selective regime compared to the combined intermediate and benthic ecologies. Support for any multi-peak model provides evidence that the planktivore-to-benthic feeding axis in reef fishes plays a role in scale evolution.

We also fit two evolutionary models that include no effect of ecology on scale evolution. The simplest model is Brownian motion (BM) with a single evolutionary rate (σ2) and ancestral state (θ). In addition, we fit a single-peak OU model (OU1) (Hansen 1997; Butler and King 2004; Beaulieu et al. 2012), which describes trait evolution towards a single optimal value, regardless of ecology, under constant α and σ2. Support for either BM or OU1 indicates that scale evolution is unrelated to ecology.

For each scale variable, we fit evolutionary models using maximum likelihood as implemented in the OUwie package (Beaulieu and O'Meara 2016) for R. All analyses incorporated within-species trait variation by including estimates of standard errors for species means. To account for uncertainty in phylogeny and ancestral character state estimation, we repeated model fitting across a sample of

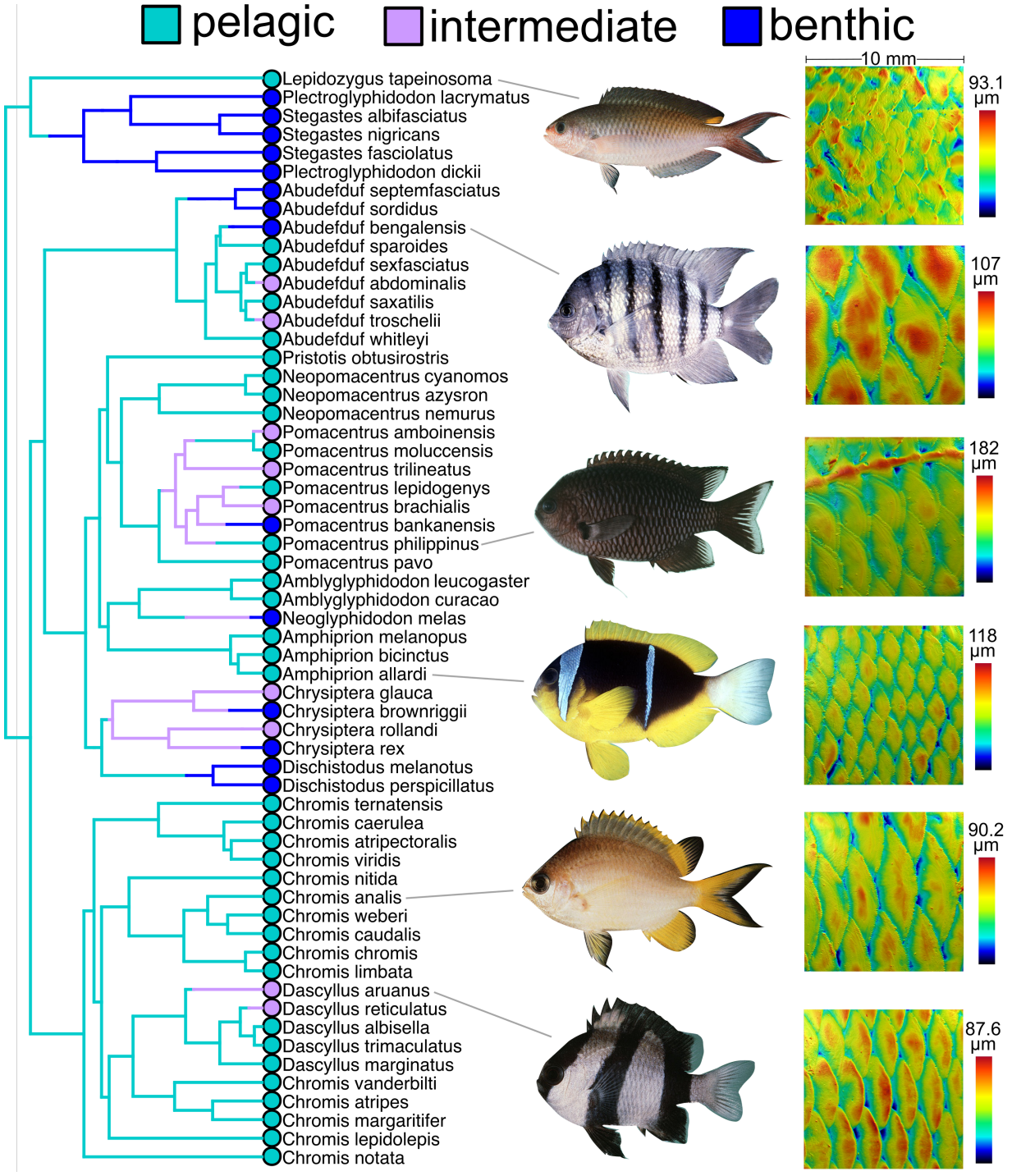

Figure 3. Pruned consensus tree from (Frédérich et al. 2013) including all species sampled in this study with tips colored by ecological category and branches colored based on a single stochastic character map. Grey lines indicate species photographs shown (photos from (Randall n.d.)). Example topographic maps of scaled surfaces are given for the pictured species at right. Note that each topographic image has a different height scale.

phylogenetic trees and feeding habitat reconstructions. We used the same 100 trees from the posterior distribution of Frédérich et. al 2013 (Frédérich et al. 2013) that we used in phylogenetically-informed

size correction (see above). For each tree we sampled five reconstructions of ancestral feeding ecology using stochastic character mapping (Huelsenbeck et al. 2003) under an equal-transition-rates Markov model, as implemented in the function make.simmap in the phytools package (Revell 2012) for R. We pruned each of our 500 phylogenetic and ecological reconstructions (referred to as reconstructions from this point forward) down to the 59 sampled species in our dataset. An example stochastic character map is shown in Fig. 3. Our 500 stochastic character maps inferred a median of 26 transitions between pelagic, intermediate, and benthic ecologies, with a range of 19 to 45 inferred transitions.

We compared the fit of the five models (BM, OU1, OU3M, OU2M-pelagic, OU2M-benthic) for each of our four variables (roughness, scale aspect ratio, ctenii coverage, ctenii length) using sample size corrected Akaike information criterion (AICc: Table 2) (Burnham and Anderson 2002). For each reconstruction, we calculated each model's ΔAICc, the difference between its AICc and the AICc of the best-fit model (i.e., the model with the lowest AICc). We also used these values to calculate Akaike weights (wAICc), the proportion of model support relative to the total support received by all fitted models (Burnham and Anderson 2002). This procedure led to distributions of model-specific ΔAICc and wAICc evaluated across reconstructions. To determine the best supported model(s), we compared mean wAICc. To describe the robustness of these results to phylogenetic and ancestral state uncertainty, we present the percent of reconstructions for which a model was favored (see Table 2). While we show results from the three multi-peak OU models separately, we consider their cumulative support (i.e., the sum of wAICc for OU3M, OU2M-pelagic, and OU2M-benthic) when evaluating support for the hypothesis that habitat influences scale evolution. Because all three models specify separate optima for pelagic and benthic feeding, the total Akaike weight for the three models indicates the empirical support for adaptive scale evolution.

We also calculated Akaike weighted model parameters (Supplemental Table 3), including θpelagic, θbenthic, α, and σ2, which are calculated as the mean parameter estimates from the five

Table 2. Model support for variables measured from the midbody region of scales given as the mean and 95% confidence interval of AICc scores for each model (in brackets), model selection as the wAICc and 95% confidence (in brackets), and robustness of model selection as the percent of time a model has the lowest dAICc score (% preferred). Support values taken from analyses of 100 trees with five stochastic character maps per tree. Values for wAICc are bolded where they represent a majority of the support. All three multi-peak models are bolded together as they provide cumulative support for ecology-associated adaptive evolution.

Trait	Model	mean AICc	mean wAICc	% preferred
Aspect ratio	BM	-198.0 [-202.2, -193.6]	0.25 [0.08, 0.42]	25
	OU	-198.4 [-201.4, -194.6]	0.30 [0.11, 0.42]	48
	OU3M	-196.4 [-201.2, -191.1]	0.12 [0.04, 0.37]	6
	OU2M pelagic	-196.9 [-200.3, -192.8]	0.13 [0.08, 0.22]	1
	OU2M benthic	-197.6 [-201.9, -193.1]	0.20 [0.10, 0.44]	20
Ctenii coverage	BM	-133.1 [-134.7, -131.6]	**0.53** [0.33, 0.62]	98
	OU	-131.0 [-132.5, -129.4]	0.18 [0.12, 0.21]	0
	OU3M	-128.3 [-131.9, -125.9]	0.06 [0.02, 0.17]	1
	OU2M pelagic	-129.6 [-131.7, -127.5]	0.09 [0.06, 0.14]	0
	OU2M benthic	-130.3 [-133.3, -128.0]	0.14 [0.07, 0.30]	1
Ctenii length	BM	-164.3 [-170.1, -158.3]	0 [0.00, 0.00]	0
	OU	-179.3 [-182.2, -177]	0.35 [0.14, 0.54]	56
	OU3M	-177.1 [-181.1, -173.7]	**0.11** [0.06, 0.22]	0
	OU2M pelagic	-178.4 [-182.3, -175.4]	**0.22** [0.11, 0.40]	12
	OU2M benthic	-179.1 [-182.6, -175.9]	**0.31** [0.18, 0.51]	31
Roughness	BM	-61.6 [-67.9, -52.7]	0 [0.00, 0.00]	0
	OU	-79.0 [-80.6, -77.4]	0.01 [0.00, 0.03]	0
	OU3M	-85.5 [-88.9, -82.7]	**0.24** [0.11, 0.39]	5
	OU2M pelagic	-85.8 [-88.4, -83.3]	**0.31** [0.08, 0.54]	32
	OU2M benthic	-86.6 [-90.3, -83.7]	**0.43** [0.20, 0.71]	63

different evolutionary models weighted by each model's wAICc (note that $\theta_{pelagic} = \theta_{benthic} = \theta$ for BM and OU1 models). We used these model-averaged estimates because, for several variables, empirical support is spread across multiple models. Weighted parameter estimates integrate over this uncertainty in model selection and can improve on estimation compared to the best-fit model alone (Burnham and Anderson 2002). We note, however, that for estimates of optima in pelagic versus benthic ecologies, model averages are in agreement with estimates from the preferred model.

To account for the tendency of model selection to erroneously support complex models over simpler ones (Boettiger et al. 2012; Cooper et al. 2016), we evaluated the empirical support for multi-peak models against a null distribution based on simulation under single-rate Brownian motion evolution. For the two morphological variables that showed support for multi-peak models—roughness and ctenii length (see Results section below)—we simulated 100 data sets using empirical estimates of $\sigma 2$ and θ. For each simulated data set, we repeated the analysis described above; we fit alternative models for each of 100 phylogenetic trees and ecology reconstructions (subsampled from the full set of reconstructions used in the main analysis) and summarized support for multi-peak models as mean wAICc and the proportion of reconstructions for which multi-peak models were preferred. Repeating this analysis over 100 simulated data sets produced a null distribution for multi-peak model support under Brownian motion evolution. We then compared our empirical support for multi-peak OU models to this distribution to estimate the probability of falsely inferring the role of ecology-imposed selection on scale evolution.

Results

Midbody region

We found support for evolution toward alternative feeding habitat-imposed optima in roughness and ctenii length (Table 2). Support for alternative adaptive optima is especially strong and robust for roughness; the cumulative mean wAICc for the three multi-peak models is 0.98 (OU3M: 0.24, OU2M-pelagic: 0.31, OU2M-benthic: 0.43) and multi-peak models were favored across 100% of reconstructions (OU3M: 5%, OU2M-pelagic: 32%, OU2M-benthic: 63%). Model weighted optima show that pelagic damselfishes have evolved to a lower-roughness optimum than benthic damselfishes (Fig. 4, Supplemental Table 3).

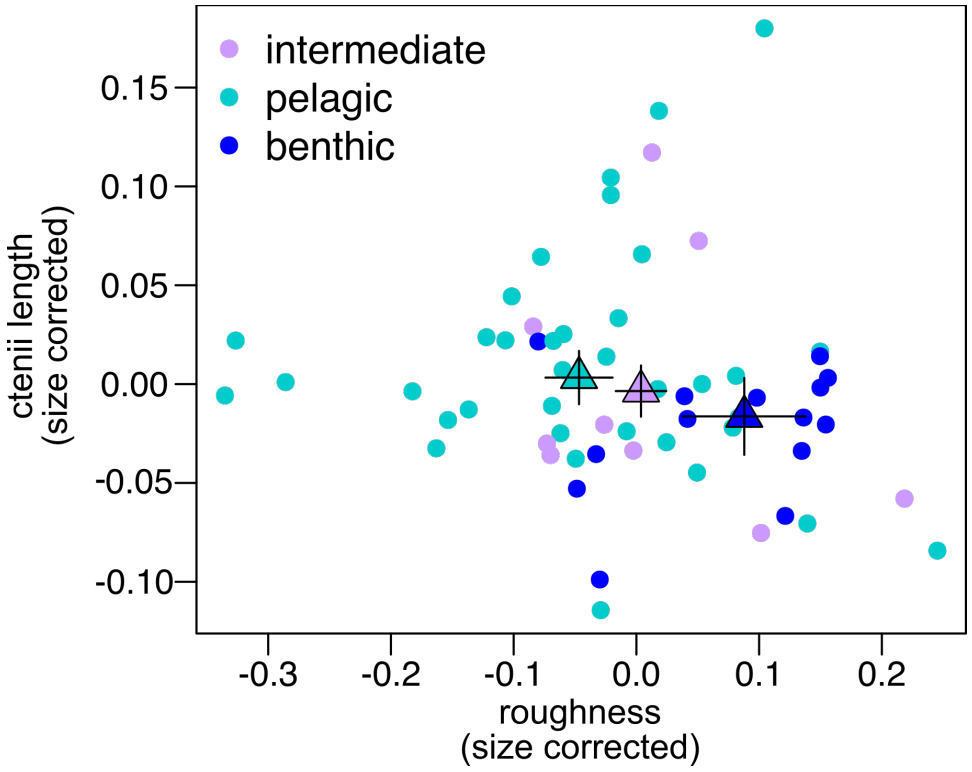

Figure 4. Species means plotted with model weighted optima and standard errors (+/- one standard error given by bars). Model weighted optima given as filled triangles. Log transformed and size corrected ctenii length plotted against log transformed and size corrected roughness. The pelagic ecology has a model weighted optimum with lower roughness and longer ctenii than the benthic ecology.

For ctenii length we also found evidence for habitat-associated adaptive evolution toward separate pelagic- and benthic-associated optima, but support was less robust to uncertainty in phylogeny and ancestral state reconstruction. For ctenii length, multi-peak OU models received a majority of Akaike weight (cumulative wAICc = 0.64; OU3M: 0.11, OU2M-pelagic: 0.22, OU2M-benthic: 0.31). However, these models were favored for only 43% of reconstructions, indicating that support varies substantially across alternative reconstructions. Instead, the OU1 model is favored over a majority (56%) of reconstructions. Although we cannot rule out the possibility that ctenii length evolution has been constrained by a global optimum shared by all damselfish lineages, model weighted estimates suggest separation between pelagic and benthic optima, with pelagic damselfishes evolving longer ctenii compared to benthic damselfishes (Fig. 4; Supplemental Table 3).

Furthermore, despite the tendency for model selection to favor complex models over simpler ones (Boettiger et al. 2012; Cooper et al. 2016), simulations reveal that the level of empirical support we found for multi-peak OU models is unlikely under a simpler model of Brownian motion evolution (details in Supplementary material).

Ctenii coverage was not influenced by alternative feeding habitats (Table 2, Supplemental Figure 3). In fact, we found little evidence of adaptive constraint on ctenii coverage, as BM was strongly and robustly preferred over OU models; BM received Akaike weights over 0.5 and were preferred in 98% of reconstructions.

Model selection was less clear for scale aspect ratio (Table 2), but single-peak OU and Brownian models combined together have a majority of support; BM and single-peak OU models together have Akaike weights over 0.5 (BM: 0.25, OU1: 0.30) and were preferred in 63% of reconstructions (BM: 25%, OU1: 38%). There is also support for the multi-optima models for scale aspect ratio with a combined wAICc of 0.45 (Table 2). However, despite the support for the multi-optima models, the model-averaged optima show very little difference between benthic and pelagic ecologies and instead show intermediate as different (Supplementary table 3). The general support for the BM and OU1 models combined with the model optima values suggest that scale aspect ratio is not responding to evolution driven by feeding ecology.

Posterior region

Results for scale morphology in the posterior body region were largely concordant with midbody scale results. Scale variables from these two regions were strongly correlated (Supplemental Table 9), and so we present results and discussion for posterior scales in the supplemental material.

Discussion

Scales are common to the majority of fishes and exhibit a diversity of forms, yet we have an incomplete understanding of the selective factors that shape this diversity. In this study, we present a novel interspecific morphological dataset describing multiple aspects of scale three-dimensional structure in a diverse clade of fishes, and we identify evolutionary links between scale form and ecology for the first time. In damselfishes, transitions between a pelagic, planktivorous ecology and a benthic, grazing ecology are associated with divergence in scale morphology as pelagic-feeding lineages evolve smooth scales with long ctenii and benthic lineages evolve rough scales with shorter ctenii.

These results support the hypothesis that fish scale morphology evolves in response to selective demands of movement through alternative flow regimes associated with pelagic and benthic habitats. Damselfish are active foragers that swim while they feed (Emery 1973; Allen 1975, 1991), and the flow characteristics of feeding habitats are likely to impose demands on locomotor performance. Planktivores forage above the reef in open water and tend to swim oriented towards incoming flow in deeper upwelling areas near reefs or at reef edges (Davis and Birdsong 1973; Thresher 1983; Lazzaro 1987; Wainwright and Bellwood 2002; Cooper and Westneat 2009; Frédérich et al. 2009). In contrast, benthic grazers tend to move around the structure of the reef feeding on organisms attached to substrates (Ogden et al. 1978; Wainwright and Bellwood 2002; Olivier et al. 2016). While planktivorous species mostly experience unidirectional flows with less turbulence in the open water, benthic-feeding fishes are likely experiencing more unsteady and turbulent flows as they maneuver near structure (Ormond et al. 1996; Reidenbach et al. 2006; Binning and Roche 2015). These flow regimes impose different demands on fish swimming performance, and in many groups of reef fish, divergence in feeding habitats is linked to differentiation in locomotor adaptations; planktivores show morphologies and behaviors that increase steady swimming speeds whereas benthic feeding fishes exhibit forms and behaviors associated with better maneuvering and unsteady swimming

(Fulton et al. 2001; Wainwright et al. 2002; Walker and Westneat 2002; Collar et al. 2008; Aguilar-Medrano et al. 2016). We therefore argue that divergent scale morphologies in pelagic versus benthic feeding damselfish result from adaptive evolution to enhance locomotor performance in the flow regimes imposed by alternative foraging habitat. In the following sections, we consider the ecomorphological associations documented here and previous ideas about scale function in light of these demands from habitat-linked flows.

Roughness

We find robust support for evolutionary models that infer pelagic damselfish have evolved smoother scales while benthic lineages have evolved rougher surfaces. This model-fitting result aligns with the expectation that teleost scales function to reduce drag on the bodies of swimming fish. In the laminar flow of steadily swimming planktivores, smooth body surfaces will keep drag low. In the unsteady and turbulent flows of the benthic zone, scale roughness and surface features can help decrease drag (Choi 1989; Smits 2000; Jimenez 2004; Schultz and Flack 2007; Wainwright and Lauder 2016). The consistency we find between our results and expectations for drag reduction suggests that scale roughness adapts readily to the alternative flow regimes damselfishes experience.

Despite this link between scale roughness and ecologically relevant function, future experiments are needed to test the mechanisms by which scales reduce drag or otherwise increase swimming performance. Previous work has proposed a variety of hydrodynamic functions by which scales could increase swimming performance across different flow conditions (Aleyev 1977; Burdak 1986; Wainwright and Lauder 2016), but experimental results have yet to confirm these hypotheses. While two studies have been able to show that boundary layer flows can oscillate between laminar and turbulent around two different swimming teleosts (Anderson et al. 2001; Yanase and Saarenrinne 2015), no study has explicitly shown evidence that scales or scale features influence flow around fish.

The only studies to investigate hydrodynamic effects of teleost scales do so with physical or computer models that represent single species (Sagong et al. 2008; Liyan et al. 2017). Whereas there is no indication of drag reduction in physical models of sailfish skin (Sagong et al. 2008), computational models of grass carp scales do in fact demonstrate mechanisms for drag reduction (Liyan et al. 2017). Together these studies suggest that species-specific surface geometry and testing conditions can change results, though neither study uses methods for accurate topographic reconstruction of fish surfaces nor do they account for the effect of mucus on fish surfaces. While more work is needed in this area before any broader conclusions can be drawn about the relationship between fish scale roughness and hydrodynamic function, our results show that fishes experiencing more unsteady and turbulent flows tend to evolve rougher surfaces than fishes experiencing more steady flows.

Although our evolutionary model fitting results recover separate roughness optima for pelagic and benthic feeding damselfishes, we find that these ecological groups overlap along this axis (Fig. 4). We note that this overlap is not unexpected under the multi-peak OU model. According to Hansen's (1997) biological interpretation of the model, the optima we estimate represent the effects of shared selective demands on species phenotypes. Because species differ in many unconsidered ways, we expect the pull of shared selection to affect species differently, resulting in a spread of species-specific optima. Our results reveal that selection imposed by the flow regimes of different reef habitats has a tendency to similarly shape surface roughness, but selection is not so strong as to overwhelm species-specific constraints on evolution.

Nevertheless, the pattern of overlap that we observe—the pelagic-feeding group has a wide range of scale roughness, but benthic-feeders exhibit only rough surfaces (Fig. 4)—suggests that benthic feeding may impose stronger constraints on roughness compared to pelagic feeding (we note that this is also true for ctenii length as well; see below). The evolution of scale morphology in damselfishes may be more complex than the multi-peak evolutionary models we fit in this study (see

Caveats section in Supplementary Material). While evolutionary optima (θ) do appear different between feeding ecologies, it may be that the rate of adaptation to the optimum (α) or the rate of stochastic evolution around the optimum (σ2) are also different and lead to a narrower range of benthic-feeding ecologies. The biological explanation for stronger functional constraints in the scale morphology of benthic-feeding damselfishes is not clear to us, and it does not appear to mirror patterns shown in feeding or locomotor-related traits in this group (Frédérich et al. 2013; Aguilar-Medrano et al. 2016).

Another potential explanation for the overlap in morphology between pelagic and benthic-feeding damselfishes is that our feeding-ecologies do not perfectly predict swimming behavior and flow environment. For example, many of the pelagic-feeding species that have high roughness are in the genus *Dascyllus* (see Supplementary Figures 1 and 2). While these species are certainly planktivores, they often shelter in branching corals and disperse above these structures to feed (Allen 1991), which perhaps helps to explain their high roughness. Also, damselfishes all lay sticky eggs onto substrates and guard them until hatching. This means that even pelagic-feeding species will spend time living near structure during egg guarding behaviors, potentially weakening the relationship between feeding ecology and flow environment. Nonetheless, our analysis provides strong support for roughness as an important functional feature of damselfish scales despite the limitations of broad ecological categories.

Ctenii length

We also find that ctenii increase in length in damselfish with pelagic and intermediate ecologies and become shorter in benthic lineages. Ctenii and other bony projections are ubiquitous on the scales of most teleost fishes, with three of the four categories of teleost scales (crenate, spinoid, ctenoid) based on ctenii presence, shape, and arrangement (Roberts 1993). Our results suggest that ctenii

morphology evolves in response to functional demands imposed by habitat. However, similar to the uncertainty surrounding the hydrodynamic function of roughness, hypotheses concerning hydrodynamic function of ctenii are as yet untested (Lauder et al. 2016; Wainwright and Lauder 2016).

Like most fishes, the ctenii of damselfishes tend to be small (75-300 μm long) compared to the scales they attach to (1 to 5 mm long), and they are complete only at the posterior edge of the scale. Because of their small size, ctenii do not contribute much to roughness measurements, which are instead largely determined by size, shape, and inclination angle of whole scales (Wainwright and Lauder 2016; Wainwright et al. 2017). Nevertheless, ctenii may still change flows inside the boundary layer of swimming fishes, similar to how the denticles of sharks (hundreds of microns in length) alter flows (Oeffner and Lauder 2012). Most hypotheses on the function of ctenii suggest that they decrease drag in turbulent flow either by organizing the boundary layer into beneficial vorticies or by preventing backflow during separation of the boundary layer (Lauder et al. 2016; Wainwright and Lauder 2016). Both of these hydrodynamic effects mirror the function of shark denticles, which are of a similar size-scale to most ctenii (Motta et al. 2012; Domel et al. 2018). Under these hypotheses, we might expect benthic damselfishes that experience more unsteady and turbulent flows to have larger ctenii compared to species with pelagic ecologies that experience more unidirectional laminar flows. However, we see the opposite trend (though we note that our model averaged optima are not well differentiated and the OU1 model, which does not account for ecological differences, receives substantial support: Fig. 4, Supplemental Table 3).

This lack of congruence between hydrodynamic expectations and our results may be partially explained by considering that epidermis and mucus cover scales in most fishes. In fact, new evidence suggests that ctenii can be obscured from the surrounding fluid by mucus (Wainwright and Lauder 2018). Because we measured preserved material, we do not know the appearance of the surface when epidermis and mucus is intact. Therefore, we cannot determine if damselfish ctenii protrude past the

mucus layer. Nevertheless, fish mucus is thought to reduce drag during pulsing laminar flow or turbulent flow (Daniel 1981; Bernadsky et al. 1993), so it is possible that benthic damselfishes experiencing more unsteady and turbulent flows would produce more mucus to reduce friction drag across the body. In this case, ctenii may be smaller in benthic fishes to minimize the likelihood that they would protrude past the mucus layer and disrupt mucus-based drag reduction. Damselfishes in the pelagic ecology may then have longer ctenii because ctenii may reduce drag in steady flows, perhaps by keeping flow organized in the streamwise direction as seen in surfaces with ridges parallel to flow (Bechert and Bartenwerfer 1989).

Just as the presence of epidermis and mucus affect the exposure of ctenii to flow, these features also likely influence surface roughness. Recent research in other fishes shows that epidermis and mucus on scales decreases surface roughness but do not change roughness relationships between species (Wainwright and Lauder 2018). We therefore expect that the roughness differences we identify between damselfish species are likely to be similar when mucus is present.

Similar to the spread of species values for roughness, we find overlap in ctenii length between the benthic-feeding species and the pelagic-feeders, with the pelagic species occupying a larger range of ctenii lengths and benthic-feeding species limited to shorter ctenii lengths. Of the pelagic species with short ctenii lengths, *Pristotis obtusirostris* and species in the genus *Dascyllus* have the shortest ctenii lengths (Supplementary Figures 1 and 2). *P. obtusirostris* has a different ecology than most damselfishes because it is largely found over soft substrates and not the rocky reef habitats that are more typical of other damselfishes (Travers et al. 2010), and this habitat may present different flow conditions. As mentioned in the previous section, *Dascyllus spp.* are well known for sheltering and feeding above branching corals, which may complicate the flow environment that they experience and perhaps explain their small ctenii.

Aspect ratio and ctenii coverage

Neither aspect ratio nor ctenii coverage shows clear evidence of adaptation toward shared ecology-imposed optima (Table 2, Supplementary Figure 3). Instead, scale aspect ratio shows mixed support between all models with better support in the Brownian and single-peak OU models compared to the multi-optima models, and ctenii coverage shows strong support for the Brownian model. One explanation for this result is that these aspects of scale morphology have little effect on flow around the swimming fish, resulting in weak habitat-imposed selection on them during the evolutionary history of damselfishes. Brownian evolution does not necessarily rule out ecologically relevant functional consequences for these characters, however. If multiple values for these characters result in similar hydrodynamic function (i.e., if the relationship between scale shape and function is many-to-one [Wainwright 2007; Alfaro et al. 2014]), we would expect a relatively weak association between habitat and morphology. In addition, if constraints on these aspects of scale shape vary among damselfish lineages, there may be little tendency to adapt to similar trait values. Because damselfishes vary in many ways beyond the zooplanktivory-benthic axis, species that share the same ecology may nevertheless be attracted to distinct phenotypic optima (Hansen 1997) or may be subject to different magnitudes of selection (Beaulieu et al. 2013). Although we are unable to differentiate between these alternative evolutionary scenarios, the lack of widely shared constraints on aspect ratio and ctenii coverage means that these aspects of scale shape can diversify even among lineages that share similarities in other scale attributes because of ecology-imposed selection. We propose that this mosaic of adaptive and non-adaptive evolution of scale characters may be a major driver of the diversity of scales across teleost fishes.

Conclusion

Scales are a common feature of ray-finned fishes, yet we understand little of how scale form is shaped by evolution and how scale form influences function. We show evidence of ecologically imposed selection acting to change scale morphology in damselfishes. Pelagic damselfishes have larger ctenii and smoother surfaces, and benthic species have smaller ctenii and rougher surfaces. This pattern supports previous hypotheses about the relationship between scale morphology and its functional and ecological consequences, though we emphasize that links between scale morphology and flows across the fish body remain to be tested. Future studies investigating the nature of boundary layer flows over scales with different morphology would further our understanding of the function of roughness and ctenii length and the flows around swimming fish. Also, additional morphological and experimental work is needed to understand both the topography of fish surfaces with mucus present and how mucus effects boundary layer flows. Nevertheless, the associations we find between scale evolution and trophic ecology support the idea that diversity in fish scale morphology is functionally and ecologically relevant, yet largely unexplored. We hope this work encourages additional studies of fish scale functional morphology and evolution.

References

Agassiz, L. 1833. Recherches sur les poissons fossiles: Tome 2. Petitpierre.

Aguilar-Medrano, R., B. Frédérich, E. F. Balart, and E. de Luna. 2013. Diversification of the pectoral fin shape in damselfishes (Perciformes, Pomacentridae) of the Eastern Pacific. Zoomorphology 132:197–213.

Aguilar-Medrano, R., B. Frédérich, and P. H. Barber. 2016. Modular diversification of the locomotor system in damselfishes (Pomacentridae). J. Morphol. 277:603–614.

Aguilar-Medrano, R., B. Frédérich, E. De Luna, and E. F. Balart. 2011. Patterns of morphological evolution of the cephalic region in damselfishes (Perciformes: Pomacentridae) of the Eastern Pacific. Biol. J. Linn. Soc. 102:593–613.

Aleyev, Y. G. 1977. Nekton.

Alfaro, M. E., D. I. Bolnick, P. C. Wainwright, S. Evolution, and N. Mar. 2014. Evolutionary dynamics of complex biomechanical systems : An example using the four-bar mechanism. Evolution. 58:495–503.

Allen, G. R. 1975. Damselfishes of the south seas. T. F. H. Publications, Inc.

Allen, G. R. 1991. Damselfishes of the world. Mergus publishers Hans A. Baensch.

Anderson, E. J., W. R. McGillis, and M. A. Grosenbaugh. 2001. The boundary layer of swimming fish. J. Exp. Biol. 204:81–102.

Atkinson, M. J., and R. W. Grigg. 1995. Spatial patterns in the distribution of damselfishes on a fringing coral reef. Coral Reefs 14:151–161.

Barneche, D. R., S. R. Floeter, D. M. Ceccarelli, D. M. B. Frensel, D. F. Dinslaken, H. F. S. Mário, and C. E. L. Ferreira. 2009. Feeding macroecology of territorial damselfishes (Perciformes: Pomacentridae). Mar. Biol. 156:289–299.

Beaulieu, J. M., D. Jhwueng, C. Boettiger, and B. C. O'Meara. 2012. Modeling stabilizing selection:

expanding the Ornstein-Uhlenbeck model of adaptive evolution. Evolution. 66:2369–2383.

Beaulieu, J. M., and B. C. O'Meara. 2016. OUwie: Analysis of evolutionary rates in an OU framework. R package version 1.50.

Beaulieu, J. M., B. C. O'Meara, and M. J. Donoghue. 2013. Identifying hidden rate changes in the evolution of a binary morphological character: The evolution of plant habit in campanulid angiosperms. Syst. Biol. 62:725–737.

Bechert, D. W., and M. Bartenwerfer. 1989. The viscous flow on surfaces with longitudinal ribs. J. Fluid Mech. 206:105–129.

Bernadsky, G., N. Sar, and E. Rosenberg. 1993. Drag reduction of fish skin mucus: Relationship to mode of swimming and size. J. Fish Biol. 42:797–800.

Binning, S. A., and D. G. Roche. 2015. Water flow and fin shape polymorphism in coral reef fishes. Ecology 96:828–839.

Boettiger, C., G. Coop, and P. Ralph. 2012. Is your phylogeny informative? Measuring the power of comparative methods. Evolution. 66:2240–2251.

Browning, A., C. Ortiz, and M. C. Boyce. 2013. Mechanics of composite elasmoid fish scale assemblies and their bioinspired analogues. J. Mech. Behav. Biomed. Mater. 19:75–86.

Burdak, V. D. 1986. Morphologie fonctionnelle du tegument ecailleux des poissons. Cybium 10:1–128.

Burnham, K. P., and D. R. Anderson. 2002. Model selection and mixed model inference: a practical information-theoretic approach. 2nd ed. Springer New York, New York, New York, USA.

Butler, M. A., and A. A. King. 2004. Phylogenetic comparative analysis: A modeling approach for adaptive evolution. Am. Nat. 164:683–695.

Choi, J., W. P. Jeon, and H. Choi. 2006. Mechanism of drag reduction by dimples on a sphere. Phys. Fluids 18:16–19.

Choi, K.-S. 1989. Near-wall structure of a turbulent boundary layer with riblets. J. Fluid Mech. 208:417–458.

Cockerell, T. D. A. 1911. The scales of freshwater fishes. Biol. Bull. 20:367–387.

Collar, D. C., P. C. Wainwright, and M. E. Alfaro. 2008. Integrated diversification of locomotion and feeding in labrid fishes. Biol. Lett. 4:84–86.

Cooper, N., G. H. Thomas, C. Venditti, A. Meade, and R. P. Freckleton. 2016. A cautionary note on the use of Ornstein Uhlenbeck models in macroevolutionary studies. Biol. J. Linn. Soc. 118:64–77.

Cooper, W. J., and M. W. Westneat. 2009. Form and function of damselfish skulls: rapid and repeated evolution into a limited number of trophic niches. BMC Evol. Biol. 9:24.

Daniel, T. L. 1981. Fish mucus: In situ measurements of polymer drag reduction. Biol. Bull. 160:376–382.

Daniels, R. A. 1996. Guide to the identification of scales of inland fishes of northeastern North America. New York State Museum Bull. 488:1–93.

Dapar, M. L. G., M. A. J. Torres, P. K. Fabricante, and C. G. Demayo. 2012. Scale Morphology of the Indian goatfish, *Parupeneus indicus* (Shaw 1803) (Perciformes: Mullidae). Adv. Environ. Biol. 6:1426–1432.

Davis, W. P., and R. S. Birdsong. 1973. Coral reef fishes which forage in the water column. Helgoländer Wissenschaftliche Meeresuntersuchungen 24:292–306.

Domel, A. G., G. Domel, J. C. Weaver, M. Saadat, K. Bertoldi, and G. V Lauder. 2018. Hydrodynamic properties of biomimetic shark skin: effect of denticle size and swimming speed. Bioinspir. Biomim. 13.

Emery, A. R. 1973. Comparative ecology and functional osteology of fourteen species of damselfish (Pisces: Pomacentridae) at Alligator Reef, Florida Keys. Bull. Mar. Sci. 23:649–770.

Felsenstein, J. 1985. Phylogenies and the comparative method. Am. Nat. 125:1–15.

Findley, J. S., and M. T. Findley. 2001. Global, regional, and local patterns in species richness and abundance of butterflyfishes. Ecol. Monogr. 71:69–91.

Frédérich, B., G. Fabri, G. Lepoint, P. Vandewalle, and E. Parmentier. 2009. Trophic niches of thirteen damselfishes (Pomacentridae) at the Grand Récif of Toliara, Madagascar. Ichthyol. Res. 56:10–17.

Frédérich, B., D. Lecchini, and P. Vandewalle. 2010. Evidence of an original scale development during the settlement phase of a coral reef fish (*Acanthurus triostegus*). J. Appl. Ichthyol. 26:176–178.

Frédérich, B., A. Pilet, E. Parmentier, and P. Vandewalle. 2008. Comparative trophic morphology in eight species of damselfishes (Pomacentridae). J. Morphol. 269:254–274.

Frédérich, B., L. Sorenson, F. Santini, G. J. Slater, and M. E. Alfaro. 2013. Iterative ecological radiation and convergence during the evolutionary history of damselfishes (Pomacentridae). Am. Nat. 181:94–113.

Friedman, S. T., S. A. Price, A. S. Hoey, and P. C. Wainwright. 2016. Ecomorphological convergence in planktivorous surgeonfishes. J. Evol. Biol. 29:965–978.

Froese, R., and D. Pauly. 2018. Fishbase.

Fulton, C. ., D. . Bellwood, and P. . Wainwright. 2005. Wave energy and swimming performance shape coral reef fish assemblages. Proc. R. Soc. B Biol. Sci. 272:827–832.

Fulton, C. J., and D. R. Bellwood. 2005. Wave-induced water motion and the functional implications for coral reef fish assemblages. Limnol. Oceanogr. 50:255–264.

Fulton, C. J., D. R. Bellwood, and P. C. Wainwright. 2001. The relationship between swimming ability and habitat use in wrasses (Labridae). Mar. Biol. 139:25–33.

Gluckmann, I., and P. Vandewalle. 1998. Morphofunctional analysis of the feeding apparatus in four pomacentridae species: *Dascyllus aruanus*, *Chromis retrofasciata*, *Chrysiptera biocellata* and *C. unimaculata*. Ital. J. Zool. 65:421–424.

Hansen, T. F. 1997. Stabilizing selection and the comparative analysis of adaptation. Evolution.

51:1341–1351.

Ho, L. S. T., and C. Ane. 2014. A linear-time algorithm for Gaussian and non-Gaussian trait evolution models. Syst. Biol. 63:397–408.

Hobson, E. S. 1991. Trophic relationships of fishes specialized to feed on zooplankters above coral reefs. Pp. 69–95 *in* The ecology of fishes on coral reefs. Academic Press, San Diego.

Hobson, E. S., and J. R. Chess. 1978. Trophic Relationships Among Fishes and plankton in the lagoon at Enewetak Atoll, Marshall Islands. Fish. Bull. 76:133–153.

Huelsenbeck, J. P., R. Nielsen, and J. P. Bollback. 2003. Stochastic Mapping of Morphological Characters. Syst. Biol 52:131–158.

Ibañez, A. L., I. G. Cowx, and P. O'Higgins. 2009. Variation in elasmoid fish scale patterns is informative with regard to taxon and swimming mode. Zool. J. Linn. Soc. 155:834–844.

James Cooper, W., L. L. Smith, and M. W. Westneat. 2009. Exploring the radiation of a diverse reef fish family: Phylogenetics of the damselfishes (Pomacentridae), with new classifications based on molecular analyses of all genera. Mol. Phylogenet. Evol. 52:1–16. Elsevier Inc.

Jimenez, J. 2004. Turbulent flows over rough walls. Annu. Rev. Fluid Mech. 36:173–196.

Johnson, M. K., and E. H. Adelson. 2009. Retrographic sensing for the measurement of surface texture and shape. 2009 IEEE Conf. Comput. Vis. Pattern Recognit. 1070–1077.

Johnson, M. K., F. Cole, A. Raj, and E. H. Adelson. 2011. Microgeometry capture using an elastomeric sensor. ACM SIGGRAPH 2011.

Klein, A., and H. Bleckmann. 2015. Function of lateral line canal morphology. Integr. Zool. 10:111–121.

Kobayasi, H. 1955. Comparative studies of the scales in Japanese freshwater fishes, with special reference to phylogeny and evolution. IV. Particular lepidology of freshwater fishes. I. Suborder Isospondyli (continued). Japanese J. Ichthyol.

Koehl, A. R., J. A. Strother, M. A. Reidenbach, J. R. Koseff, and M. G. Hadfield. 2007. Individual-based model of larval transport to coral reefs in turbulent , wave-driven flow : behavioral responses to dissolved settlement inducer. Mar. Ecol. Prog. Ser. 335:1–18.

Lauder, G. V., D. K. Wainwright, A. G. Domel, J. Weaver, L. Wen, and K. Bertoldi. 2016. Structure, biomimetics, and fluid dynamics of fish skin surfaces. Phys. Rev. Fluids 1.

Lazzaro, X. 1987. A review of planktivorous fish: Their evolution, feeding behaviour, selectivities and impacts. Hydrobiologia 146:97–167.

Lippitsch, E. 1998. Phylogenetic study cichlid fishes in Lake Tanganyika: a lepidological approach. J. Fish Biol. 53:752–766.

Liyan, W. U., J. Zhibin, S. Yuqiu, R. Wentao, N. Shichao, and H. Zhiwu. 2017. Water-trapping and drag-reduction effects of fish *Ctenopharyngodon idellus* scales and their simulations. Sci. China Technol. Sci. 60.

Madin, J. S., K. P. Black, and S. R. Connolly. 2006. Scaling water motion on coral reefs: From regional to organismal scales. Coral Reefs 25:635–644.

Motta, P., M. L. Habegger, A. Lang, R. Hueter, and J. Davis. 2012. Scale morphology and flexibility in the shortfin mako *Isurus oxyrinchus* and the blacktip shark *Carcharhinus limbatus*. J. Morphol. 273:1096–1110.

Odum, H. T., and E. P. Odum. 1955. Trophic structure and productivity of a windward coral reef community on Eniwetok Atoll. Ecol. Monogr. 25:291–320.

Oeffner, J., and G. V Lauder. 2012. The hydrodynamic function of shark skin and two biomimetic applications. J. Exp. Biol. 215:785–95.

Ogden, J. C., P. S. Lobel, P. O. A. Box, S. Croix, and U. S. V. Islands. 1978. The role of herbivorous fishes and urchins in coral reef communities. Environ. Biol. Fishes 3:49–63.

Olivier, D., E. Parmentier, and B. Frédérich. 2016. Insight into biting diversity to capture benthic prey in damselfishes (Pomacentridae). Zool. Anz. 264:47–55.

Ormond, R. F. G., J. M. Roberts, and R.-Q. Jan. 1996. Behavioural differences in microhabitat use by damselfishes (Pomacentridae): impliations for reef fish biodiversity. J. Exp. Mar. Bio. Ecol. 202:85–95.

Pagel, M. 1999. Inferring the historical patterns of biological evolution. Nature 401:877–884.

Parenti, L. R. 1986. The phylogenetic significance of bone types in euteleost fishes. Zool. J. Linn. Soc. 87:37–51.

Pothoff, T., and S. Kelley. 1982. Development of the vertebral column, fins and fin supports, branchiostegal rays, and squamation in the swordfish, *Xiphias gladius*. Fish. Bull. 80:161–186.

Poulet, N., Y. Reyjol, H. Collier, and S. Lek. 2005. Does fish scale morphology allow the identification of populations at a local scale? A case study for rostrum dace *Leuciscus leuciscus burdigalensis* in River Viaur (SW France). Aquat. Sci. 67:122–127.

Price, S. A., J. J. Tavera, T. J. Near, and P. C. Wainwright. 2012. Elevated rates of morphological and functional diversification in reef-dwelling Haemulid fishes. Evolution. 67:417–428.

R Development Core Team. 2016. R: A language and environment for statistical computing. R Foundation for Statistical Computing., Vienna, Austria.

Randall, J. E. n.d. John Randall's fish photographs.

Reidenbach, M. A., S. G. Monismith, J. R. Koseff, G. Yahel, and A. Genin. 2006. Boundary layer turbulence and flow structure over a fringing coral reef. Limnol. Oceanogr. 51:1956–1968.

Revell, L. J. 2012. phytools: An R package for phylogenetic comparative biology (and other things). Methods Ecol. Evol. 3:217–223.

Richards, R. A., and C. Esteves. 1997. Use of scale morphology for discriminating wild stocks of Atlantic striped bass. Trans. Am. Fish. Soc. 126:919–925.

Roberts, C. D. 1993. Comparative morphology of spined scales and their phylogenetic significance in the Teleostei. Bull. Mar. Sci. 52:60–113.

Sagong, W., C. Kim, S. Choi, W.-P. Jeon, and H. Choi. 2008. Does the sailfish skin reduce the skin friction like the shark skin? Phys. Fluids 20:101510-1-101510–10.

Schultz, M. P., and K. A. Flack. 2007. The rough-wall turbulent boundary layer from the hydraulically smooth to the fully rough regime. J. Fluid Mech. 580:381.

Smits, A. J. 2000. A physical introduction to fluid mechanics. 1st ed. John Wiley and Sons Inc., New York, New York, USA.

Sudo, S., K. Tsuyuki, Y. Ito, and T. Ikohagi. 2002. A study on the surface shape of fish scales. Japan Soc. Mech. Eng. 45:1100–1105.

Tang, K. 2001. Phylogenetic relationships among damselfishes (Teleostei: Pomacentridae) as determined by mitochondrial DNA. Copeia 2001:591–601.

Thresher, R. 1983. Environmental Correlates of the Distribution of Planktivorous Fishes in the One Tree Reef Lagoon. Mar. Ecol. Prog. Ser. 10:137–145.

Travers, M. J., I. C. Potter, K. R. Clarke, S. J. Newman, and J. B. Hutchins. 2010. The inshore fish faunas over soft substrates and reefs on the tropical west coast of Australia differ and change with latitude and bioregion. J. Biogeogr. 37:148–169.

Vernerey, F. J., and F. Barthelat. 2014. Skin and scales of teleost fish: Simple structure but high performance and multiple functions. J. Mech. Phys. Solids 68:66–76.

Wainwright, D. K., S. Ingersoll, and G. V Lauder. 2018. Scale diversity in bigeye tuna (*Thunnus obesus*): Fat-filled trabecular scales made of cellular bone. J. Morphol. 1–13.

Wainwright, D. K., and G. V. Lauder. 2018. Mucus matters: the slippery and complex surfaces of fish. Pp. 223–246 *in* S. N. Gorb and E. Gorb, eds. Functional Surfaces in Biology - From the Micro- to Nanoscale. Springer Berlin Heidelberg.

Wainwright, D. K., and G. V. Lauder. 2016. Three-dimensional analysis of scale morphology in bluegill sunfish, *Lepomis macrochirus*. Zoology 119:182–195.

Wainwright, D. K., G. V. Lauder, and J. C. Weaver. 2017. Imaging biological surface topography *in situ* and *in vivo*. Methods Ecol. Evol. 8:1626–1638.

Wainwright, P. C. 2007. Functional versus morphological diversity in macroevolution. Annu. Rev. Ecol. Evol. Syst. 38:381–401.

Wainwright, P. C., and D. R. Bellwood. 2002. Ecomorphology of Feeding in Coral Reef Fishes. Coral Reef Fishes. Dyn. Divers. a Complex Ecosyst. 33–55.

Wainwright, P. C., D. R. Bellwood, and M. W. Westneat. 2002. Ecomorphology of locomotion in labrid fishes. Environ. Biol. Fishes 65:47–62.

Walker, J. A., and M. W. Westneat. 2002. Performance limits of labriform propulsion and correlates with fin shape and motion. J. Exp. Biol. 205:177–187.

Wen, L., J. C. Weaver, P. J. M. Thornycroft, and G. V Lauder. 2015. Hydrodynamic function of biomimetic shark skin: effect of denticle pattern and spacing. Bioinspir. Biomim. 10:066010.

Whitehouse, D. J. 1994. Handbook of Surface Metrology. Institute of Physics Publishing, Philadelphia, USA.

Wu, L., Z. Jiao, Y. Song, C. Liu, H. Wang, and Y. Yan. 2018. Experimental investigations on drag-reduction characteristics of bionic surface with water-trapping microstructures of fish scales. Sci. Rep. 8:1–8.

Yanase, K., and P. Saarenrinne. 2015. Unsteady turbulent boundary layers in swimming rainbow trout. J. Exp. Biol. 218:1373–1385.

Supplementary Information for Chapter 4

Supplemental Table 1. Number of individuals sampled per species

Species	# of individuals
Abudefduf abdominalis	5
Abudefduf bengalensis	5
Abudefduf saxatilis	5
Abudefduf septemfasciatus	5
Abudefduf sexfasciatus	5
Abudefduf sordidus	5
Abudefduf sparoides	5
Abudefduf troschelii	5
Abudefduf whitleyi	5
Amblyglyphidodon curacao	5
Amblyglyphidodon leucogaster	5
Amphiprion allardi	5
Amphiprion bicinctus	5
Amphiprion melanopus	5
Chromis analis	5
Chromis atripectoralis	5
Chromis atripes	5
Chromis caerulea	5
Chromis caudalis	3
Chromis chromis	5
Chromis lepidolepis	5
Chromis limbatus	5
Chromis margaritifer	5
Chromis nitida	5
Chromis notata	5
Chromis ternatensis	5
Chromis vanderbilti	5
Chromis viridis	5
Chromis weberi	5
Chrysiptera brownriggii	5
Chrysiptera glauca	5
Chrysiptera rex	4
Chrysiptera rollandi	3
Dascyllus albisella	5
Dascyllus aruanus	5

Supplemental Table 1 (Continued)

Dascyllus marginatus	5
Dascyllus reticulatus	5
Dascyllus trimaculatus	5
Dischistodus melanotus	3
Dischistodus perspicillatus	4
Lepidozygus tapeinosoma	5
Neoglyphidodon melas	5
Neopomacentrus azysron	5
Neopomacentrus cyanomos	3
Neopomacentrus nemurus	5
Plectroglyphidodon dickii	5
Plectroglyphidodon lacrymatus	5
Pomacentrus amboinensis	5
Pomacentrus bankanensis	5
Pomacentrus brachialis	5
Pomacentrus lepidogenys	5
Pomacentrus moluccensis	5
Pomacentrus pavo	5
Pomacentrus philippinus	5
Pomacentrus trilineatus	5
Pristotis obtusirostris	5
Stegastes albifasciatus	5
Stegastes fasciolatus	5
Stegastes nigricans	5

Supplemental Table 2. Specimen identification numbers and sizes

Species	MCZ#	Standard Length (mm)
Abudefduf abdominalis	14761	148
Abudefduf abdominalis	28960	86
Abudefduf abdominalis	28960	95
Abudefduf abdominalis	14765	94
Abudefduf abdominalis	14765	98
Abudefduf bengalensis	91106	107
Abudefduf bengalensis	91106	109
Abudefduf bengalensis	91106	118
Abudefduf bengalensis	14768	114

Supplemental Table 2 (Continued)

Abudefduf bengalensis	14768	102
Abudefduf saxatilis	42766	96
Abudefduf saxatilis	42766	93
Abudefduf saxatilis	42766	95
Abudefduf saxatilis	42766	96
Abudefduf saxatilis	42766	89
Abudefduf septemfasciatus	29762	141
Abudefduf septemfasciatus	29762	136
Abudefduf septemfasciatus	29762	135
Abudefduf septemfasciatus	14746	123
Abudefduf septemfasciatus	14746	137
Abudefduf sexfasciatus	14758	108
Abudefduf sexfasciatus	69061	103
Abudefduf sexfasciatus	69061	94
Abudefduf sexfasciatus	89970	95
Abudefduf sexfasciatus	30272	93
Abudefduf sordidus	14760	103
Abudefduf sordidus	14760	82
Abudefduf sordidus	14760	98
Abudefduf sordidus	14760	91
Abudefduf sordidus	14760	85
Abudefduf sparoides	6091	100
Abudefduf sparoides	6091	94
Abudefduf sparoides	6091	94
Abudefduf sparoides	6091	89
Abudefduf sparoides	6091	91
Abudefduf troschelii	45599	138
Abudefduf troschelii	45599	150
Abudefduf troschelii	45599	135
Abudefduf troschelii	29683	123
Abudefduf troschelii	29682	124
Abudefduf whitleyi	89980	135
Abudefduf whitleyi	89980	118
Abudefduf whitleyi	69097	129
Abudefduf whitleyi	69097	123
Abudefduf whitleyi	82741	129
Amblyglyphidodon curacao	69095	78
Amblyglyphidodon curacao	69095	76

Supplemental Table 2 (Continued)

Amblyglyphidodon curacao	69095	84
Amblyglyphidodon curacao	69095	75
Amblyglyphidodon curacao	69095	74
Amblyglyphidodon leucogaster	64387	98
Amblyglyphidodon leucogaster	64387	91
Amblyglyphidodon leucogaster	64387	88
Amblyglyphidodon leucogaster	64387	93
Amblyglyphidodon leucogaster	69106	86
Amphiprion allardi	14850	106
Amphiprion allardi	14850	90
Amphiprion allardi	14848	93
Amphiprion allardi	14846	89
Amphiprion allardi	14846	83
Amphiprion bicinctus	50649	80
Amphiprion bicinctus	36777	74
Amphiprion bicinctus	36777	62
Amphiprion bicinctus	36776	65
Amphiprion bicinctus	36776	52
Amphiprion melanopus	33413	64
Amphiprion melanopus	33412	61
Amphiprion melanopus	33186	78
Amphiprion melanopus	27535	69
Amphiprion melanopus	38588	48
Chromis analis	30241	74
Chromis analis	30241	72
Chromis analis	30241	67
Chromis analis	30241	64
Chromis analis	30241	58
Chromis atripectoralis	64475	78
Chromis atripectoralis	64475	68
Chromis atripectoralis	64475	70
Chromis atripectoralis	64475	67
Chromis atripectoralis	69107	74
Chromis atripes	91103	48
Chromis atripes	64442	44
Chromis atripes	64443	54
Chromis atripes	82708	48
Chromis atripes	82708	45

Supplemental Table 2 (Continued)

Chromis caerulea	30230	68
Chromis caerulea	30230	58
Chromis caerulea	30230	54
Chromis caerulea	30230	57
Chromis caerulea	30230	54
Chromis caudalis	162985	43
Chromis caudalis	162985	40
Chromis caudalis	162392	43
Chromis chromis	125554	90
Chromis chromis	125554	91
Chromis chromis	125554	72
Chromis chromis	14660	62
Chromis chromis	14660	64
Chromis lepidolepis	69085	54
Chromis lepidolepis	69085	52
Chromis lepidolepis	69085	53
Chromis lepidolepis	69085	51
Chromis lepidolepis	69085	53
Chromis limbatus	96183	102
Chromis limbatus	96183	94
Chromis limbatus	96183	91
Chromis limbatus	96183	94
Chromis limbatus	96183	92
Chromis margaritifer	64325	54
Chromis margaritifer	64325	53
Chromis margaritifer	64325	53
Chromis margaritifer	64325	55
Chromis margaritifer	64325	52
Chromis nitida	170620	63
Chromis nitida	170620	54
Chromis nitida	170620	49
Chromis nitida	170620	46
Chromis nitida	36853	47
Chromis notata	28996	70
Chromis notata	28996	65
Chromis notata	28996	74
Chromis notata	28996	73
Chromis notata	28996	55

Supplemental Table 2 (Continued)

Chromis ternatensis	80359	59
Chromis ternatensis	80359	60
Chromis ternatensis	80359	60
Chromis ternatensis	80359	57
Chromis ternatensis	80359	56
Chromis vanderbilti	69067	45
Chromis vanderbilti	69067	44
Chromis vanderbilti	69067	42
Chromis vanderbilti	69067	42
Chromis vanderbilti	69067	39
Chromis viridis	162645	39
Chromis viridis	162645	44
Chromis viridis	162645	43
Chromis viridis	162645	38
Chromis viridis	162645	41
Chromis weberi	64328	80
Chromis weberi	64328	82
Chromis weberi	64328	79
Chromis weberi	64328	78
Chromis weberi	64328	79
Chrysiptera brownriggii	30224	50
Chrysiptera brownriggii	30224	51
Chrysiptera brownriggii	30224	49
Chrysiptera brownriggii	30224	49
Chrysiptera brownriggii	30224	48
Chrysiptera glauca	30239	63
Chrysiptera glauca	30239	60
Chrysiptera glauca	30239	56
Chrysiptera glauca	30239	56
Chrysiptera glauca	30239	63
Chrysiptera rex	64440	37
Chrysiptera rex	90613	36
Chrysiptera rex	90613	34
Chrysiptera rex	90613	28
Chrysiptera rollandi	90624	42
Chrysiptera rollandi	90624	35
Chrysiptera rollandi	90624	30
Dascyllus albisella	14835	63

Supplemental Table 2 (Continued)

Dascyllus albisella	51671	83
Dascyllus albisella	51671	89
Dascyllus albisella	51671	87
Dascyllus albisella	51671	82
Dascyllus aruanus	63139	51
Dascyllus aruanus	14827	50
Dascyllus aruanus	14827	50
Dascyllus aruanus	14831	43
Dascyllus aruanus	14831	41
Dascyllus marginatus	36854	47
Dascyllus marginatus	36854	34
Dascyllus marginatus	36854	33
Dascyllus marginatus	14844	40
Dascyllus marginatus	26420	38
Dascyllus reticulatus	89972	47
Dascyllus reticulatus	89972	41
Dascyllus reticulatus	89972	42
Dascyllus reticulatus	36764	40
Dascyllus reticulatus	36764	40
Dascyllus trimaculatus	82742	86
Dascyllus trimaculatus	82742	76
Dascyllus trimaculatus	82742	115
Dascyllus trimaculatus	82742	85
Dascyllus trimaculatus	82742	94
Dischistodus melanotus	36786	100
Dischistodus melanotus	36786	38
Dischistodus melanotus	36786	32
Dischistodus perspicillatus	36789	89
Dischistodus perspicillatus	36789	82
Dischistodus perspicillatus	36789	71
Dischistodus perspicillatus	36789	66
Lepidozygus tapeinosoma	162569	54
Lepidozygus tapeinosoma	162569	48
Lepidozygus tapeinosoma	162569	44
Lepidozygus tapeinosoma	162569	43
Lepidozygus tapeinosoma	162568	55
Neoglyphidodon melas	82740	133
Neoglyphidodon melas	82740	112

Supplemental Table 2 (Continued)

Neoglyphidodon melas	82739	117
Neoglyphidodon melas	82739	123
Neoglyphidodon melas	36770	43
Neopomacentrus azysron	64469	54
Neopomacentrus azysron	64469	50
Neopomacentrus azysron	64469	47
Neopomacentrus azysron	64469	49
Neopomacentrus azysron	64469	45
Neopomacentrus cyanomos	41737	53
Neopomacentrus cyanomos	54314	58
Neopomacentrus cyanomos	52955	50
Neopomacentrus nemurus	64389	37
Neopomacentrus nemurus	64389	39
Neopomacentrus nemurus	64389	39
Neopomacentrus nemurus	64389	36
Neopomacentrus nemurus	64389	36
Plectroglyphidodon dickii	69093	76
Plectroglyphidodon dickii	69093	71
Plectroglyphidodon dickii	69093	74
Plectroglyphidodon dickii	91107	74
Plectroglyphidodon dickii	91107	72
Plectroglyphidodon lacrymatus	64337	81
Plectroglyphidodon lacrymatus	64337	83
Plectroglyphidodon lacrymatus	64337	79
Plectroglyphidodon lacrymatus	64337	68
Plectroglyphidodon lacrymatus	64337	72
Pomacentrus amboinensis	89988	50
Pomacentrus amboinensis	89988	53
Pomacentrus amboinensis	89988	49
Pomacentrus amboinensis	89988	48
Pomacentrus amboinensis	89988	49
Pomacentrus bankanensis	69091	63
Pomacentrus bankanensis	69091	62
Pomacentrus bankanensis	69091	64
Pomacentrus bankanensis	69091	61
Pomacentrus bankanensis	69091	60
Pomacentrus brachialis	82714	67
Pomacentrus brachialis	38597	70

Supplemental Table 2 (Continued)

Pomacentrus brachialis	69087	68
Pomacentrus brachialis	69087	62
Pomacentrus brachialis	69087	58
Pomacentrus lepidogenys	82711	62
Pomacentrus lepidogenys	82711	62
Pomacentrus lepidogenys	82711	60
Pomacentrus lepidogenys	82711	58
Pomacentrus lepidogenys	82711	59
Pomacentrus moluccensis	82716	51
Pomacentrus moluccensis	82716	47
Pomacentrus moluccensis	82716	53
Pomacentrus moluccensis	82716	48
Pomacentrus moluccensis	90628	50
Pomacentrus pavo	162668	39
Pomacentrus pavo	162668	37
Pomacentrus pavo	30215	38
Pomacentrus pavo	30215	35
Pomacentrus pavo	30215	33
Pomacentrus philippinus	82718	65
Pomacentrus philippinus	82718	64
Pomacentrus philippinus	69082	67
Pomacentrus philippinus	69082	68
Pomacentrus philippinus	69082	63
Pomacentrus trilineatus	14685	77
Pomacentrus trilineatus	3695	52
Pomacentrus trilineatus	14683	42
Pomacentrus trilineatus	14683	40
Pomacentrus trilineatus	14683	32
Pristotis obtusirostris	54084	74
Pristotis obtusirostris	54084	79
Pristotis obtusirostris	54084	78
Pristotis obtusirostris	54084	77
Pristotis obtusirostris	54084	73
Stegastes albifasciatus	63148	94
Stegastes albifasciatus	63148	90
Stegastes albifasciatus	63148	89
Stegastes albifasciatus	63148	81
Stegastes albifasciatus	63148	77

Supplemental Table 2 (Continued)

Stegastes fasciolatus	89983	91
Stegastes fasciolatus	89983	88
Stegastes fasciolatus	89983	86
Stegastes fasciolatus	89983	83
Stegastes fasciolatus	89983	90
Stegastes nigricans	162633	77
Stegastes nigricans	162633	73
Stegastes nigricans	162633	72
Stegastes nigricans	162633	64
Stegastes nigricans	162633	64

Simulations to examine error rates of choosing multi-peak models:

Repeating our model-fitting on species data simulated under single-rate Brownian motion evolution led to results that were consistent with the findings of Boettiger et al. (2012) and Cooper et al. (2016). Multi-peak OU models do often received substantial empirical support even when the generating model is Brownian motion. However, the level of support—as reflected by mean wAICc and the proportion of reconstruction for which multi-peak OU was the preferred model—was rarely as high as the empirical support we found for our data. For roughness, only 1% of simulated datasets showed multi-optima model support equal to or higher than those reported in Table 1. For ctenii length, 4% of simulated datasets show mean wAICc values for multi-peak models greater than or equal to our results (Table1) and 8% show percent preferred values at or higher than our results. Ctenii length also shows support for the OU1 model, and only 1% of simulated datasets have model selection values for the OU1 model at or higher than our results (Table 1) and 2% of simulated datasets show percent preferred values for the OU1 model at or higher than our results (Table 1: 56% preferred for OU1). Altogether these analyses reveal robust support for our evolutionary model selection results.

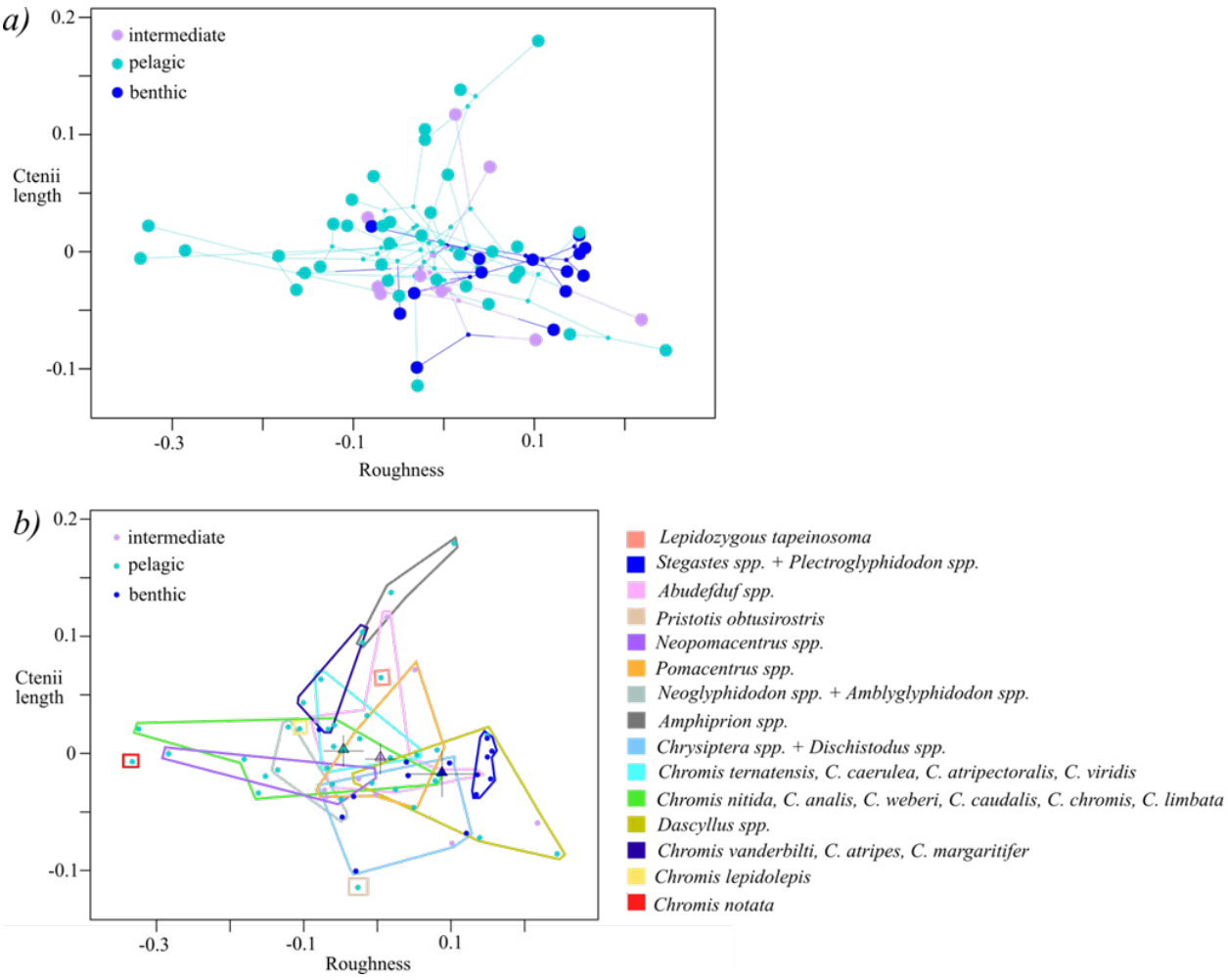

Supplemental Figure 1. Phylomorphospaces of roughness versus ctenii length. a) phylomorphospace with stochastic map from Figure 3. b) Same as Figure 4 but with clades outlined in colored polygons.

Results for scales sampled from the posterior body region:

Scales from the posterior body region showed evolutionary patterns similar to those of the midbody region. Supplemental Tables 3, 4, 6, and 8 summarize model selection and parameter estimation for morphological evolution of posterior scales. As in the midbody results, the best fitting models for the evolution of roughness on posterior scales are the three OUM models. These models have the lowest dAICc 99% of the time (OU3M: 0%, OU2M-pelagic: 47%, OU2M-benthic: 52%) as well as a combined wAICc vale of 0.86 (OU3M: 0.14, OU2M-pelagic: 0.33, OU2M-benthic: 0.39) indicating strong support for multi-peak models that is robust across reconstructions and trees.

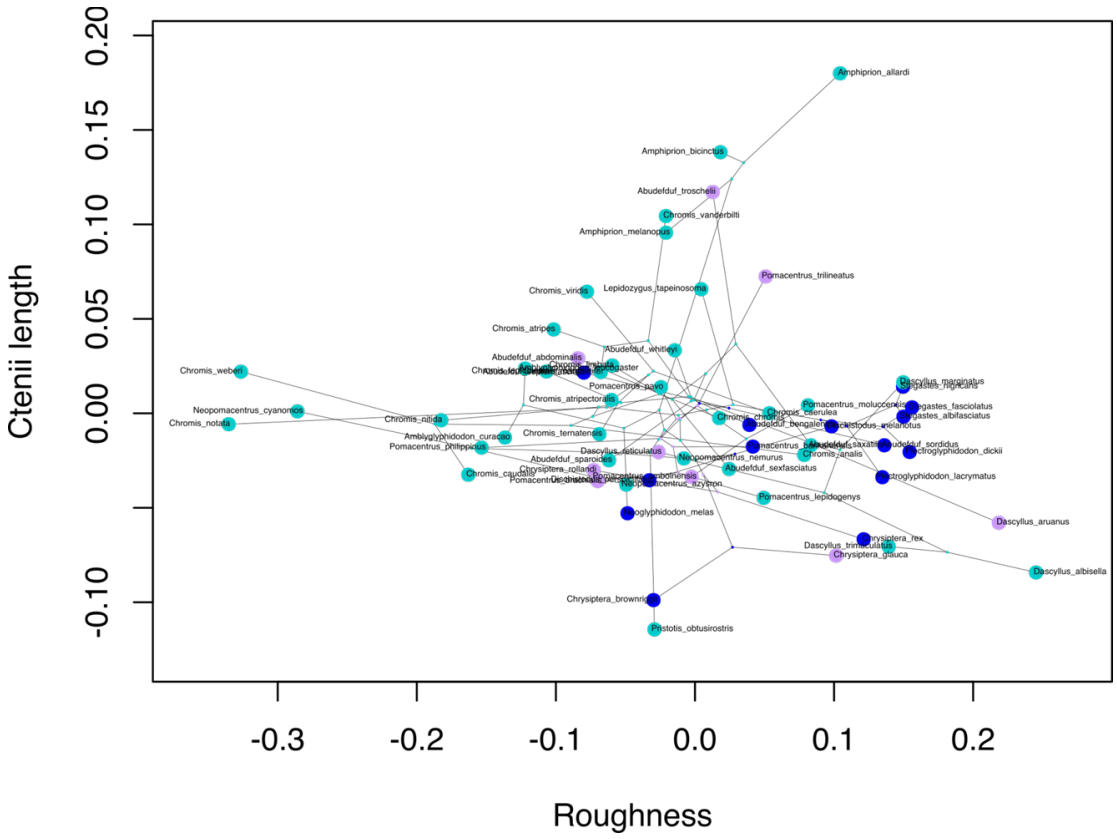

Supplemental Figure 2. Roughness versus ctenii length phylomorphospace with species labels added.

Results are mixed for the evolution of ctenii length, with the OU1 model having the lowest dAICc in 98% of the 500 model comparisons. However, wAICc values show mixed support between the OU1 model and the three multi-peak models, with wAICc for OU1 at 0.50 and wAICc for the combined multi-peak models also at 0.50 (OU3M: 0.08, OU2M-pelagic: 0.18, and OU2M-benthic: 0.24).

The best fitting model for scale aspect ratio is the BM model, although there is some weak support for the three multi-peak models (Supplemental Table 4). For scale aspect ratio, the BM model has a wAICc value of 0.44 and has 76% of the models with the lowest dAICc. The best fitting model for percentage of ctenii coverage is the OU1 model, however there is some mixed support for the three multi-peak models (Supplemental Table 4). Specifically, the OU1 model has a wAICc value of

0.41 and has 84.6% of the models with the lowest dAICc.

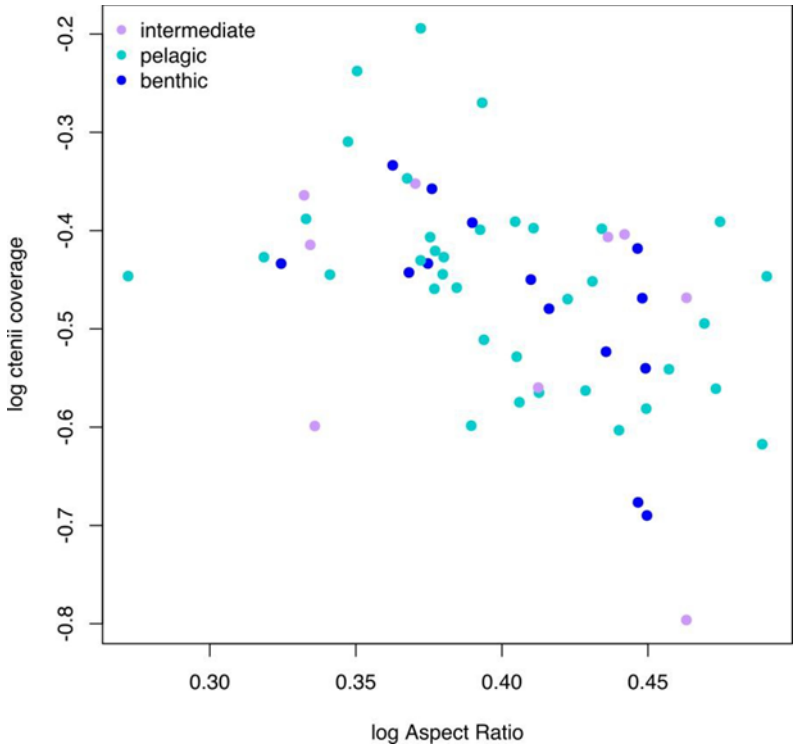

Supplemental Figure 3. Midbody scale aspect ratio vs ctenii coverage. Both of these variables show high support for either the BM or OU single-optima models.

Discussion of posterior scale evolution:

The results for the posterior region of the body are largely similar to results from the midbody region of the body. Small differences include having less support for the three multi-peak models (OU3M, OU2M-pelagic, OU2M-benthic) for the ctenii length variable, so that model support is evenly split between the OU1 model and the aggregate support of the three multi-peak models. Nevertheless, because the data and model fitting for the posterior region is similar to the midbody region, our conclusions are similar. The pelagic ecology's model weighted optimum has a lower roughness than the benthic ecology (with the intermediate ecology in between the two). Like the midbody results, this supports the idea that a smoother surface may be advantageous in planktivorous species that tend to

Supplemental Table 3. Model weighted optima from both midbody and posterior variables. Variables names given with a '.resid 'indicate this variable was size corrected. AR is aspect ratio, coverage is ctenii coverage, Sq is roughness. θ are trait optima. Standard errors are indicated with a 'se.' before the column name. α is also called the rate of adaptation and σ^2 is the rate of stochastic evolution. Phyl.half-life is phylogenetic half-life and represents half of the time it takes for a trait to evolve towards an optimum (units of branch length). Posterior variables are given below midbody ones and are labelled with 'Post'.

Variable	θ int	θ pel	θ ben	se. θ int	se. θ pel	se. θ ben	α	se. α	phyl half life	σ^2	se.σ^2
logAR	0.2760	0.3944	0.4084	0.0178	0.0165	0.0200	1.0760	0.5338	0.6442	0.0059	0.3982
logcoverage	-0.3748	-0.4654	-0.4905	0.0385	0.0415	0.0460	0.1055	39.8576	6.5682	0.0119	0.3037
logcteniilength.resid	-0.0035	0.0033	-0.0163	0.0075	0.0099	0.0144	4.2708	0.4243	0.1623	0.0234	0.3971
logSq.resid	0.0038	-0.0467	0.0879	0.0145	0.0199	0.0334	8.0888	0.5624	0.0857	0.1948	0.5534
PostlogAR	0.2343	0.3860	0.4197	0.0220	0.0264	0.0312	0.000006	407.9123	123546.0	0.0038	0.2131
Postlogcoverage	-0.2408	-0.4057	-0.4277	0.0182	0.0201	0.0265	1.7676	0.4283	0.3921	0.0187	0.3632
Postlogcteniilength.resid	-0.0038	-0.0003	-0.0084	0.0081	0.0106	0.0146	4.0936	0.3908	0.1693	0.0267	0.3694
PostlogSq.resid	0.0054	-0.0113	0.0550	0.0097	0.0169	0.0273	8.9327	0.6292	0.0776	0.1639	0.6173

swim away from structure, experiencing mostly laminar flow during feeding. Species in the benthic ecology are likely to be swimming near or within structure while maneuvering, thus experiencing more turbulent and unsteady flows. In turbulent flows, roughness in the form of organized surface features can decrease drag (i.e. dimples on golf balls) and while experimental testing would be needed to prove such a mechanism, our results could be considered evidence to support this hypothesis.

Caveats:

Although our results support the hypothesis that damselfish scales have been shaped by the selective demands of feeding habitat, we recognize several limitations to the inferences that can be drawn from our study.

First, our selection of multi-peak OU models as best-fit is relative to the set of models we

Supplemental Table 4. Posterior model supports showing the percent of models with the lowest dAICc values and wAICc values.

	wAICc					% with lowest dAICc				
	BM	OU	OU3M	OU2M pelagic	OU2M benthic	BM	OU	OU3M	OU2M pelagic	OU2M benthic
Aspect ratio	**0.44**	0.14	0.10	0.10	0.22	**76**	0	0.6	0.4	23
Percent ctenii coverage	0.05	**0.41**	0.10	0.18	0.25	0	**84.6**	1.8	0	13.6
ctenii length (size corr)	0.00	**0.50**	0.08	0.18	0.24	0	**97.6**	0	0	2.4
roughness (size corr)	0.00	0.15	**0.14**	**0.33**	**0.39**	0	1	**0.2**	**46.8**	**52**

evaluated, and so unconsidered models that incorporate additional selective factors or constraints could potentially better explain patterns of scale diversity among damselfishes. In fact, while there is a clear association between evolution of feeding habitat and scale morphology, we strongly suspect that scale evolution is more complex than our best-fit multi-peak models. As we describe above, the capacity to respond to habitat-imposed selection may vary among species because of differences in genetics, functional tradeoffs, or environmental conditions (Hansen 1997). At this point, we cannot say much about the possible roles of other drivers of scale evolution. We believe, however, that our analysis is a reasonable and productive first step in identifying adaptive scale evolution because the pelagic-benthic feeding gradient is a prominent axis of damselfish diversity (Cooper and Westneat 2009; Frédérich et al. 2013), feeding habitats are associated with different flow regimes (Wainwright et al. 2002; Fulton et al. 2005; Madin et al. 2006; Johansen et al. 2007; Aguilar-Medrano et al. 2016) and scales have been hypothesized to have important functional consequences for swimming performance (Burdak 1986; Choi et al. 2012; Lauder et al. 2016; Wainwright and Lauder 2016; Liyan et al. 2017; Wainwright and Lauder 2018).

We also acknowledge that the ecological categories we examined pertain to feeding habitats and uncertainty remains regarding the selective importance of this variable on locomotor performance. We argue that because damselfish swim while they feed and spend considerable time feeding, the demands of effective foraging are likely to be important in shaping locomotor performance. However,

Supplemental Table 5. Midbody 95% confidence interval of dAICc from model fitting. Values of zero indicate strong support. Sq is roughness; variables that were size corrected are labelled with ".resid".

	BM1_AICc	OU1_AICc	OUM_AICc	OUMpel_AICc	OUMben_AICc
logAR	(0, 3.51)	(0, 2.99)	(0, 4.71)	(0.42, 3.30)	(0, 2.71)
logcoverage	(0, 0)	(1.90, 2.22)	(1.41, 6.65)	(2.36, 4.50)	(0.46, 4.39)
logcteniilength.resid	(11.12, 19.96)	(0, 2.36)	(1.21, 4.25)	(0, 2.97)	(0, 2.07)
logSq.resid	(19.14, 34)	(5.46, 11.19)	(0, 3.42)	(0, 4.23)	(0, 1.88)

Supplemental Table 6. Posterior 95% confidence interval of dAICc from model fitting. Values of zero indicate strong support. Sq is roughness; variables that were size corrected are labelled with ".resid".

	BM1_AICc	OU1_AICc	OU3M_AICc	OU2Mpel_AICc	OU2Mben_AICc
logAR	(0, 3.07)	(2.22, 5.29)	(0.75, 6.50)	(1.13, 4.53)	(0, 4.47)
logcoverage	(2.85, 6.71)	(0, 1.07)	(0.91, 4.58)	(0.80, 2.30)	(0, 2.26)
logcteniilength.resid	(9.8, 25.84)	(0, 0)	(2.42, 4.63)	(1, 2.3)	(0.03, 2.29)
logSq.resid	(15.59, 29.45)	(0.45, 5.75)	(1.43, 3.99)	(0, 4.37)	(0, 1.9)

damselfish do more than feed, and other activities may bring them to habitats beyond their feeding grounds where they might experience different, potentially contrasting demands on swimming performance. Moreover, it is difficult to determine the exact flow conditions a fish experiences within a habitat. The high spatial and temporal variability of flows on coral reefs (Odum and Odum 1955; Wainwright et al. 2002; Fulton and Bellwood 2005; Reidenbach et al. 2006) make it very challenging to assign flow characteristics to the microhabitats where species occur (Bellwood and Wainwright 2001; Fulton et al. 2001; Johansen and Jones 2013). We therefore recognize ambiguity in the relationship between feeding habitat, flow regime, and selection on swimming performance, but we expect any weakness in these links to lessen the association between feeding habitat and scale evolution rather than cause a spurious one. In spite of likely variation in the exact flow conditions experienced

Supplemental Table 7. Midbody 95% confidence interval for log likelihood and AIC scores. Sq is roughness; variables that were size corrected are labelled with ".resid".

	BM1_loglik	BM1_AICc	OU1_loglik	OU1_AICc	OU3M_loglik	OU3M_AICc	OU2Mpel_loglik	OU2Mpel_AICc	OU2Mben_loglik	OU2Mben_AICc
AR	(98.92, 103.22)	(-202.2, -193.6)	(100.51, 103.92)	(-201.4,-194.6)	(101.09, 106.15)	(-201.2, -191.1)	(100.78, 104.51)	(-200.3, -192.8)	(100.92, 105.30)	(-201.9, -193.1)
cteniicoverage	(67.90, 69.4)	(-134,7, -131.6)	(67.94, 69.49)	(-132.5, -129.4)	(68.50, 71.51)	(-131.9, -125.9)	(68.14, 70.20)	(-131.7, -127.5)	(68.38, 71.00)	(-133.3, -128.0)
cteniilength.resid	(81.26, 87.16)	(-170.11, -158.31)	(91.69, 94.31)	(-182.18, -176.95)	(92.39, 96.09)	(-181.06, -173.66)	(92.05, 95.53)	(-182.33, -175.36)	(92.32, 95.65)	(-182.56, -175.89)
Sq.resid	(28.45, 36.08)	(-67.94, -52.68)	(41.89, 43.53)	(-80.62, -77.35)	(46.9, 50.03)	(-88.93, -82.66)	(46.01, 48.55)	(-88.35, -83.28)	(46.22, 49.53)	(-90.32, -83.7)

Supplemental Table 8. Posterior 95% confidence interval for log likelihood and AIC scores. Sq is roughness; variables that were size corrected are labelled with ".resid".

	BM1_loglik	BM1_AICc	OU1_loglik	OU1_AICc	OU3M_loglik	OU3M_AICc	OU2Mpel_loglik	OU2Mpel_AICc	OU2Mben_loglik	OU2Mben_AICc
AR	(101.19, 103.89)	(-203.56, -198.17)	(101.19, 103.89)	(-201.34, -195.95)	(102.19, 106.79)	(-202.44, -193.26)	(101.5, 105.35)	(-201.95, -194.27)	(101.95, 106.58)	(-204.42, -195.17)
coverage	(70.23, 73.76)	(-143.3, -136.25)	(74.22, 76.45)	(-146.46, -142.01)	(74.85, 78.00)	(-144.88, -138.56)	(74.57, 76.94)	(-145.15, -140.4)	(74.74, 77.49)	(-146.23, 140.74)
cteniilength.resid	(72.66, 83.74)	(-163.27, -141.1)	(86.41, 90.08)	(-173.72, -166.39)	(87.13, 90.61)	(-170.09, -163.14)	(86.6, 90.32)	(-171.89, -164.45)	(87.01, 90.56)	(-172.39, -165.28)
Sq.resid	(38.01, 46.09)	(-87.96, -71.8)	(52.45, 54.21)	(-101.99, -98.47)	(54.22, 57.72)	(-104.31, -97.3)	(53.86, 56.89)	(-105.04, -98.98)	(54.03, 57.32)	(-105.91, -99.32)

by species that share a feeding habitat, we document a general trend for pelagic and benthic feeding damselfish to evolve different scale morphology. Nevertheless, variable flow environments within a feeding habitat or in habitats used during other behaviors may explain the substantial overlap in scale characteristics between some pelagic and benthic damselfishes (Fig. 4).

5

Mucus Matters: The Slippery and Complex Surfaces of Fish

Reprinted from:

Wainwright, D. K., & Lauder, G. V. (2018) Mucus matters: the slippery and complex surfaces of fish. In S. N. Gorb & E. Gorb (Eds.), *Functional Surfaces in Biology - From the Micro- to Nanoscale* (1st ed., pp. 223–246). Springer Berlin Heidelberg.

Chapter 10
Mucus Matters: The Slippery and Complex Surfaces of Fish

Dylan K. Wainwright and George V. Lauder

Abstract Teleost scales are extremely diverse in morphology, with different categories (cycloid, crenate, spinoid, ctenoid) once used to define major groups of fish. We describe these different classical categories of scales and discuss the structure and potential function of small features of scale morphology such as spines, ctenii, radii, and circuli. Modern techniques now make analysis of scale morphology using three-dimensional quantitative data possible. This ability is crucial because many of the hydrodynamic and protective hypotheses concerning the function of scales are dependent on three-dimensional structure. We discuss different techniques to investigate and image the structure of fish scales and skin, and we highlight gel-based surface profilometry as a new valuable tool for studying fish skin. In addition to bony scales, fish skin is also covered by an epidermis that secretes mucus that can coat the exterior of scales. Fish scales are often studied in isolation with the epidermis removed; here we present topographic, three-dimensional, analyses of fish skin surfaces from seven species with the mucus, epidermis, and relative positions of scales intact. We compare these images qualitatively and quantitatively to the same individuals with the epidermis and mucus removed to show a previously unexplored axis of diversity in fish: how mucus and epidermis interact with scale morphology to create surface texture. The three-dimensional structure of fish skin has important implications for hydrodynamic function during locomotion, but this remains a largely unexplored area.

10.1 Introduction – Fish Surfaces

Fish skin is generally similar to the skin of other vertebrates, with a few important distinctions. Like other vertebrates, fish have an epidermis as their outermost dermal layer and a dermis beneath that, but fish skin is distinguished by the presence of two

D. K. Wainwright (✉) · G. V. Lauder
Department of Organismic and Evolutionary Biology, Harvard University,
Cambridge, MA, USA
e-mail: dylanwainwright@fas.harvard.edu

important features – goblet cells full of mucus in the epidermis, and bony scales embedded in the dermis and epidermis (Hawkes 1974; Fast et al. 2002; Zaccone et al. 2001). Other vertebrates may have one of these features, such as bony scales in crocodiles and goblet cells in human mucus membranes, but never both together as in fishes. In teleosts, bony scales appear as overlapping, layered-bone plates embedded in the skin. In this chapter, we will focus on fish surfaces composed of elasmoid scales, thereby excluding both the ganoid scales of basal fish groups (gars and polypterids) and the placoid scales of sharks and rays (Meyer and Seegers 2012; Motta et al. 2012).

Scales likely serve a number of functions in fishes, including physical protection from predators and parasites, prevention of surface fouling, and modification of flow during swimming. However, scales are only a part of a fish's surface, and in fact, scales are not even the outermost part of the skin – instead, an epidermis covers scales and secretes a layer of mucus that covers fish (Fig. 10.1) (Whitear 1970). This layer of epidermis and mucus covers scales and is necessary for scale growth, regeneration, and maintenance (Bereiter-Hahn and Zylberberg 1993; Shephard 1994). The mucus layer is also known to be important for immune function in fishes (Shephard 1994; Rakers et al. 2010; Esteban 2012; Xu et al. 2013), and some authors have also suggested that mucus plays a role in modifying flow conditions around fish to increase swimming efficiency (Rosen and Cornford 1971; Daniel 1981; Bernadsky et al. 1993).

Fig. 10.1 Histological transverse cross-section of skin from a brook trout (*Salvelinus fontinalis*) showing epidermis with goblet cells, scales in scale pockets, and the underlying dermis and muscle. Stained with hematoxylin and eosin. Anterior is coming out of the page, posterior is going into the page. *d* dermis, *e* epidermis, *g* goblet cell, *ll* lateral line canal, *m* muscle, *s* scale. Scale bar: 100 μm

Together, the mucus layer, epidermis, and scales of a fish create the outermost barrier between a fish's body and the external fluid (Fig. 10.1). These tissues also combine to create the topographic texture of a fish's skin. For example, scales overlap in a pattern where the posterior of each scale is inclined towards the outside of the fish, with epidermis and mucus covering the surface of the scales. Scales, epidermis, and mucus interact to create surface topography on the outside of the fish, but the degree to which each of these tissues contributes to topography is unclear. Additionally, structures such as spines, ctenii, and circuli occur on fish scales and create texture on fish (these structures are further discussed below). Fish skin texture in various species has been hypothesized to create favorable flow conditions for swimming by reducing drag, increasing thrust, or increasing efficiency (Bone 1972; Burdak 1986; Liyan et al. 2017); however, these ideas have yet to be tested in a rigorous way. Many ideas about hydrodynamic functions of scales concern how structures on scales, such as spines, can influence the flow around the body of a fish in a favorable way (Burdak 1986; Sagong et al. 2008; Wainwright and Lauder 2016), but these ideas tend to neglect how the epidermis and mucus could also change the topography that the water encounters during swimming.

In this chapter, we will discuss both the diversity of fish scales and how different scale morphologies interact with epidermis and mucus. We will show how mucus changes the topography of fish scale surfaces in a variety of species and elaborate on what that might mean for hypotheses of fish scale function.

10.2 Fish Scales – Complex Surfaces

10.2.1 Scale Types: A Classification

Elasmoid scales of bony fish have three layers (external to internal: limiting layer, external layer, and elasmodine), but the bulk of their structure is elasmodine, a plywood-like structure of collagen fibers that mineralizes into acellular bone with development (Huysseune and Sire 1998; Sire and Huysseune 2003; Meunier 2011). Elasmoid scales are embedded in the epidermis of fishes and are often arranged in an overlapping pattern over the body and sometimes fins. Scales are sheathed in scale pockets, which are connective tissue wrappings that either completely or partially surround the scale (Fig. 10.1) (Bereiter-Hahn and Zylberberg 1993; Sire and Akimenko 2004). Scales grow with the fish – bony fish will replace scales if they fall off or are damaged, but fish do not typically increase the number of scales with growth (Taylor 1916; Thomson 1956; Casselman 1990). Although there is tremendous size diversity in fish scales, scales are routinely 2–15 mm in length, 0.1–2 mm in thickness, and features such as spines and ridges may be tens to hundreds of microns (many exceptions exist to these estimates) (Taylor 1916; Roberts 1993; Wainwright and Lauder 2016; Bergman et al. 2017; Wainwright et al. 2017).

Elasmoid scales of most teleosts have been categorized into different types according to their morphology, with the four main types being cycloid, crenate,

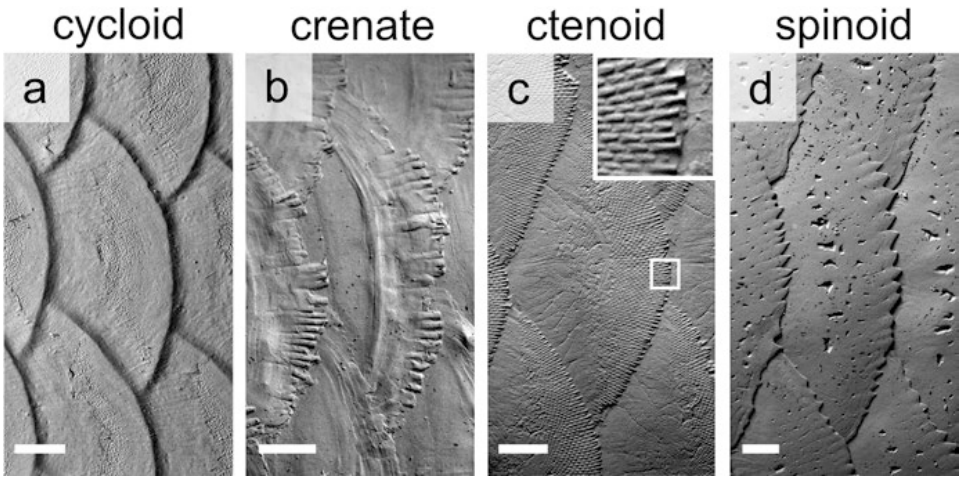

Fig. 10.2 Scale types of teleost fishes illustrated using gel-based profilometry. (**a**) Cycloid scales of bonefish (*Albula vulpes*) with smooth edges. (**b**) Crenate scales of Chacunda gizzard shad (*Anodontostoma chacunda*) with flat, finger-like projections at the posterior edge. (**c**) Ctenoid scales of blackspot sergeant (*Abudefduf sordidus*) with small interlocking spines, enlarged in inset. (**d**) Spinoid scales of sabre squirrelfish (*Sargocentron spiniferum*) with large, flattened, continuous spines. Scale bars: 1 mm

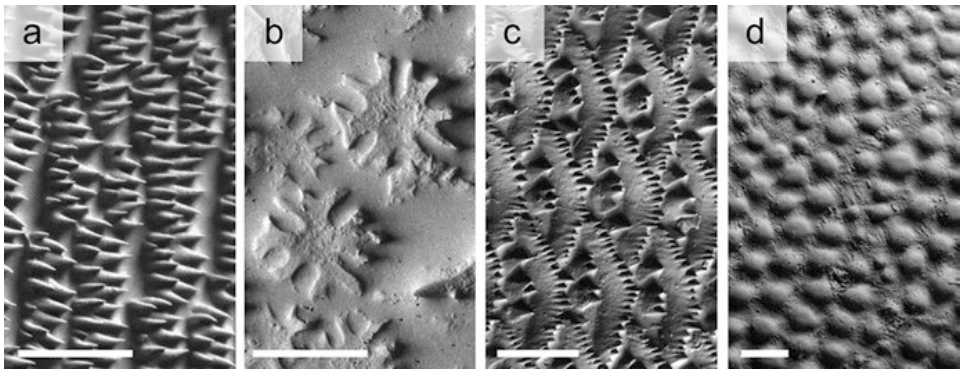

Fig. 10.3 Diversity of fish scales illustrated with gel-based profilometry. (**a**) Complex spiny scales of Moorish idol (*Zanclus cornutus*). (**b**) Oak-leaf-shaped scales of louvar (*Luvarus imperialis*). (**c**) Spiny scales of deepbody boarfish (*Antigonia capros*). (**d**) Interlocking plate-like bumpy scales of scrawled cowfish (*Acanthostracion quadricornis*). Scale bars: 1 mm

ctenoid, and spinoid (Roberts 1993). Figure 10.2 illustrates these four different categories of scales with typical examples of each category. Cycloid scales have smooth posterior edges, crenate scales have edges with flat, blunt projections, ctenoid scales have posterior edges made of separate ossified interlocking spines called ctenii (plural; Fig. 10.2c inset), and spinoid scales have spines that are continuous with the ossification of the scale itself (Roberts 1993).

As is often the case in biology, these classifications hold for large portions of diversity, but there are many exceptions. In Fig. 10.3, we show images of four dif-

ferent fish skin surfaces that illustrate some of the challenges to scale classification. In Fig. 10.3a, we show scales of the Moorish idol (*Zanclus cornuta*) that have many densely-packed spines. We would classify these scales as spinoid because they have spines that are continuous with the ossification of the scale plate themselves, but these look markedly different from the spinoid scales in Fig. 10.2d. Similarly, Fig. 10.3c shows spinoid scales from the boarfish (*Antigonia capros*), which have both spines on the posterior margin of the scale and on the body of the scale. Figure 10.3a, c illustrate how diverse spinoid scales are – so diverse that the classification of spinoid seems to be too broad to have much meaning. C. Roberts (Roberts 1993) remedied this by further classifying scales into subtypes within the different categories, especially in the case of spinoid and ctenoid scales. However, this author also acknowledged how little we know about the evolution and development of different scale types – both of which are relevant to making meaningful categorizations. We also know little about how scale morphology correlates with function, which would inform categorization based not only on morphology, but also on the relationship between morphology and function.

Figure 10.3b shows the bizarre, leaf-shaped scales of a juvenile louvar (*Luvaris imperialis*). These louvar scales are so modified that they do not fit in any current category of scale classification – they are vaguely oak leaf-shaped and sit atop pedestals connected to the rest of the body of the scale. In Fig. 10.3d, the thickened and sutured scales in the scrawled cowfish (*Acanthostracion quadricornis*) are also modified to the point that they defy classification into normal categories and as such, they are often referred to as scutes or dermal plates instead of scales (Besseau and Bouligand 1998). The four species in Fig. 10.3 illustrate a small part of the vast diversity of scales found in different species of fish. It is important that we continue to explore scale diversity in both qualitative and quantitative studies to gain a better understanding of the morphological disparity of scales, the evolutionary patterns of scale morphology, and scale structure-function relationships.

10.2.2 Hypotheses for Functional Diversity in Scales

Although scale morphology is diverse, there are some structural features that are common to most scaled species. We have briefly mentioned some of the microstructures on fish scales above, such as the interlocking ctenii of ctenoid scales and the spines of spinoid scales, but there are other relevant structures like circuli and radii that also occur on many scales. Below we discuss these structural features and potential functions for them.

Circuli are concentric circles usually starting from the scale's center (called the focus), and that represent periods of growth of a scale (similar to tree rings) (Fig. 10.4). They are raised above the surface of the scale and are present on the external surface of scales, facing the water. In many studies, circuli are used to estimate the age of fish, although not by a direct count (Batts 1964; Beardsley 1967; Hill et al. 1989); instead some circuli (called annuli) are closer together and represent

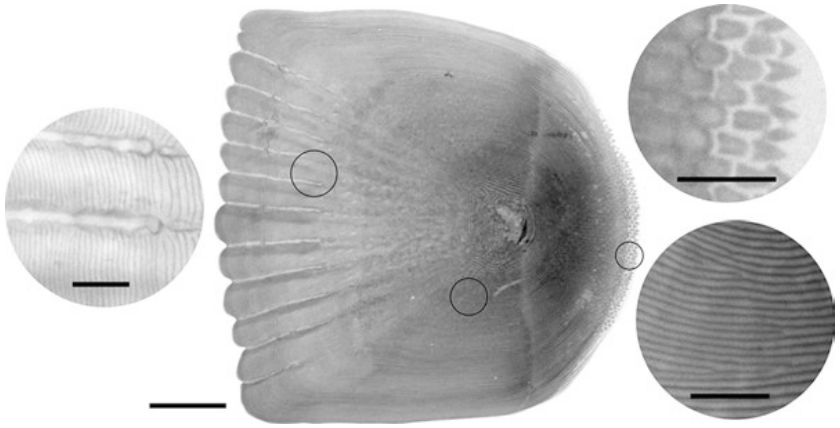

Fig. 10.4 Common features of fish scales. A single cleared and stained scale from a bluegill is shown, anterior to the left and dorsal above. Left inset shows radii, which appear as gaps in the mineralized layers of the scale. Top right inset shows ctenii, which are separate ossified spines that occur at the edge of ctenoid scales. In this scale, the outermost two rows of ctenii are separate mineralizations from the body of the scale, while the other inner (and older) rows of ctenii become mineralized together. Bottom right inset shows circuli, which are concentric ridges on the surface of scales. Scale bar for center image: 1 mm. Scale bars for insets: 200 μm

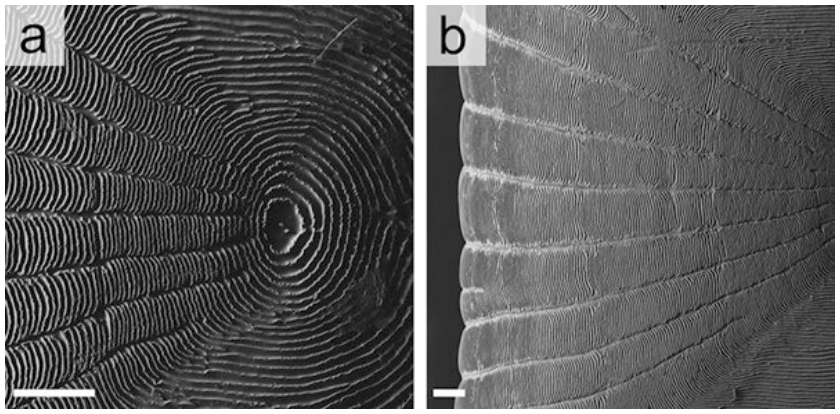

Fig. 10.5 Images of bluegill (*Lepomis macrochirus*) scales taken with scanning electron microscopy (SEM). Anterior is to the left. (**a**) The concentric raised ridges called circuli are clearly visible starting from the focus. Radii are also evident on the anterior part of the scale (left) as breaks in the circuli that radiate from the center to the edge of the scale. (**b**) The anterior margin of the scale with the radii is shown. Scale bars 200 μm (Images credited to James Weaver)

a yearly mark. Circuli can be seen clearly in Figs. 10.4 and 10.5a as they grow around the center of a bluegill scale.

Radii are radial breaks in the mineralization of the scale (but not the unmineralized tissues; Schönbörner et al. 1979) that look like physical gaps in CT scans and cleared and stained scales (Fig. 10.4) or cracks in SEM (Fig. 10.5). Radii are visible in most fish only when the scale is removed from the body because they occur on the anterior

portion of the scale, which is normally covered and layered below more anterior scales (Roberts 1993; Esmaeili et al. 2012). However, some species have radii on the dorsal and ventral regions of the scale (the lateral fields) (e.g. Daniels 1996).

Ctenii are spines that come in a variety of sizes and shapes, and it is often the case that most of the visible portion of the scale (called the posterior field) is made of interlocking ctenii. In these cases, usually only the posterior-most one or two rows of ctenii are whole spines, while the other older ctenii are reduced to shortened interlocking stubs, as shown in Fig. 10.4 (Roberts 1993). The further towards the outer scale margin ctenii are, the younger they are – similar to circuli which grow around the scale center as the scale grows at the edge (Sire 1986; Sire and Arnulf 1990). Because ctenii are separate ossifications from the body of the scale (Fig. 10.4), they may be flexible and can potentially bend relative to the body of the scale to either point externally or internally.

Circuli, radii, ctenii, spines, and other scale features such as overall shape suggest a host of different hypotheses concerning scale function. We have discussed multiple hypotheses for scale structure-function relationships previously (Wainwright and Lauder 2016) and we will summarize several here. Ctenii, spines, circuli, radii, scale shape, and scale curvature may all result in changes in scale stiffness compared to scales without these features. For example, flexibility may be added by fields of separate spiny ctenii, as well as by radii. Increased scale flexibility could benefit undulatory swimmers by decreasing the force needed to bend the scales and skin. Stiffness may be increased using circuli that increase the second moment of area of a scale or by adding curvature to scales, which creates anisotropic stiffness by increasing the second moment of area with respect to different bending axes. Increasing the stiffness of scales could be beneficial for functions like physical protection – creating a scale resistant to bending with little material allows for economical armor.

Fish scales and their features have also been proposed to function hydrodynamically in swimming, with flow being directed in a beneficial way by scale surface structures (Burdak 1986; Wainwright and Lauder 2016; Lauder et al. 2016). Circuli, ctenii, spines of spinoid scales, and scale pattern may either generate turbulence or control turbulence in ways that decrease the overall drag on a fish's body (Anderson et al. 2001; Wainwright and Lauder 2016; Liyan et al. 2017). These fluid mechanisms are dependent on many factors including flow speed, fish size and shape, swimming kinematics, and scale morphology, making it very difficult to investigate the hydrodynamic roles of scale surface structures in these dynamic, small-scale, and species-specific systems. There have been some attempts to assign hydrodynamic functions to fish scales (Aleyev 1977; Burdak 1986; Sagong et al. 2008; Liyan et al. 2017), but these studies either do not present quantitative results or do not test real fish skin. We still know little about how fish surfaces impact the flow around them, and in fact we know little in general about the boundary layer flows around swimming fish (although see Anderson et al. 2001, Yanase and Saarenrinne 2015).

In addition to a potential hydrodynamic role, the microroughness of fish scales created by circuli and ctenii may also function to hold the epidermis and mucus on scales. Covering circuli and ctenii with mucus would make the fish's surface

smoother, which could act to either maintain laminar flow close to the body or prevent boundary layer separation, thereby reducing surface friction (Daniel 1981; Bernadsky et al. 1993). In this case, perhaps fish skin satisfies immune and hydrodynamic functions through the epidermis and mucus, and creates physical protection with bony scales. The functional hypotheses we have outlined above are in no way an exhaustive list of fish scale function and certainly different species may utilize scales and skin in different ways. Furthermore, scales, epidermis, and mucus are undoubtedly a system with multiple biological functions and many of the potential functions of fish skin mentioned above could occur together.

Because of our lack of knowledge tying particular scale morphologies to function, it is important to continue to investigate scale morphology so that we can better understand the diversity of scales and begin to understand how different scales may influence interactions between a fish and its environment. To do this, we first need to understand scale structure in both two and three dimensions to build a strong foundation for testing hypotheses of scale function. Hydrodynamic interactions happen in three dimensions, making it necessary for us to understand the surface topography of scaled surfaces before theorizing about mechanisms fish scales may employ to alter flow during locomotion. This includes the need for additional study of mucus on fish skin and *in vivo* fish surfaces, as seen below in Sect. 10.3.

10.2.3 Investigating Scales – SEM, μCT, Histology, and Profilometry

Studying fish scales and fish skin requires techniques that are able to image sizes in the micron to centimeter range and detect tissues from mucus to bone, which exhibit a range of material and optical properties, and different degrees of hydration. Not many techniques can accomplish all of these at once, but researchers have used optical microscopy, scanning electron microscopy (SEM), micro x-ray computed tomography (μCT), histology, and profilometry to study fish scales and skin. We will briefly discuss some of the benefits of SEM, μCT, histology, and profilometry below. To our knowledge, few studies to date have used μCT and profilometry on fish skin and scales to generate three-dimensional data (Sudo et al. 2002; Wainwright and Lauder 2016; Lauder et al. 2016; Wainwright et al. 2017) – historically, SEM and histology have been the most common approaches to the study of fish skin.

SEM has been a popular way to image and measure scale features for decades and has produced many valuable scale descriptions that reveal patterns of scale evolution and detailed two-dimensional scale morphology of particular species (e.g. Roberts 1993; Johal et al. 2006; Jawad and Al-Jufaili 2007; Sankar et al. 2008; Esmaeili et al. 2012). SEM is an effective technique for investigating scale microstructures such as ctenii, radii, and circuli (Sire and Arnulf 2000; Sire and Huysseune 2003; Meunier and Brito 2004), especially when epidermis and mucus coatings have been removed using dehydration and sample preparation. SEM has also been used to investigate the plywood-like arrangement of fibers in the elasmodine layer

of scales (Meunier 1981; Zylberberg et al. 1988). SEM benefits from fields of view anywhere from a few square micrometers to a few square millimeters and reveals surface details within this range to great effect. However, SEM usually requires specimen preparation (drying, sputter coating) and traditionally only offers two-dimensional information (although environmental SEM requires less specimen preparation). Thus, SEM is not a good technique for understanding the topography of scales or mucus-covered surfaces, but it is a good technique for observing fine details on scale surfaces. Figure 10.5 shows some examples of SEM images of bluegill (*Lepomis macrochirus*) scales, which clearly demonstrate the radii and circuli.

μCT has become an increasingly widespread technique used in research to obtain three-dimensional information about morphology. Because μCT uses x-ray projections to reconstruct morphology, it works best on mineralized biological tissues like bone and shell, although there are now several effective techniques for staining soft tissues with metal ions to enhance CT scan contrast of neural tissue, connective tissues, and muscle (e.g. Descamps et al. 2014; Gignac et al. 2016). Scales are mineralized and thus make good specimens for μCT analysis and the average laboratory μCT resolution of 5–50 microns is within the appropriate range for imaging most fish scales. μCT scans are excellent for reconstructing the full three-dimensionality of scale shape and larger scale features, and they provide a good mechanism for developing computer and physical models of fish scales that could be tested in various experimental and simulation approaches in the future. One downside of laboratory μCT is that this technique is not particularly good at reconstructing the smallest surface features of scales such as individual ctenii or circuli (Wainwright and Lauder 2016). Reconstructing surface renderings of x-ray slices at typical resolutions of 5–50 micron voxel size tends to smooth out small features such as circuli and small ctenii, and the degree of surface roughness is greatly affected by the quality of the render and the values used for thresholding gray values to create the surface.

However, for investigating the volume, structure, and shape of scales in three dimensions, μCT is a good technique to use. We show an example of μCT scans of scales from two different species in Fig. 10.6, illustrating the three-dimensional nature of the data generated with this approach, which can produce three-dimensional surfaces and two-dimensional cross sections through different anatomical planes. Such cross-sectional views are useful for visualizing the relative placement of groups of scales *in situ*, the degree of scale overlap, and the nature of inter-scale connections and contact (Fig. 10.6).

Histology is a tool for investigating scale internal structure and it has the benefit of imaging both soft and hard tissues. Although histological sections can be used as image stacks to reconstruct morphology in three dimensions, it is traditionally a two-dimensional technique. Histology allows us to gain an understanding of relative position of scales and associated soft tissues, and it provides a wealth of information about the structure and composition of different tissues. Compared to SEM and μCT, histology is excellent at displaying soft tissues like the epidermis of fish and goblet cells filled with mucus (Fig. 10.7). Furthermore, histology also provides a method to measure the relative thickness of different skin elements in different species and to generally inspect the structure of the dermis, scales, epidermis, and

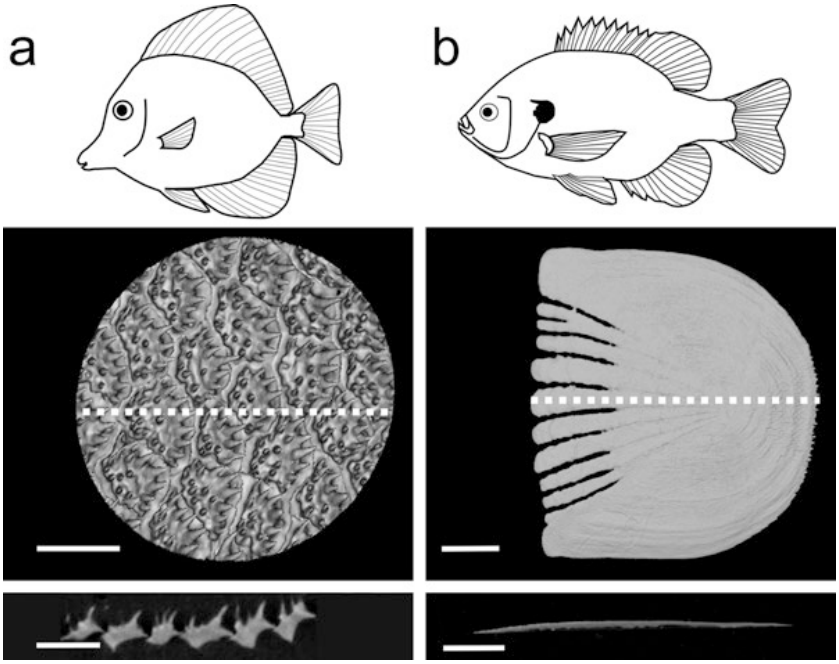

Fig. 10.6 Surface renderings and cross-sections of scales from two species illustrated with models generated from μCT. (**a**) Scales from the yellow tang (*Zebrasoma flavescens*) are shown in a surface rendering containing over 20 scales. A cross-section also shows the three-dimensional nature of these scales and the complex surface texture. (**b**) A scale from a bluegill (*Lepomis macrochirus*) with typical teleost scale morphology. Gaps on the anterior edge are radii, and ctenii are visible on the posterior edge. Cross sectional view below shows that the scale is a single bony plate; note also substantial differences in scale size between these two species. Scale bars: 1 mm

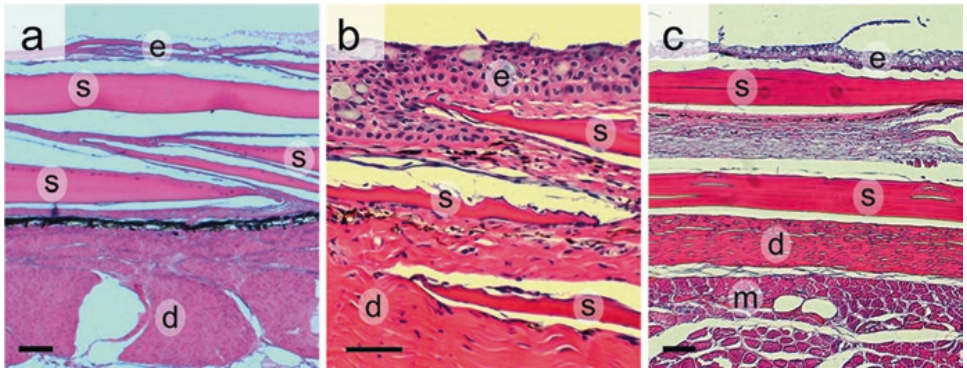

Fig. 10.7 Histological sections of skin and scales for three different fish species. Each sample is stained with hematoxylin and eosin. (**a**) Bigeye tuna (*Thunnus obesus*) has 200 μm thick scales but only a very thin epidermal layer. A dark layer of pigmented tissue is visible above the connective tissue of the dermis. (**b**) Brook trout (*Salvelinus fontinalis*) has a thick epidermis with many goblet cells and thin scales embedded in scale pockets. (**c**) Bluegill (*Lepomis macrochirus*) shows a clear epidermis above and between scales. The dermis lies external to deeper muscle fibers. d: dermis, e: epidermis, m: muscle fibers, s: bony scales. Scale bars: 100 μm

underlying muscle. Disadvantages of histology include difficulty in reconstructing accurate 3D information from slice data and challenges in sectioning fish skin, due to the proximity and location of soft, delicate tissue (epidermis) that is external to hard mineralized tissue (scales). We show histological sections through the skin from three species in Fig. 10.7 to highlight selected structural differences among these species. The relative thickness of the epidermis, scales, and dermis is different in each species, even when the general pattern of bony scales embedded in the dermis remains similar.

For research on fish surface topography, we have found that gel-based surface profilometry (described below) is an excellent method for capturing details of fish surfaces in three dimensions, regardless of skin optical or material properties and without the need for specimen preparation (Wainwright et al. 2017). We use a gel-based profilometry system manufactured by GelSight Inc. (Waltham, MA) that takes images through clear flexible gels pressed onto a surface of interest (Johnson and Adelson 2009; Johnson et al. 2011; Li and Adelson 2013). The contact surface of these clear gels has an opaque coating that standardizes the optical properties of the surface. Six photographs are taken of each surface using a different lighting angle for each image. These photographs are then reconstructed into a three-dimensional topographic map of the surface, which can be quantified using surface metrology metrics such as root-mean-square roughness (Table 10.1). This method

Table 10.1 Root mean square roughness (Sq) values for the nine species in Figs. 10.2, 10.3 and 10.7. Common manufactured surfaces are included for reference

Surface	Roughness Sq (μm)
Extruded aluminum	0.06
1000 grit sandpaper	6.3
Back of hand (*Homo sapiens*)	14.3
Moorish Idol (*Zanclus cornuta*)	14.9
500 grit sandpaper	16.2
Bonefish (*Albula vulpes*)	17.9
Shad (*Anodontosoma chacunda*)	20
Sergeant (*Abudefduf sordidus*)	25.2
Smelt (*Osmerus mordax*)	26.1
Squirrelfish (*Sargocentron spiniferum*)	30.1
Boarfish (*Antigonia capros*)	32.7
Cowfish (*Acanthostracion quadricornis*)	38.6
80 grit sandpaper	53.6
Louvar (*Luvaris imperialis*)	76.5

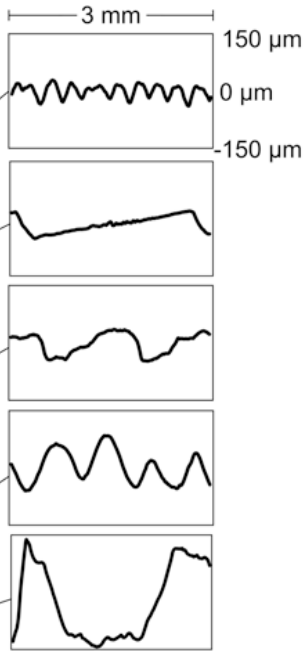

allows for the study of skin on living (anesthetized) fishes, providing a means of understanding the effect of the mucus coating over the surface of scales.

Gel-based profilometry provides significant advantages for studying fish surfaces involved in interactions with the environment because it can reconstruct surfaces in three dimensions, and because this technique can image large fields of view (square centimeters to square millimeters) at high spatial resolutions (each topographic image represents over 18 million three-dimensional points in *x, y,* and *z*). The high-throughput and non-invasive nature of this technique also allows for the study of living animals with the mucus coating intact. Three-dimensional surface data are crucial to furthering the study of hypotheses regarding hydrodynamic function, and techniques like gel-based profilometry allow us to quickly gather this topographic data without damaging or destroying specimens.

We show a reconstruction of the surface of a rainbow smelt (*Osmerus mordax*) from gel-based profilometry and analysis using MountainsMap 7 (Digital Surf Inc., Besançon, France). In Figs. 10.8 and 10.9 displaying this technique, warmer colors correspond to higher elevations on the surface. Using surface profilometry data, elevation profiles can be easily created for analyzing specific surface features, and the surface itself can be used to calculate a large number of canonical surface metrology parameters. We have calculated root-mean-square roughness (Sq) of

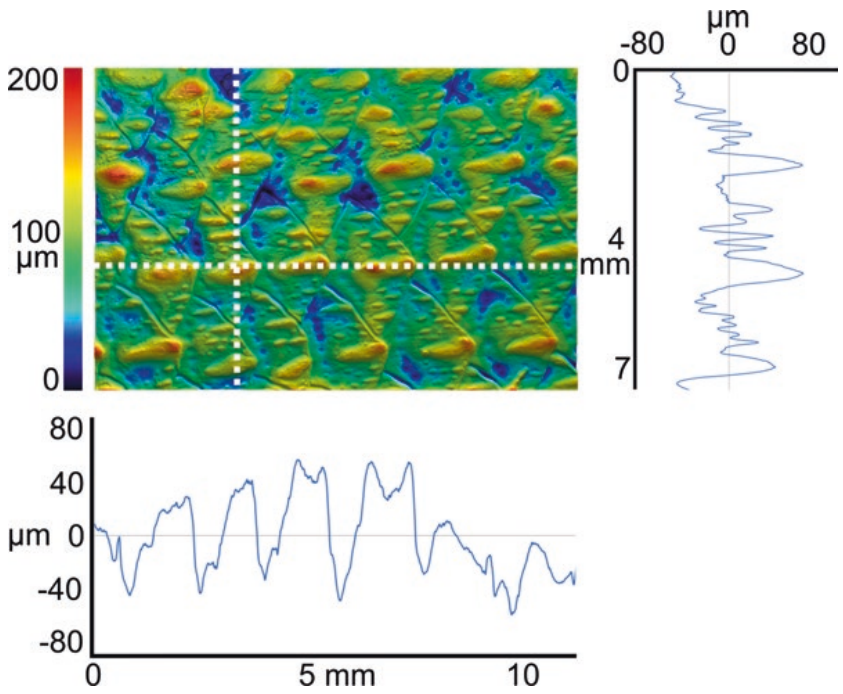

Fig. 10.8 Topographic surface of scales from a rainbow smelt (*Osmerus mordax*) reconstructed using gel-based profilometry. Color refers to elevation, with red colors being highest above the surface. Two orthogonal profile lines are shown to illustrate the three-dimensional nature of these surface data

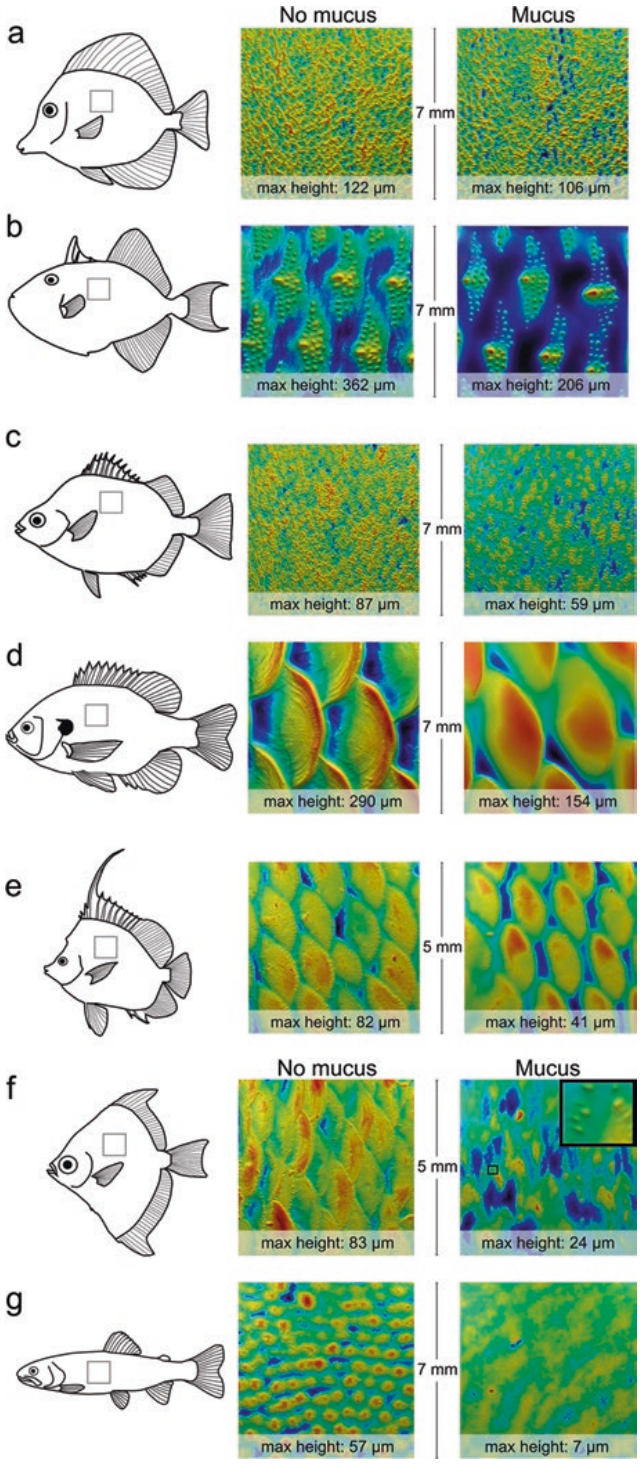

Fig. 10.9 The effect of mucus on fish surface topography. (**a**) Yellow tang (*Zebrasoma flavescens*). (**b**) Niger triggerfish (*Odonus niger*). (**c**) Spotbanded scat (*Selenotoca multifasciatus*). (**d**) Bluegill (*Lepomis macrochirus*). (**e**) Singular bannerfish (*Heniochus singularis*). (**f**) African moony (*Monodactylus sebae*). (**g**) Brook trout (*Salvelinus fontinalis*)

many fish surfaces as well as some manufactured surfaces (extruded aluminum and various sandpapers). Sq represents an average distance a point is from the mean height of the surface. The Sq parameter is calculated by taking a mean height of the surface and then for each point on the surface, subtracting its value from the mean height. These differences between the point and the mean are then squared, integrated across all of the points on the surface, and averaged. Finally, this integrated average value is square-rooted to account for squaring the differences in height. Table 10.1 shows Sq roughness values for several different species of fish discussed in this chapter compared to some manufactured materials. Many other surface metrology parameters exist that describe other topographic qualities. We have previously used skew and kurtosis (which describe the distribution of heights over a surface), max height (another measure of roughness), and texture direction (which evaluates the direction of dominant topographic patterns) (Wainwright and Lauder 2016; Wainwright et al. 2017), but there are an additional 20–30 common surface metrology parameters used in a variety of applications (Whitehouse 1994). We can use these numerous parameters to search for functional traits of fish scales by studying how parameters such as Sq roughness change with different fish that exhibit different behaviors or levels of swimming performance.

10.3 Slippery Surfaces – How Mucus Changes Fish Skin Texture

10.3.1 Fish Surfaces with Mucus

We have previously demonstrated how gel-based profilometry can be used to image the mucus and epidermis that covers scales on anesthetized fishes (Wainwright et al. 2017) and here we present data including *in vivo* surface images from seven different species: yellow tang (*Zebrasoma flavescens*), niger triggerfish (*Odonus niger*), spotbanded scat (*Selenotoca multifasciatus*), bluegill sunfish (*Lepomis macrochirus*), singular bannerfish (*Heniochus singularis*), African moonys (*Monodactylus sebae*), and brook trout (*Salvelinus fontinalis*). We used gel-based profilometry to image the lateral midbody and the peduncle region on each living fish after anesthetizing them with tricaine methanesulfonate (MS-222). We then preserved each individual in a 3.4% formalin solution and imaged the surface again after brushing the surface to remove preserved mucus and epidermis. We imaged one individual of each species in this manner.

We present images of the surfaces both with and without mucus of each species imaged in Fig. 10.9. Note that each image has a different elevation range and we give the maximum height (the elevation value that corresponds to the darkest red) for each image. We have ordered the presentation of these seven species to illustrate how mucus can change the apparent features created by fish scales. The yellow tang in Fig. 10.9a has a surface that changes very little with the presence of mucus and

epidermis. Yellow tangs have scales made of many small laterally projecting spines that protrude clearly above the mucus layer so removing mucus has little effect on the overall topography of their surfaces (Fig. 10.6a also shows yellow tang scales). The niger triggerfish (Fig. 10.9b) and spotband scat (Fig. 10.9c) show similar trends but at different sizes. Both species have raised portions of their scales that clearly protrude past the mucus layer when it is present. However, the boundaries of individual scales are only clear when mucus is removed (i.e. mucus fills the surface and obscures the scale boundaries).

In Fig. 10.9d and e, we show surfaces from a bluegill and a bannerfish, which have similar patterns with and without mucus. Without mucus, the scales of both species are obvious, as are small features on the scale surfaces such as ctenii at the margin and circuli on the body of the scale. However, mucus and the epidermis obscure these small features when present, and instead only the general shape of the scale is obvious in our images with mucus present. Next, we show the surfaces of the moony, which has small scales with ctenii at the posterior margin (Fig. 10.9f). These scales become almost completely obscured in the presence of mucus and epidermis, and instead the only visible features are the small ctenii at the posterior margin of each scale (inset in Fig. 10.9f). Finally, we show how the brook trout's surface changes with and without mucus: trout have small smooth-edged cycloid scales that become completely covered when the epidermis and mucus layers are intact in anesthetized specimens, and maximum surface height is only 7 μm (Fig. 10.9g).

From tang to trout, we see a clear gradient of increasing changes to surface topography with the presence of mucus; yellow tang have surfaces that are very similar with or without mucus, and in contrast, trout scales are completely concealed by mucus. Fish in the middle of this gradient either have scale microstructures obscured (bluegill, bannerfish), scale boundaries obscured (trigger, scat), or most of the scales obscured, and only a few features visible (moony) when mucus and epidermis are present. We also measured the roughness of these seven species with and without mucus and compare values in Table 10.2. We show both quantitatively (Table 10.2) and qualitatively (Fig. 10.9) that surfaces without mucus are rougher than those with mucus, yet there is considerable diversity in this effect. The yellow tang has the smallest decrease in roughness with a 0% change (although the peduncle region of the yellow tang actually shows a curious increase in roughness with mucus) while the trout has the largest percentage decrease in roughness, with a 93% loss. A nominal range from a 0% to a 93% drop in roughness illustrates a challenge of studying fish surfaces – sometimes mucus matters a great deal, but other times it has little effect on surface roughness. We are puzzled by the increase in roughness measured on the yellow tang peduncle scales with mucus compared to without mucus, but we believe this could result from having flexible scales before preservation, that when pressed, will rotate to have spines elevated in line with the z-axis of our measurements, creating higher roughness (whereas in preserved specimens, the scales are fixed and no longer flexible in the skin).

Table 10.2 Roughness of fish surfaces with and without mucus at mid-lateral body (shown in Fig. 10.9) and peduncle positions

Species	Location	No mucus roughness Sq (μm)	Mucus roughness Sq (μm)
Tang	Body	15.2	15.2
	Peduncle	26.0	36.9
Triggerfish	Body	38.7	21.8
	Peduncle	43.5	43.5
Scat	Body	10.9	6.2
	Peduncle	13.9	7.4
Bluegill	Body	55.7	33.5
	Peduncle	61.5	40.8
Bannerfish	Body	10.8	6.9
	Peduncle	9.5	4.4
Moony	Body	11.0	2.7
	Peduncle	11.5	6.1
Trout	Body	8.6	0.6
	Peduncle	10.3	3.9

10.3.2 What Mucus Means for Hypotheses of Function

Mucus has long been considered an important part of fish swimming (Daniel 1981; Bernadsky et al. 1993), and our topographic data have important implications for how fish surfaces may function hydrodynamically, as mucus clearly alters surface roughness and the effect of mucus in obscuring surface roughness changes along the body (Table 10.2). Furthermore, there is not necessarily a correlation between the appearance of scales and what those scales look like when covered by epidermis and mucus. For example, both the moony (Fig. 10.9f) and the bannerfish (Fig. 10.9e) have similar size and elevated features on their scales, but anesthetized specimens with mucus intact appear different in these two species. This indicates that not only does scale morphology differ between species, but so too does the morphology of the epidermis and mucus layers, showing us that the topography of live fish is determined by interactions between scale, epidermis, and mucus morphology.

The interaction between the complex structure of scales and the slippery nature of epidermis and mucus changes many of the hypotheses concerning the function of fish scale morphology. Many of the species we imaged have part or all of their ctenii and circuli completely obscured by epidermal tissues or mucus and thus, it seems that in these species and others like them, ctenii and circuli will not play a role in locomotor hydrodynamics except perhaps an indirect one by holding mucus and epidermis on the surface. However, we do not know if patterns of body bending during swimming might expose ctenii to water flow as scales bend and slide past each other as the body undulates. The effect of body bending patterns on scale relative position and surface feature exposure remains entirely unknown.

One additional complexity is that fish scale morphology changes across a fish's body (e.g. Jawad 2005; Wainwright and Lauder 2016), and we have noted rougher and more rugose scales in the peduncle and other posterior regions in many species that we have investigated (Wainwright and Lauder 2016; Wainwright et al. 2017). Because of this, it is possible that anterior scales or scale features could be covered by mucus and epidermis, but more extreme-featured posterior scales may be less changed by the epidermis and mucus layers. Fluid flow along the body of a fish will change as flow moves from head to tail because of the natural development of boundary layer flow coupled with changes in movement and body shape. It is possible that scales are hidden under mucus on anterior parts of a fish where there is a laminar boundary layer and then protrude into the boundary layer towards the tail to create turbulence and maintain flow attachment.

Functional measurements of how fish scales change boundary layer flow do not exist. There are some measurements of fish boundary layers (Anderson et al. 2001; Yanase and Saarenrinne 2015) and they indicate that swimming fish likely experience both laminar and turbulent boundary layers depending on Reynolds number, fish kinematics, and the region of the fish being investigated. These measurements come from just two species of bony fish, however, and thus cannot provide much information on the effect of scales. In order for us to begin to answer how scales interact with boundary layer flows, we need careful experimental measurements of the boundary layer of fish skin, starting with static conditions and eventually moving towards dynamic testing with flapping skin pieces with and without mucus, and finally to free-swimming fish. To investigate different skin topographies, we need careful choice of fish species to compare not just one species to another, but to compare general scale morphologies against one another. These experiments could also be accomplished with physical models if models are validated as having similar flow properties to fish scales, as has been done in placoid shark scales (Wen et al. 2014; Wen et al. 2015).

Until experiments on boundary layer flow over different fish scale morphologies are completed, we can focus the discussion on scale topography and boundary layer interactions in another way. The engineering parameter k+, also known as roughness Reynolds number (Jimenez 2004), provides an estimate of whether surface roughness will change boundary layer characteristics. k+ values do not estimate whether an effect on the boundary layer will be beneficial or not – they simply estimate if a surface has features that are large enough to change flow in the boundary layer relative to a smooth surface. The k+ parameter is calculated by multiplying friction velocity of the fluid by the height of surface features and dividing by the viscosity of the fluid of interest (Jimenez 2004; Schultz and Flack 2007). Viscosity of salt or freshwater is known, the size of surface features can be measured with gel-based profilometry, and friction velocity can be estimated using power law equations involving the Reynolds number (Smits 2000). Because calculating friction velocity uses the Reynolds number, a known or estimated swimming speed is needed, along with the distance from the anterior tip of the body to the region under investigation. This also means that each k+ value is relevant only for a particular swimming speed and location on the body. k+ values of less than three indicate that

surface features are too small to disturb the boundary layer; values over three indicate that surface features are likely to change the boundary layer flow.

Although the height of surface features is incorporated into k+ estimation, surface geometry and patterning are also important to boundary layer effects and are not taken into account with k+. For example, if two surfaces have the same feature size, but one surface is covered in smooth-sloping ridges while the other is covered in sharp-peaked ridges, the sharp ridges will be more likely to change boundary layer flow because sharp features provide natural separation points on the surface. Aside from ignoring surface geometry, simple calculations of k+ also assume that objects are not moving across the flow, a condition that is violated during undulatory fish swimming, especially on posterior regions of the body. Nonetheless, a cutoff value of three for k+ is sufficiently conservative and our k+ values will give us a guide for future data collection. Questions relating to boundary layer flows on a deforming flexible object with a surface coating are complex, and k+ can provide a useful initial piece of a broader multivariate approach.

We can use k+ as a way of narrowing the field of potential scale functions – if a particular fish's surface has a k+ below three, then its surface features are simply too small to have a substantial effect on the boundary layer. In Fig. 10.10 we present k+ values for the different species in Fig. 10.8 using surface profilometry data and estimates of swimming speed. We include values for surfaces with mucus and for swimming both at one body-length per second and three body lengths per second. We also include values calculated from scale height data at the midbody of each fish (Fig. 10.8) as well as from the peduncle of the fish. Note that these values are for the specific specimens we used in this study and the specific regions we imaged on their body surfaces. Caution should be used before extrapolating these results to larger individuals of the same species or different regions on the same species. Additionally, we are not accounting for either surface geometry (sharpness of corners of edges, spacing between peaks) or body undulation, so our k+ values should be viewed as hypotheses instead of corroborated results.

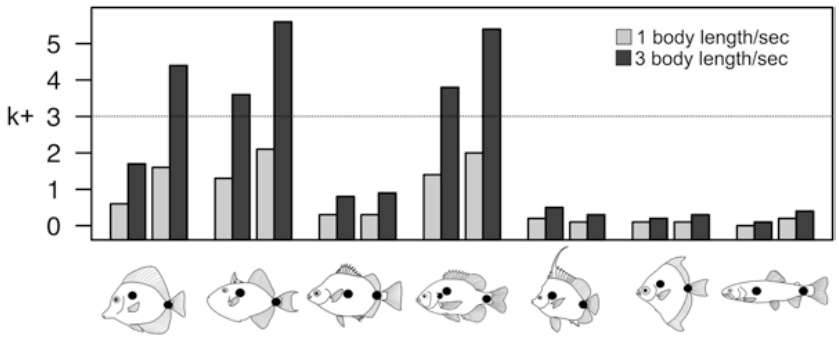

Fig. 10.10 Calculated k+ values of fish with mucus at body and peduncle regions at two different swimming speeds, one and three body lengths per second (see legend). From left to right species, with body region always followed by the peduncle region: yellow tang, niger triggerfish, scat, bluegill, bannerfish, moony, trout. k+ cutoff value of three is marked with a line – values above three indicate surfaces where flow may be altered in the boundary layer

We find that the only fish with k+ values above three are yellow tang, niger triggerfish, and bluegill (Fig. 10.10). These fish have the roughest surfaces among the seven species we investigated (Table 10.2), so it is unsurprising that these are the fish that are most likely to have scales that change the boundary layer flow in some way, even with the presence of mucus and epidermis. Yellow tang has skin with many small distal-pointing spines on their scale surfaces and these spines increase in size at the peduncle, just anterior to the scalpel-like spine also located there. It is these larger spines that are likely the reason the yellow tang shows a k+ over three only on the peduncle at the higher swimming speed of three body lengths per second. The triggerfish has k+ values above three on body and peduncle regions, but only at swimming speeds of three body lengths per second, indicating surface geometry may only affect the boundary layer at high swimming speeds. Bluegill also shows high k+ values on both body and peduncle regions only at the faster swimming speed of three body lengths per second. Calculating k+ provides a way of identifying potential candidates for future experimental studies of boundary layers around swimming fish.

10.4 Concluding Remarks

Fish scales display a vast diversity of morphology – scale size, shape, and internal structure vary among species, different populations of the same species, and on different regions of the same fish (Margraf and Riley 1993; Roberts 1993; Dapar et al. 2012; Wainwright and Lauder 2016). While we have a basic understanding about how scales vary and develop (Suzuki 1971; Roberts 1993; Sire and Akimenko 2004) and we have been able to quantify scales in two dimensions (Ibañez et al. 2007; Ibañez et al. 2009), we have only just begun to understand the surface of scales and fish skin in three dimensions, and we still have no understanding of how scale morphology and deployment changes with fish activity. Gel-based profilometry provides a method of reconstructing the surface topography of scales in different species of fish with the hopes of eventually using this information to elucidate the function of different scale morphologies (Wainwright and Lauder 2016; Lauder et al. 2016; Wainwright et al. 2017). Understanding scale topography in three dimensions is both necessary and important for studying fish scale hydrodynamic function because of the role surface features have in changing boundary layer flows. Furthermore, understanding the three-dimensional morphology of fish scales in a quantitative manner allows for more rigorous exploration of fish surfaces in the contexts of morphology, evolutionary patterns, and the form-function relationship of scales.

We also demonstrated how fish scale topography changes on fish where mucus and skin are still intact atop the scales. Using gel-based profilometry, we have discovered that mucus and epidermis can often obscure and cover small structures present on fish scales, which changes the roughness and structure of a mucus-coated surface compared to a preserved fish without mucus or epidermis. By imaging a diverse sample of seven species, we show that scale morphology alone is a poor predictor of *in vivo* skin topography, and that mucus, epidermis, and scales interact

to form complicated 3D surfaces. Some fish have rough surfaces that are barely changed with the presence of live skin tissues (yellow tang, triggerfish), while others have scales that are completely changed by mucus and epidermis to create a very smooth external surface (trout). It is likely that most fish fall in the middle of this spectrum, with most scale microstructure obscured by mucus but with general scale shape still visible, perhaps also with some spines or ctenii. The imaging and quantitative comparison of mucus-covered fish surfaces is a new area of research and reveals what surfaces are like on living fish, which is vital information for understanding what type of surface the water interacts with during swimming.

Despite promising new techniques to image and quantify fish scale topography, we still know little about fish scale function. Other authors have studied the armor-like aspects of fish scales (Vernerey and Barthelat 2010; Song et al. 2011; Browning et al. 2013; Chintapalli et al. 2014; Vernerey and Barthelat 2014; Duro-Royo et al. 2015), and the roles fish skin have in body and skin bending (Long et al. 1996; Ghosh et al. 2014; Szewciw et al. 2017), yet work on the hydrodynamic effect of fish scales remains hypothetical (Walters 1963; Burdak 1986; Sudo et al. 2002; Liyan et al. 2017). In part, it is challenging to experimentally study fine-scale flows on swimming fish, which is compounded by the fact that we also know little about boundary layer flow around freely-swimming fishes. In order to investigate how and if fish scales change boundary layer flow for better or worse, we can use metrics like k+ to search for surfaces of potential interest, and then investigate function experimentally. Using micro-scale particle image velocimetry with real fish skin pieces, using physical models of scales or fish surfaces, or using phylogenetic comparative methods to link different scale morphologies with ecology or swimming performance are all key areas for future study. The functional implications of the complex and slippery surfaces of fish remains an intriguing and understudied area of fish biology, and with research on scale morphology, surface topography, fluid mechanics, and evolutionary patterns, we can move toward a comprehensive understanding of the form and function of fish surfaces.

Acknowledgements We would like to acknowledge James Weaver for his imaging expertise (in particular for the images in Fig. 10.5), and Kimo Johnson for his assistance with GelSight profilometry measurements. We acknowledge Karsten Hartel and Andrew Williston with assistance in accessing specimens and Dr. Lex Smits for introducing us to k+. The research reported here was supported by ONR MURI Grant N000141410533 monitored by Dr. Bob Brizzolara, HFSP Young Investigators Grant (RGY0067- 2013) to James Weaver, and NSF GRF 2014162421 awarded to D.K.W.

References

Aleyev, Y. G. (1977). *Nekton*. Hague: Dr. W. Junk b.v. Publishers.

Anderson, E. J., McGillis, W. R., & Grosenbaugh, M. A. (2001). The boundary layer of swimming fish. *The Journal of Experimental Biology, 204*, 81–102.

Batts, B. S. (1964). Lepidology of the adult pleuronectiform fishes of Puget Sound, Washington. *Copeia, 4*, 666–673.

Beardsley, G. L. (1967). Age, growth, and reproduction of the Dolphin, *Coryphaena hippurus*, in the Straits of Florida. *Copeia, 1967*, 441.

Bereiter-Hahn, J., & Zylberberg, L. (1993). Regeneration of teleost fish scale. *Comparative Biochemistry and Physiology, 105A*, 625–641.

Bergman, J. N., Lajeunesse, M. J., & Motta, P. J. (2017). Teeth penetration force of the tiger shark *Galeocerdo cuvier* and sandbar shark *Carcharhinus plumbeus*. *Journal of Fish Biology, 91*, 460–472.

Bernadsky, G., Sar, N., & Rosenberg, E. (1993). Drag reduction of fish skin mucus: Relationship to mode of swimming and size. *Journal of Fish Biology, 42*, 797–800.

Besseau, L., & Bouligand, Y. (1998). The twisted collagen network of the box-fish scutes. *Tissue & Cell, 30*, 251–260.

Bone, Q. (1972). Buoyancy and hydrodynamic functions of integument in the Castor oil fish, *Ruvettus pretiosus* (Pisces: Gempylidae). *Copeia, 1972*, 78–87.

Browning, A., Ortiz, C., & Boyce, M. C. (2013). Mechanics of composite elasmoid fish scale assemblies and their bioinspired analogues. *Journal of the Mechanical Behavior of Biomedical Materials, 19*, 75–86.

Burdak, V. D. (1986). Morphologie fonctionnelle du tegument ecailleux des poissons. *Cybium, 10*, 1–128.

Casselman, J. M. (1990). Growth and relative size of calcified structures of fish growth and relative size of calcified structures of fish. *Transactions of the American Fisheries Society, 119*, 673–688.

Chintapalli, R. K., Mirkhalaf, M., Dastjerdi, A. K., & Barthelat, F. (2014). Fabrication, testing and modeling of a new flexible armor inspired from natural fish scales and osteoderms. *Bioinspiration & Biomimetics, 9*, 36005.

Daniel, T. L. (1981). Fish mucus: In situ measurements of polymer drag reduction. *The Biological Bulletin, 160*, 376–382.

Daniels, R. A. (1996). Guide to the identification of scales of inland fishes of northeastern North America. *New York State Museum Bulletin, 488*, 1–93.

Dapar, M. L. G., Torres, M. A. J., Fabricante, P. K., & Demayo, C. G. (2012). Scale morphology of the Indian goatfish, *Parapeneus indicus* (Shaw, 1803) (Perciformes: Mullidae). *Advance Envirronmental Biologico, 6*, 1426–1432.

Descamps, E., Sochacka, A., de Kegel, B., Van Loo, D., Hoorebeke, L., & Adriaens, D. (2014). Soft tissue discrimination with contrast agents using micro-ct scanning. *Belgian Journal of Zoology, 144*, 20–40.

Duro-Royo, J., Zolotovsky, K., Mogas-Soldevila, L., Varshney, S., Oxman, N., Boyce, M. C., & Ortiz, C. (2015). MetaMesh: A hierarchical computational model for design and fabrication of biomimetic armored surfaces. *Computer-Aided Design, 60*, 14–27.

Esmaeili, H. R., Gholamifard, A., Zarei, N., & Arshadi, A. (2012). Scale structure of a cyprinid fish, *Garra rossica* (Nikol'skii, 1900) using scanning electron microscope (SEM). *International Journal of Science, Technology and Society, 4*, 487–492.

Esteban, M. Á. (2012). An overview of the immunological defenses in fish skin. *ISRN Immunology, 2012*, 1–29.

Fast, M. D., Sims, D. E., Burka, J. F., Mustafa, A., & Ross, N. W. (2002). Skin morphology and humoral non-specific defence parameters of mucus and plasma in rainbow trout, coho and Atlantic salmon. *Comparative Biochemistry and Physiology A, 132*, 645–657.

Ghosh, R., Ebrahimi, H., & Vaziri, A. (2014). Contact kinematics of biomimetic scales. Applied Physics Letters. *105*, 233701-1-233701-5.

Gignac, P. M., Kley, N. J., Clarke, J. A., Colbert, M. W., Morhardt, A. C., Cerio, D., Cost, I. N., Cox, P. G., Daza, J. D., Early, C. M., et al. (2016). Diffusible iodine-based contrast-enhanced computed tomography (diceCT): An emerging tool for rapid, high-resolution, 3-D imaging of metazoan soft tissues. *Journal of Anatomy, 228*, 889–909.

Hawkes, J. W. (1974). The structure of fish skin I. General organization. *Cell and Tissue Research, 149*, 147–158.

Hill, K. T., Cailliet, G. M., & Radtke, R. L. (1989). A comparative analysis of growth zones in four calcified structures of Pacific Blue Marlin, *Makaira nigricans*. *Fishery Bulletin, 87*, 829–843.

Huysseune, A., & Sire, J.-Y. (1998). Evolution of patterns and processes in teeth and tooth-related tissues in non-mammalian vertebrates. *European Journal of Oral Sciences, 106*, 437–481.

Ibañez, A. L., Cowx, I. G., & O'Higgins, P. (2007). Geometric morphometric analysis of fish scales for identifying genera, species, and local populations within the Mugilidae. *Canadian Journal of Fisheries and Aquatic Sciences, 1100*, 1091–1100.

Ibañez, A. L., Cowx, I. G., & O'Higgins, P. (2009). Variation in elasmoid fish scale patterns is informative with regard to taxon and swimming mode. *Zoological Journal of the Linnean Society, 155*, 834–844.

Jawad, L. A. (2005). Comparative scale morphology and squamation patterns in triplefins (Pisces: Teleostei: Perciformes: Tripterygiidae). *Tuhinga, 16*, 137–167.

Jawad, L. A., & Al-Jufaili, S. M. (2007). Scale morphology of greater lizardfish *Saurida tumbil* (Bloch, 1795) (Pisces: Synodontidae). *Journal of Fish Biology, 70*, 1185–1212.

Jimenez, J. (2004). Turbulent flows over rough walls. *Annual Review of Fluid Mechanics, 36*, 173–196.

Johal, M. S., Esmaeili, H. R., & Sharma, M. L. (2006). Scale structure of a cobitid fish, *Cobitis linea* (Heckel, 1849) using different modes of SEM. *Current Science, 91*, 1464–1466.

Johnson, M.K. and Adelson, E.H. (2009). Retrographic sensing for the measurement of surface texture and shape. In: *2009 IEEE Conference on Computer Vision and Pattern Recognition*, 1070–1077.

Johnson, M. K., Cole, F., Raj, A., & Adelson, E. H. (2011). Microgeometry capture using an elastomeric sensor. *ACM Transactions on Graphics, 30*, 46.

Lauder, G. V., Wainwright, D. K., Domel, A. G., Weaver, J., Wen, L., & Bertoldi, K. (2016). Structure, biomimetics, and fluid dynamics of fish skin surfaces. *Physical Review Fluids, 1*, 060502.

Li, R., & Adelson, E. H. (2013). Sensing and recognizing surface textures using a GelSight sensor. In: *2013 IEEE Conference on Computer Vision and Pattern Recognition*, pp. 1241–1247.

Liyan, W. U., Zhibin, J., Yuqiu, S., Wentao, R., Shichao, N., & Zhiwu, H. (2017). Water-trapping and drag-reduction effects of fish *Ctenopharyngodon idellus* scales and their simulations. *Science China Technological Sciences, 60*, 1111–1117.

Long, J. H., Hale, M. E., McHenry, M. J., & Westneat, M. W. (1996). Functions of fish skin: Flexural stiffness and steady swimming of longnose gar *Lepisosteus osseus*. *The Journal of Experimental Biology, 199*, 2139–2151.

Margraf, F. J., & Riley, L. M. (1993). Evaluation of scale shape for identifying spawning stocks of coastal Atlantic striped bass (*Morone saxatilis*). *Fisheries Research, 18*, 163–172.

Meunier, F. J. (1981). "Twisted plywood" structure and mineralization in the scales of a primitive living fish *Amia calva*. *Tissue & Cell, 13*, 165–171.

Meunier, F. J. (2011). The Osteichtyes, from the Paleozoic to the extant time, through histology and palaeohistology of bony tissues. *Comptes Rendus Palevol, 10*, 347–355.

Meunier, F. J., & Brito, P. M. (2004). Histology and morphology of the scales in some extinct and extant teleosts. *Cybium, 28*, 225–235.

Meyer, W., & Seegers, U. (2012). Basics of skin structure and function in elasmobranchs: A review. *Journal of Fish Biology, 80*, 1940–1967.

Motta, P., Habegger, M. L., Lang, A., Hueter, R., & Davis, J. (2012). Scale morphology and flexibility in the shortfin mako *Isurus oxyrinchus* and the blacktip shark *Carcharhinus limbatus*. *Journal of Morphology, 273*, 1096–1110.

Rakers, S., Gebert, M., Uppalapati, S., Meyer, W., Maderson, P., Sell, A. F., Kruse, C., & Paus, R. (2010). "Fish matters": The relevance of fish skin biology to investigative dermatology. *Experimental Dermatology, 19*, 313–324.

Roberts, C. D. (1993). Comparative morphology of spined scales and their phylogenetic significance in the Teleostei. *Bulletin of Marine Science, 52*, 60–113.

Rosen, M. W., & Cornford, N. E. (1971). Fluid friction of fish slimes. *Nature, 234*, 49–51.

Sagong, W., Kim, C., Choi, S., Jeon, W.-P. and Choi, H. (2008). Does the sailfish skin reduce the skin friction like the shark skin? *Physics of Fluids*, *20*, 101510-1-101510-10.

Sankar, S., Sekar, S., Mohan, R., Rani, S., Sundaraseelan, J., & Sastry, T. P. (2008). Preparation and partial characterization of collagen sheet from fish (*Lates calcarifer*) scales. *International Journal of BIological Macromolecules, 42*, 6–9.

Schönbörner, A. A., Boivin, G., & Baud, C. A. (1979). The mineralization processes in teleost fish scales. *Cell and Tissue Research, 202*, 203–212.

Schultz, M. P., & Flack, K. A. (2007). The rough-wall turbulent boundary layer from the hydraulically smooth to the fully rough regime. *Journal of Fluid Mechanics, 580*, 381.

Shephard, K. L. (1994). Functions for fish mucus. *Reviews in Fish Biology and Fisheries, 4*, 401–429.

Sire, J.-Y. (1986). Ontogenic development scales in a cichlid *Hemichromis bimaculatus* (Cichlidae). *Journal of Fish Biology, 28*, 713–724.

Sire, J.-Y., & Akimenko, M.-A. (2004). Scale development in fish: A review, with description of sonic hedgehog (shh) expression in the zebrafish (*Danio rerio*). *The International Journal of Developmental Biology, 48*, 233–247.

Sire, J.-Y., & Arnulf, I. (1990). The development of squamation in four Teleostean fishes with a survey of the literature. *Jpn. Journal of Ichthyology, 37*, 133–143.

Sire, J., & Arnulf, I. (2000). Structure and development of the ctenial spines on the scales of a teleost fish, the cichlid *Cichlasoma nigrofasciatum*. *Acta Zoologica, 81*, 139–158.

Sire, J.-Y., & Huysseune, A. (2003). Formation of dermal skeletal and dental tissues in fish: A comparative and evolutionary approach. *Biological Reviews of the Cambridge Philosophical Society, 78*, 219–249.

Smits, A. J. (2000). *A physical introduction to fluid mechanics*. New York: John Wiley and Sons.

Song, J., Ortiz, C., & Boyce, M. C. (2011). Threat-protection mechanics of an armored fish. *Journal of the Mechanical Behavior of Biomedical Materials, 4*, 699–712.

Sudo, S., Tsuyuki, K., Ito, Y., & Ikohagi, T. (2002). A study on the surface shape of fish scales. *Trans. Jpn. Soc. Mechanical Engineering, 45*, 1100–1105.

Suzuki, T. (1971). Some scale patterns of the scad, Decapterus maruadsi (Temminck et Schlegel), and their variations with body parts. *Bulletin of the Japan Sea Regional Fisheries Research Laboratory 23*, 1–19.

Szewciw, L., Zhu, D., & Barthelat, F. (2017). The nonlinear flexural response of a whole teleost fish: Contribution of scales and skin. *Journal of the Mechanical Behavior of Biomedical Materials, 17*, 30252–30257.

Taylor, H. F. (1916). The structure and growth of the scales of the squeteague and the pigfish as indicative of life history. *Fishery Bulletin, 34*, 285–330.

Thomson, J. M. (1956). Interpretation of the scales of the yellow-eye mullet, *Aldrichetta forsteri* (Cuvier & Valenciennes) (Mugilidae). *Australian Journal of Marine and Freshwater Research, 8*, 14–30.

Vernerey, F. J., & Barthelat, F. (2010). On the mechanics of fishscale structures. *International Journal of Solids and Structures, 47*, 2268–2275.

Vernerey, F. J., & Barthelat, F. (2014). Skin and scales of teleost fish: Simple structure but high performance and multiple functions. *Journal of the Mechanics and Physics of Solids, 68*, 66–76.

Wainwright, D. K., & Lauder, G. V. (2016). Three-dimensional analysis of scale morphology in bluegill sunfish, *Lepomis macrochirus*. *Zoology, 119*, 182–195.

Wainwright, D. K., Lauder, G. V., & Weaver, J. C. (2017). Imaging biological surface topography *in situ* and *in vivo*. *Methods in Ecology and Evolution*. in press.

Walters, V. (1963). The Trachipterid integument and an hypothesis on its hydrodynamic function. *Copeia, 1963*, 260–270.

Wen, L., Weaver, J. C., & Lauder, G. V. (2014). Biomimetic shark skin: Design, fabrication and hydrodynamic function. *The Journal of Experimental Biology, 217*, 1656–1666.

Wen, L., Weaver, J. C., Thornycroft, P. J. M., & Lauder, G. V. (2015). Hydrodynamic function of biomimetic shark skin: Effect of denticle pattern and spacing. *Bioinspiration & Biomimetics, 10*, 066010.

Whitear, M. (1970). The skin surface of bony fishes. *Journal of Zoology, 4*, 437–454.

Whitehouse, D. J. (1994). *Handbook of surface metrology*. Philadelphia: Institute of Physics Publishing.

Xu, Z., Parra, D., Gomez, D., Salinas, I., Zhang, Y.-A., von Gersdorff Jørgensen, L., Heinecke, R. D., Buchmann, K., LaPatra, S., & Sunyer, J. O. (2013). Teleost skin, an ancient mucosal surface that elicits gut-like immune responses. *Proceedings of the National Academy of Sciences of the United States of America, 110*, 13097–13102.

Yanase, K., & Saarenrinne, P. (2015). Unsteady turbulent boundary layers in swimming rainbow trout. *The Journal of Experimental Biology, 218*, 1373–1385.

Zaccone, G., Kapoor, B. G., Fasulo, S., & Ainis, L. (2001). Structural, histochemical and functional aspects of the epidermis of fishes. *Advnces in Marine Biology, 40*, 253–348.

Zylberberg, L., Bereiter-Hahn, J., & Sire, J. Y. (1988). Cytoskeletal organization and collagen orientation in the fish scales. *Cell and Tissue Research, 253*, 597–607.